Damage and Strain Patterning Simulation of Structural Heterogeneity

Von der Fakultät für Georessourcen und Materialtechnik

der Rheinisch-Westfälischen Technischen Hochschule Aachen

zur Erlangung des akademischen Grades eines

Doktors der Ingenieurwissenschaften

genehmigte Dissertation

vorgelegt von **M.Sc.**

Ding Wang

aus Fuxin, China

Berichter: Professor Dr.-Ing. Dierk Raabe
Univ.-Prof. Dr. rer. nat. Robert Svendsen

Tag der mündlichen Prüfung: 08. Februar 2019

Diese Dissertation ist auf den Internetseiten der Universitätsbibliothek online verfügbar

Acknowledgements

This doctoral thesis was written during my PhD time at the Microstructure Physics and Alloy Design department of the Max-Planck-Institut für Eisenforschung GmbH (MPIE) under the supervision of Prof. Dierk Raabe. I would like to express my appreciation to all the people made this doctoral thesis possible.

First of all, I would like to express my sincere gratitude to Prof. Dierk Raabe for giving me the opportunity to pursue my PhD at his department, and also for his inspiring guidance, careful corrections, continuous support and encouragement during my entire PhD period. Additionally, I would like to thank Dr. Franz Roters, Dr. Martin Diehl and Dr. Pratheek Shanthraj for their support and expertise on constitutive modelling and simulation which have been most important for developing this work. I would also like to thank Dr. Hauke Springer, Dr. Han Zhang, Dr. Christian Baron and Dr. Agnieszka Szczepaniak for their support, discussions and contributions from metallurgy and processing. Furthermore, I would like to thank my examination committee: Prof. Dierk Raabe, Prof. Bob Svendsen and Prof. Jochen Schneider for taking time reading and evaluating my doctoral thesis and examine me.

I would also like to thank all the other colleagues in MPIE for the nice working atmosphere and the interesting scientific discussions. Besides, I would like to gratefully acknowledge the doctoral grant given by the Max-Planck-Institut für Eisenforschung GmbH which gave me financial support during my entire PhD period.

Finally, I would like to express my profound gratitude to my family for their lifelong support and confidence in me: my parents Prof. Xuchun Wang and Yue Zhao. I would also like to express my deepest gratitude to my fiancée Dr. Xiaoyan Yin for your constant caring, support and encouragement.

Contents

1 Introduction

1.1 Overview

Metallic materials can appear macroscopically homogeneous, but most of them exhibit structural heterogeneities at microscopic scale (Werner et al., 2016). Such structural heterogeneities can arise due to complex microstructure and phase arrangements or result from intricate interactions among the deformation and damage mechanisms prior or after loading. Therefore, to study and understand the complex interactions between individual microstructural and micromechanical mechanisms of these structural heterogeneities can not only help getting over technological difficulties of metal forming processes, but also speed up the material design process. Moreover, the mechanical properties of the metallic materials can be optimized by tailoring microstructure according to the effects of microstructural parameters.

Fe – TiB_2 metal matrix composites, also termed high modulus steels (HMS) due to their high specific stiffness, have great potential for lightweight design applications. The structural heterogeneities of HMS exist in its large variations of reinforcement configurations, i.e. particle dispersion, size, morphology and volume fractions, and also defects in the matrix such as grain boundaries. Such heterogeneous structures can create inhomogeneous distributions of the internal stress and strain field across the matrix, thereby exerting a strong influence on particle damage behaviour (Li et al., 2016; Song et al., 1996). The cracking of particles and the associated damage initiation into the adjacent matrix during deformation will result in loss of composite steels toughness and ductility (Dammak et al., 2014; Kulikowski et al., 2000a; Rana, 2014; Weiland et al., 2009). Although great efforts were made in previous studies to investigate the effects

of particle size and shape (Brechet et al., 1991; Caceres and Griffiths, 1996; Jamaati et al., 2011; Kouzeli et al., 2001; Llorca, 1995; Song et al., 1996) and particle spatial distributions (Ayyar et al., 2008; Segurado et al., 2003; Segurado and Llorca, 2006) on the mechanical properties and damage responses of MMCs, the influence of reinforcement configuration is still partially understood due to the multitude of interacting parameters and structural heterogeneities.

The heterogeneous strain patterns in the form of deformation bands (DBs) develop during plastic deformation of f.c.c crystalline materials. The DBs and the associated laminate structure are formed by complex dislocation interactions and lattice re-orientation processes. Such structural heterogeneities can result in strong deformation textures and recrystallization during metal forming processes (Kuhlmann-Wilsdorf, 1999a), which will intensify the anisotropy of materials' mechanical properties and promote damage initiation along structural interfaces. Therefore, DBs and its associated laminate structure have been the subject of research for many years (Barrett and Levenson, 1939; Honeycombe, 1951; Kuhlmann-wilsdorf and Wilsdorf, 1953), and are still of scientific interest today (Dmitrieva et al., 2009; Huang and Winther, 2007; Lee and Duggan, 1993; Wert et al., 2003). However, what is lacking is a systematic investigation of the role of crystallographic orientation, slip system interactions and boundary conditions on the formation of DBs.

In the framework of continuum mechanics, crystal plasticity model can be used to treat the deformation of crystalline materials. Since dislocations have been treated successfully as the primary defect in crystals governing their plastic behaviour (Hutchinson, 1976; Ma and Roters, 2004; Ma et al., 2006; Peirce et al., 1982, 1983; Roters et al., 2010; Schmid and Boas, 1968), micromechanical approaches can be employed to monitor field quantities (stress, strain, slip activities, damage, etc.) and their evolution under varying mechanical loading conditions. Crystal plasticity simulation using an effective spectral method is an important tool used to gain insight into the complex interactions of many microstructural and micromechanical mechanisms in heterogeneous structures (Roters et al., 2018; Roters et al., 2010). This also open pathways to the systematic parameter studies for the material design process

of the novel heterogeneous material with superior properties. Therefore, the main work of this thesis is to conduct systematic studies by crystal plasticity simulations on the impact of individual microstructure features and underlying dislocation interactions on mechanical and/or damage responses of the structural heterogeneities, which can identify the optimized microstructure. The outline of this thesis is presented in the following section.

1.2 Outline

The outlines of this thesis are as following:

Part I Introduction, Objectives, and Fundamentals

- **Chapter 1 Introduction.** The overview and outline of this thesis.
- **Chapter 2 Motivation and objectives.** The individual research objectives of the two subjects investigated in this thesis.
- **Chapter 3 Background.** A brief survey about high modulus steels and heterogeneous strain patterning in f.c.c crystals. The survey is focused on the experimental aspects of Fe – TiB_2 metal matrix composite and dislocation sub-structure in f.c.c crystals.
- **Chapter 4 Simulation theory.** The fundamental theories for crystal plasticity simulations conduced in the present thesis, such as continuum mechanics, constitutive formulations, phase field damage model and spectral method.
- **Chapter 5 Simulation setup.** The model geometries, material parameters and boundary conditions used for simulations in this thesis.

Part II Results and Discussion

- **Chapter 6 Particle-induced damage in Fe – TiB_2 metal matrix composites steels.** The effects of microstructural parameters, such as particle spatial distributions, size and volume fraction, on particle damage initiation and progression are presented.
- **Chapter 7 The formation of laminate deformation patterning in nickel single crystal.** The self-organization of a nickel single crystal into complex laminate bands during plastic deformation and the role of collinear dislocation interaction are presented.
- **Chapter 8 Summary and outlook.** This thesis is summarized, and the possible further work is suggested.

2 Motivation and objectives

The main work of this thesis is to conduct systematic studies by crystal plasticity simulations with respect to the impact of individual microstructure features and their underlying interactions on the deformation and/or damage mechanisms. Two subjects were studied in this thesis: the first is the particle-induced damage in Fe – TiB_2 metal matrix composite steels and the second is the formation of laminate deformation patterning in nickel single crystal. The individual research motivation and objectives are presented in the following:

Particle-induced damage in Fe – TiB_2 metal matrix composite steels

The Fe-TiB_2 metal matrix composites (MMCs) have promising benefits for lightweight design in structural applications, as the addition of stiff lightweight TiB_2 particles increases the specific stiffness (i.e the stiffness/density ratio) of the material. Previous studies showed the Fe-TiB_2 MMCs can be fabricated via liquid metallurgy synthesis (Bonnet et al., 2014; Springer et al., 2015) which can increase production efficiency. Although TiB_2 is very effective in terms of its physical properties, the large stiffness contrast between particle and matrix as well as geometrical constraints result in local stress concentrations, which promotes damage initiation under loading such as cracks within particles, matrix or the associated interfaces. With increasing strain, those cracks or voids can thus result in failure of the composite material. According to previous experimental investigations, good interfacial coherency and high interfacial strength were found (Cha et al., 2012; Huang et al., 2015; Lartigue-Korinek et al., 2015; Li and Huang, 2017) for Fe-TiB_2 MMCs fabricated by eutectic solidification. In addition, the recent studies (Dammak et al., 2014; Dammak et al., 2013; Hadjem-Hamouche et al., 2012; Hadjem-Hamouche et al., 2018; Li et al., 2016) on the

deformation behaviour and damage evolution of Fe-TiB_2 MMCs showed that particle fracture is the dominating damage mechanisms and the main reason for damage failure of the composite at room temperature, whereas particle interface debonding is rarely and much less frequently observed. The reinforcement configurations, such as large variations of particle size, morphology, dispersion, and volume fraction create an associated complexity in the partitioning of the internal stress and strain field across the matrix, thereby exerting a strong influence on particle cracking and the initiation and progression of damage (Li et al., 2016; Song et al., 1996). However, it is difficult to manipulate particle configuration through experiment due to the multitude of interacting parameters and microstructural complexity, i.e. the precise control of particle distribution, size, morphologies, etc. Therefore, to reduce the work and cost associated with experimental microstructure optimization alone, additional systematic screening through simulation studies can be used to speed up this process by providing basic constitutive and morphological guidelines towards identifying favourable particle microstructures (Shanthraj and Zikry, 2012).

To reflect the full microstructure complexity of such compounds, Simulation study was conducted in this thesis with systematically varied clustering degree, particle distribution and volume fraction to derive guidelines for particle microstructures that provide optimum mechanical performance. This integrated computational materials engineering (ICME) approach has the goal to identify key factors for particle damage initiation, growth and percolation, in order to derive synthesis strategies for the next generation of HMS for lightweight applications.

The formation of laminate deformation patterning in nickel single crystal

Crystalline materials, i.e. metals, often develop heterogeneous strain patterns that are characterized by the formation and evolution of banding phenomena during plastic deformation. Such heterogeneities in local strain can be observed as shear bands in polycrystals spanning over several grains after severe deformation or as deformation bands (DBs) in the form of laminates inside individual crystals. In contrast to shear bands, DBs usually occur in a collective manner such that the whole crystal domain is

covered by pronounced sub-grain scale bands of concentrated plastic flow (Dmitrieva et al., 2009; Duggan et al., 1978; Hirsch et al., 1988; Morii et al., 1985). Therefore, DBs have a strong influence on deformation textures, recrystallization and mechanical properties during metal forming processes (Kuhlmann-Wilsdorf, 1999a). Understanding DBs formation can pave the road to a better understating of plastic deformation mechanisms in general. However, DBs did not get enough attention in previous decades due to lack of available theories and good experimental methods for investigation.

To study the evolution mechanism of DBs, simulation study was conducted based on full-field crystal plasticity simulations and hence enables to investigate in detail the role of crystallographic orientation, slip system interactions, and formation processes of the DBs in nickel single crystal. Special attention is paid to the role of collinear interaction between two slip systems, which was reported to be the strongest of all dislocation interactions (Devincre et al., 2006; Kubin et al., 2008; Madec et al., 2003).

3 Background

3.1 High modulus steels

As the background for the first study subject of this thesis, this section will introduce the state of art of high modulus steels and Fe – TiB_2 metal matrix composites materials, and the challenges meet today for the design of future high modulus steels with superior properties. The details of these are presented in the following.

3.1.1 Request from automotive industry

Steels are essential ingredients for modern society. Large varieties of steels have been innovated and developed for a wide spectrum of applications, such as construction, transport, energy sector, etc. One of the major areas where steels are primarily applied is the automotive industry. Since the last decade, weight reduction of automotive structure is of particular interest in the industry where the society urges a reduction of CO_2 emissions. For example, in Europe the regulation requires CO_2 emission in cars must be reduced to 130 g/km by 2015 and to 95 g/km by 2021 in comparison with the statistical average value of 158.7 g/km in 2007[1]. Traditionally, this is achieved by thickness reduction using high and ultra-high strength steel such as dual phase and transformation induced plasticity grades in large scales. The development of high and ultrahigh strength steels is based on good compromise between strength and formability. The higher levels of strength would enable the design of automotive structure with a lower sheet thickness and hence result in weight reduction (Li et al., 2003). The car weight can be reduced even more by using low-density steels such as ferrite-based

1 The data are referred to https://ec.europa.eu/clima/policies/transport/vehicles/cars_en

duplex steel (Rana et al., 2014). However, excessive gauge reduction and/or density reduction can lead to significant reduction of stiffness. For example, for a plate in pure bending, the stiffness is proportional to Ee^3 with E the Young's modulus and e the thickness. Limits are now reached for some applications such as automobile engine and chassis/suspension part. From an engineering point of view, these parts need to have sufficient rigidity to yield only a small strain against applied stress (Pramanik et al., 2014). Therefore, stiffness rather than ultimate strength becomes the critical criterion for materials selection in designing such mechanical parts of automobile (Rana, 2014). A material with an increased specific modulus (Young's modulus per mass density of a material), also known as the specific stiffness (Bonnet et al., 2014), shall be used to achieve design targets, such as high elastic bending stiffness for engine and chassis parts and a low elastic spring-back behaviour during sheet metal forming (Münstermann et al., 2014).

For iron and almost all steels, the Young's modulus is between 190 and 210 GPa which remained for decades on the level of conventional mild steels. In addition, although the elastic modulus of these steels is the highest in structural metallic materials, the specific modulus (about 26GPa cm^3g^{-1}) is approximately the same as other lightweight metals and alloys (such as aluminum, magnesium, titanium alloys). In this case, further development of a high modulus steel, superior in both elastic modulus and material's density is required and necessary, especially for automotive industry. In the following, different ways to achieve high modulus for steels will be introduced briefly.

3.1.2 Methods to increase elastic modulus of steel

Since the elastic modulus of steels depends on its chemical composition, phases and crystal structures, crystallographic textures, several solutions and procedures exist to achieve high modulus:

(1) Alloying elements (atomic scale) can be incorporated to influence the elastic modulus of steels. Since the atomic radii of foreign atoms is different than that of iron and these atoms are either interstitially or substitutionally dissolved in the lattice, the iron lattice will distort, and the interatomic distances will be

modified accordingly. Moreover, the electron distributions in the material will also change due to alloying elements. Therefore, the combined effect of these factors will influence the elastic modulus of steel, either intensify or decrease. Diagrams in Fig. 3.1 from previous work by Speich and Leslie and their co-workers (Leslie, 1972; Speich et al., 1972) show the influence of different alloying elements on the elastic modulus of steel. An increase was found for Co, Re, Cr and a decrease for Ni, Mn, C, Pt and Rh. In recent studies, the elastic constants of steels can not only be projected by the statistical regression analysis (Bohnenkamp and Sandström, 2000), but also can be predicted accurately as a function of composition by ab *initio* calculation (Sandström and Korzhavyi, 2014). However, the increase of elastic modulus by these alloying elements are still limited and the specific modulus does not increase much due to similar density of Co, Re, Cr compared to iron.

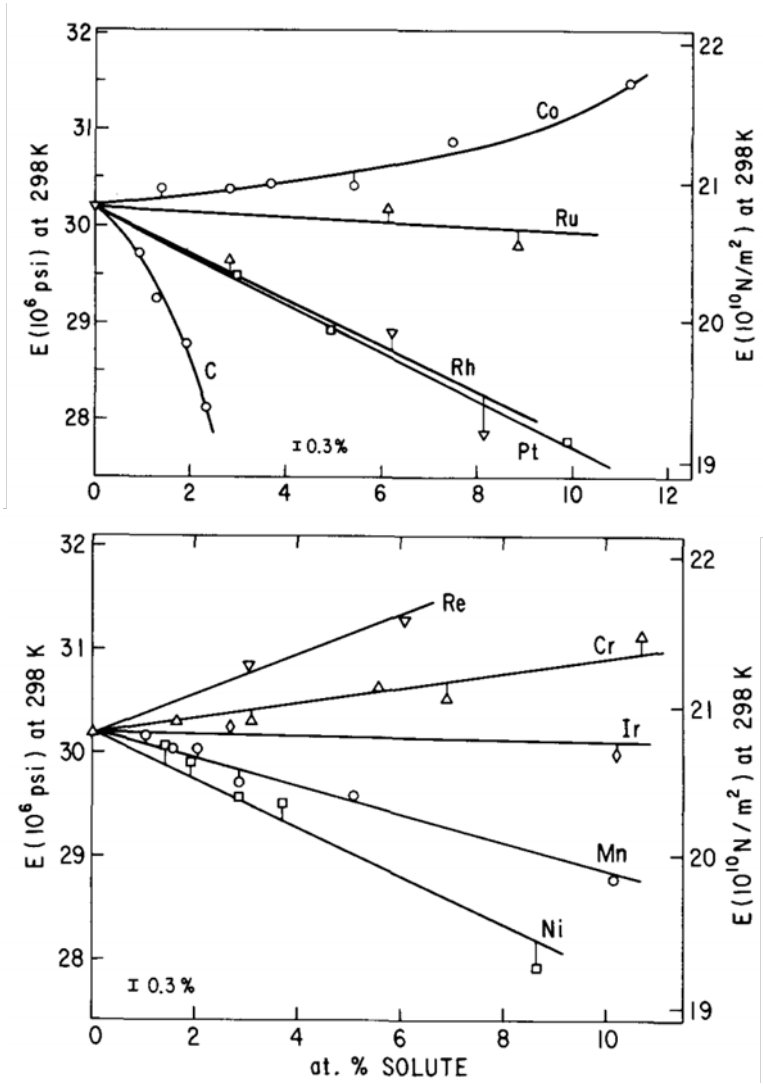

Fig. 3.1. The effect of alloying elements on Young's modulus of steel. (Speich et al., 1972)

(2) A suitable texture design (crystallographic scale) can be used to achieve high Young's modulus in certain direction of materials (Pramanik et al., 2014). The elastic modulus is a texture dependent property. For instance, the Young's modulus of a monocrystal iron is highest along the <111> direction with about 290 GPa and least along the <100> direction with about 135GPa. Therefore, for polycrystal steel, it is possible to apply specific thermomechanical treatment on optimized chemistry to strengthen preferential crystallographic orientations, thus producing an increased value of elastic modulus, for instance, in the thickness of the product. However, this procedure normally will introduce the angular variation of Young's modulus (as shown in Fig. 3.2) which can increase the defects generated during manufacturing operations.

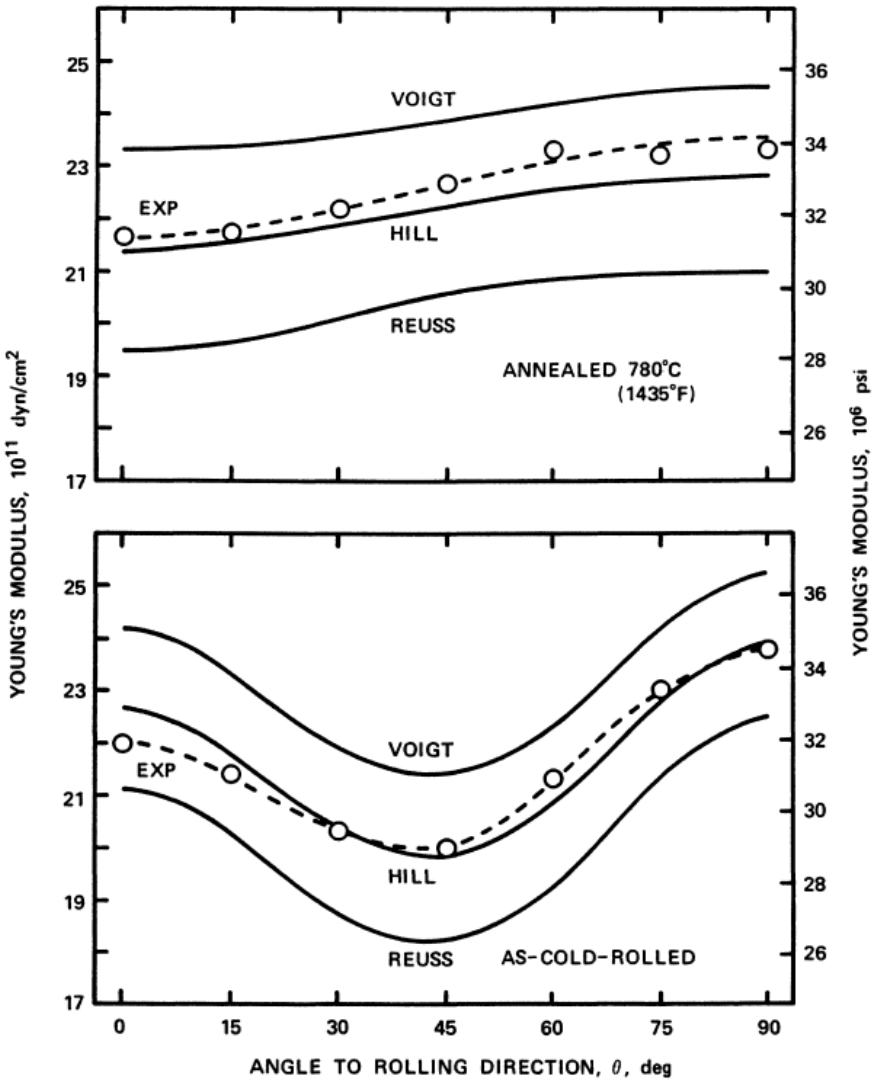

Fig. 3.2. Young's modulus of the annealed and cold-rolled sheets of phosphorous steel along various directions calculated by using Reuss, Hill and Voigt assumptions and determined by experiments. (Hu, 1980)

(3) Stiffness can be increased by composite effect (microstructure scale) with incorporation of high modulus ceramic reinforcement into steel matrix (Rana, 2014). The particles can be oxide or non-oxide ceramics, such as titanium carbide (TiC), vanadium carbide (VC), alumina (Al_2O_3), titanium diboride (TiB_2), chromium carbide (Cr_7C_3), etc. (Akhtar, 2014; Bonnet et al., 2014). The reinforcements are fabricated mostly in particulate or fibre form (Allison and Cole, 1993; Kaczmar et al., 2000; Miracle, 2005). The influence of ceramic particles on both the elastic modulus and the specific modulus of steel are significant, for instance TiB_2 as shown in Fig. 3.3. However, besides the

physical properties of particles, other conditions, such as its stability and compatibility with the steel matrix, fabrication process, as well as the costs should also be considered. One promising advantage of the incorporation of ceramic particles is the improvement in the modulus is isotropic (Tanaka and Saito, 1999). This is of great importance because in most cases the automotive parts are subject to multi-axial stress states, such isotropic properties can be applied well in mixed load conditions of bend, twist and shear. Moreover, the increasing stiffness to weight ratio has enormous benefits for lightweight design which is preferably for structural and dynamically loaded applications.

(4) Stiffness can be also increased by specific macroscopic design, such as fabricating hybrid structures (Lesuer et al., 1996; Sokolova et al., 2012; Xue and Hutchinson, 2007), steel foams (Ashby et al., 2000) and designing optimized shapes (Suzuki and Kikuchi, 1991). These solutions can guarantee the superior improvement of specific stiffness in certain part or directions, but elaborate manufacture process is needed which make it difficult to produce.

Among all the above potential methods to achieve high modulus steels, the third approach of fabricating composite material was verified to be the most feasible and practical, especially for industrial mass production (Bonnet et al., 2014). In the following, the background for Fe – TiB_2 metal matrix composites will be introduced.

3.1.3 Fe – TiB_2 metal matrix composites

The particulate-reinforced metal matrix composites (MMCs) have promising advantages, not only due to its isotropic improvement of high specific stiffness, but also its low cost, high flexibility and availability to achieve excellence performance. Because of this, the initial Al- Al_2O_3 and Al-SiC MMCs were developed and applied predominantly for diesel engines and aerospace fields (Lloyd, 1994). A recent broad review of MMCs ranging from technologies to applications can be found in Miracle (2005). MMCs can be fabricated by several processing routes, either ex situ such as powder metallurgy by blending the reinforcements or precursors powder into a homogeneous matrix (Pagounis and Lindroos, 1998), or in situ such as liquid

metallurgy by reaction between the elemental components or compounds (Tjong and Ma, 2000). It is reported that powder metallurgy synthesis techniques allows for precisely controlling the particle microstructure, but also requires great effort in material synthesis and thus price (F.Ashby, 2005; Nakanishi et al., 2002). This production constraint could be overcome by utilizing liquid metallurgy synthesis (Feng, 2013; Rohatgi et al., 1986), for which Fe — TiB_2 system is ideally suited (Springer et al., 2015). The in-situ syntheses by liquid metallurgy initiated from the equilibrium phase diagrams studies (Shurin and Panarin, 1974; Shurin and Panarin, 1984) on Fe based systems, such as Fe-TiB_2, -ZrB_2, -HfB_2 and -VC. According to these initial studies, the most suitable eutectic alloys appear to be Fe- VC and Fe-TiB_2. However since TiB_2 is very hard, Fe – TiB_2 MMCs is initially applied for wear resistance steels (Sigl and Schwetz, 1991; Telle and Petzow, 1988). Around 2000, Tanaka and Saito (1999) re-calculated the equilibria in Fe-TiB_2 system by Thermo-Calc software and they investigated the potential of increasing the specific modulus of Fe based MMCs by increasing TiB_2 fraction (Tanaka, 2000). From that time, this novel type of steels was termed high modulus steels (HMS). And the trend of HMS development by powder metallurgy (Bacon et al., 2011; Kulikowski et al., 2000b; Wang et al., 2006) and/or liquid metallurgy (Bonnet et al., 2014; Cha et al., 2012; Li et al., 2010; Springer et al., 2015; Springer et al., 2017; Tjong and Ma, 2000) continue to this day.

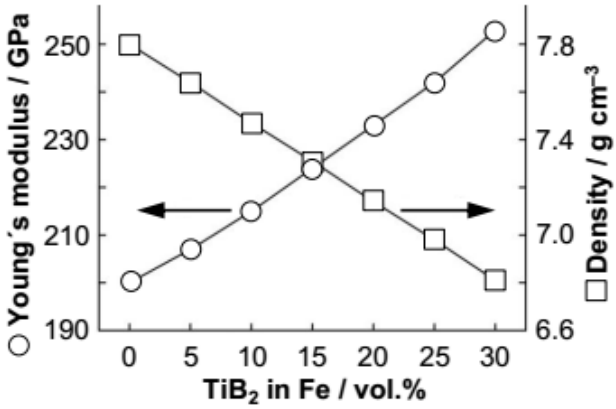

Fig. 3.3. Prediction of Young's modulus and density of Fe for different volume fractions of TiB_2 (rule of mixture), from Zhang et al. (2016).

HMS is a very attractive and ideal candidate of great potential for structural material.

TiB_2 is selected as being the reinforcement particles due to its superior physical properties (Baron, 2017; Feng, 2013), such as its high specific stiffness of 120 GPa cm^3g^{-1} (Munro, 2000), sufficient ductility of 0.94 bulk and shear modulus ratio and high melting point of 3225℃. The specific modulus increases significantly with the TiB_2 fraction up to about 37 GPa $g^{-1}cm^3$ for 30 vol% TiB_2 (Fig. 3.3). The selection and comparison of other reinforcement for HMS can be found in Bonnet et al. (2014). In addition to these, TiB_2 can be formed in-situ directly from Fe-Ti-B melts through liquid metallurgy (Shurin and Panarin, 1974; Shurin and Panarin, 1984; Tanaka and Saito, 1999). The pseudo-binary Fe – TiB_2 is a eutectic system. The phase diagram is shown in Fig. 3.5, of which the eutectic point is situated around 12 vol%. On the left side of the eutectic is termed hypo-eutectic, where small eutectic particles homogeneously precipitate with irregular morphology (Fig. 3.4a). On the right side is termed hyper-eutectic, where large primary particles of angular morphology precipitate directly from the melt and being surrounded by small eutectic particles (Fig. 3.4b). By controlling the cooling rates (Springer et al., 2015; Springer et al., 2017; Zhang et al., 2016) and also alloying additions (Aparicio-Fernández et al., 2016; Li et al., 2010), the distribution, size and morphology of TiB_2 particle in Fe based matrices can be drastically changed. Another important feature for in situ fabrication of Fe – TiB_2 MMCs is the good wettability and thermodynamic stability of TiB_2 with iron/iron-based alloy. This is very critical since it can contribute to the formation of strong interfacial bonding through in-situ precipitation and reduce the possibilities of dissolution by conventional heat treatment. A counter-example is the cementite Fe_3C which can be easily dissolved in bearing steels by a heat treatment (Kang and Rivera-Díaz-del-Castillo, 2013). The interfacial structure and plasticity of TiB_2/ferrite interface were particularly investigated by recent investigations (Cha et al., 2012; Huang et al., 2015; Lartigue-Korinek et al., 2015) which will be introduced in the following subsection.

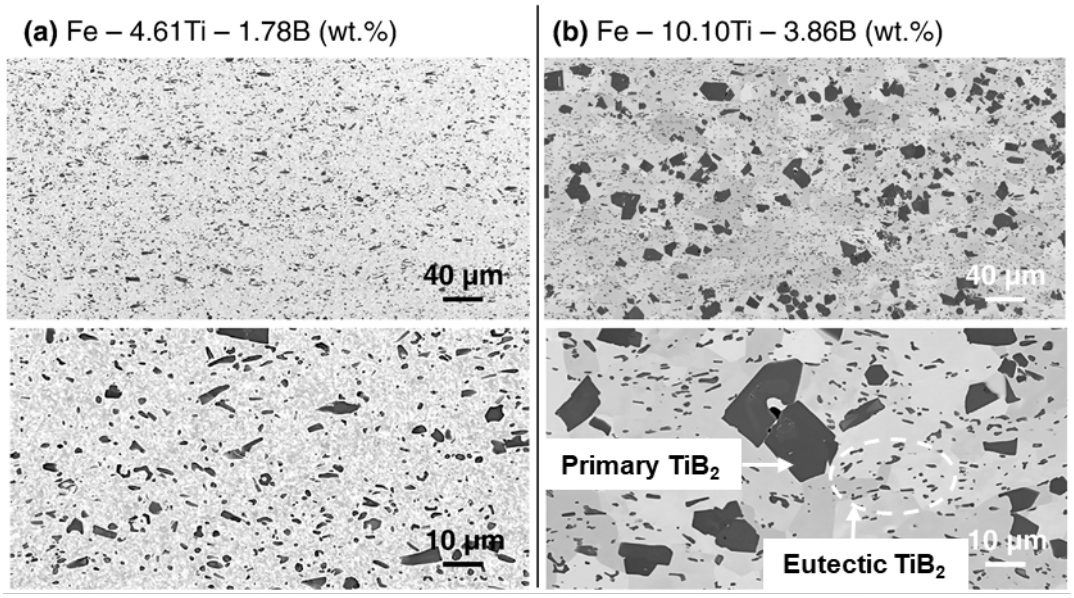

Fig. 3.4. SEM micrographs in backscatter electron contrast of the microstructures of (a) hypo- and (b) hyper-eutectic Fe- TiB_2 alloy. The compositions are present in wt.%. (Baron et al., 2016)

Besides the reinforcement particle and its strong interface, steel matrix also has the advantage of wide spectrum of microstructure and properties tuned by alloying and heat treatment (Rana, 2014). For example, the austenitic matrix obtained by alloying the iron matrix with chromium and nickel not only can achieve high corrosion resistance, but also can increase the volume fraction of titanium diboride in the eutectic (Shurin and Panarin, 1984). The addition of manganese (Mn) can result in broad spectrum of matrix microstructures (α, α, γ and ε-martensite) and phase-mixtures. This has been investigated by Baron et al. (2016). In addition to this, the austenitic matrix can be replaced by harder and stronger martensitic matrix which can increase the mechanical performance of MMCs (Akhtar, 2014). The solid solution strengthening and precipitation influence through ageing treatments were investigated by Szczepaniak et al. (2017).

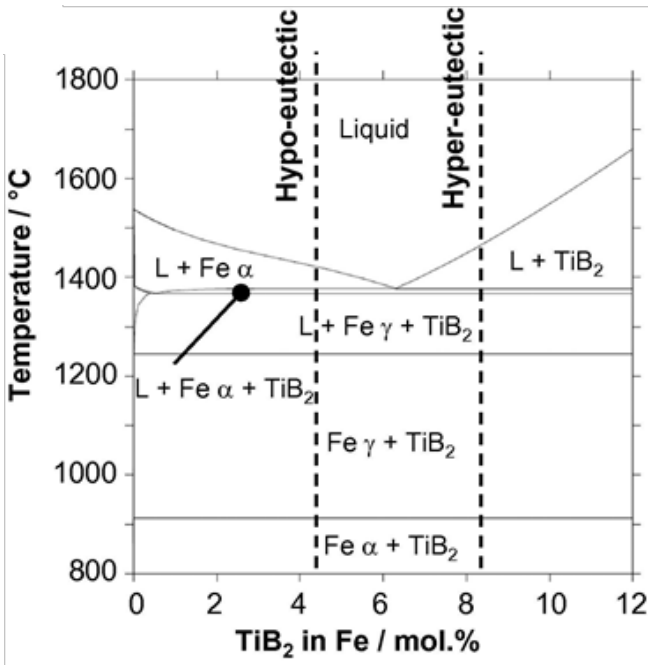

Fig. 3.5. The pseudo-binary phase diagram Fe-TiB_2 system calculated with Thermocalc. (Springer et al., 2015)

3.1.3.1 Reinforcement-matrix interface

The interface between ceramic reinforcement and Fe based matrices plays a key role to achieve significant composite effect on strengthening and good enough ductility for metal forming process. The reinforcing mechanisms related to the interface are classified as direct and indirect mechanisms (Chawla and Shen, 2001). The direct mechanism is the load transfer from the weaker matrix to more stiff reinforcement across the interface (Nardone and Prewo, 1986). In this way, the direct strengthening is based on the load carrying capability of reinforcement and its interface (Akhtar, 2014). The indirect mechanisms are related to two aspects. One aspect is matrix strengthening resulted from the strain induced dislocations due to the thermal mismatch between metallic matrix and ceramic reinforcement (Arsenault and Shi, 1986). Another aspect is the Orowan strengthening due to the addition of large and hard reinforcement in the metallic matrix. The Orowan loops will be resulted as the spacing between the particle reinforcement reduces (Bonollo et al., 1991). The above different mechanisms contribute to the so called ‘composite strengthening’. Therefore, the mechanical properties of MMCs is strongly dependent on the structure and properties of the

interface between reinforcement phase and metal matrix. It is obvious that the defect free and strong interfacial zone is critical for achieving superior mechanical properties and ductility of MMCs (Akhtar, 2014).

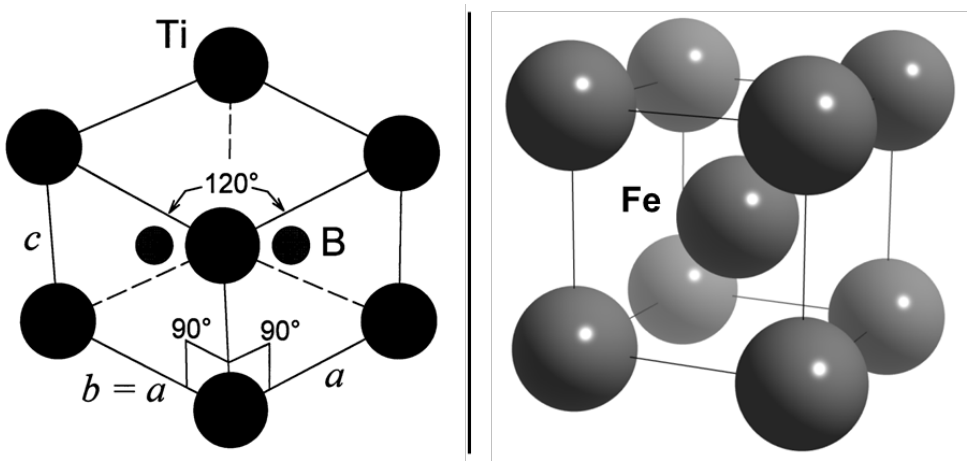

Fig. 3.6. Left: the hexagonal unit cell of single crystal TiB_2 (Munro, 2000). Right: the body-centered cubic unit cell of ferrite (alpha-iron).

The strength of the interface between reinforcement and matrix is influenced by factors, such as wettability (Naidich, 1981), crystallographic coherency (Chawla and Chawla, 2013), thermodynamic stability (Kang and Rivera-Díaz-del-Castillo, 2013), matrix alloying element (Fischmeister et al., 1972) and interfacial reactions (Pagounis and Lindroos, 1998). The wettability represents the compatibility between particle/matrix systems. Naidich demonstrated that the electron of the solid is more tightly bonded, the worse wettability between solid and liquid (Naidich, 1981). As illustrated by Baron (2017), the highly ionic compound Al_2O_3 is difficult to wet, whereas carbides and borides with mostly covalent bonds show good wettability. For example, the bond interactions of TiB_2 include covalent B-B, metallic Ti-Ti and ionic-covalent Ti-B, which can help form compatible interface with iron alloys. Besides the bond character, the alloying elements such as Ni, Si, Al in the iron alloy can increase interfacial activity and wettability (Kübarsepp, 1992). However good wettability still cannot guarantee high strength of the interface. For example, Al_2O_3 particles can be wet well with iron alloy matrix by the segregation of alloying elements Cr, Mo, Mn and Ni (Fischmeister et al., 1972). However, no interfacial reaction took place and Al_2O_3 –

steel interface is weak and easily fractured during straining (Pagounis and Lindroos, 1998). Since the reinforcement and the matrix will rarely be a system in thermodynamic equilibrium by just putting them together, there will be a driving force for some kind of interfacial reaction(s) that will reduce the free energy of the system (Chawla and Chawla, 2013). The interfacial reactions can be some specific chemical reactions, diffusion to form precipitates, alloying element segregation and lattice relaxation through arrays of dislocations. In this way, the interfacial zone will change accordingly such that the interfacial energy is minimized and the work of adhesion is maximized (Howe, 1993).

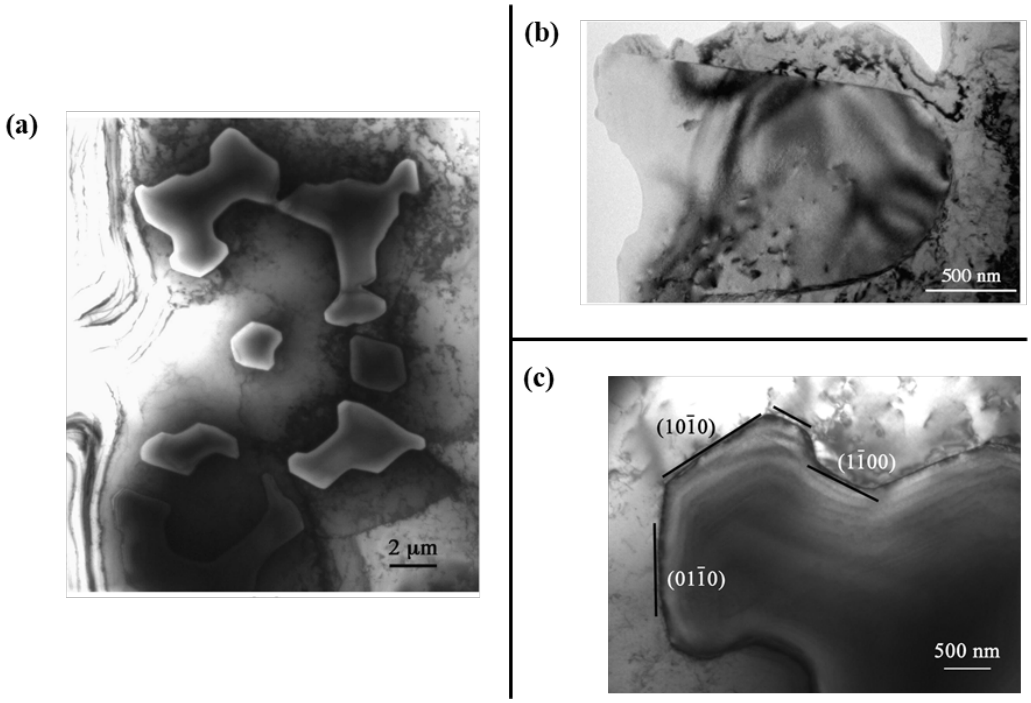

Fig. 3.7. TEM bright-field images: (a) irregular shaped TiB_2 particles (Cha et al., 2012) and (b) rounded interfaces after heat treatment (Lartigue-Korinek et al., 2015) and (c) planes of interface parallel to prismatic $\{\mathbf{10\bar{1}0}\}$ planes (Cha et al., 2012).

The energy associated with the interfacial boundary will decrease in the ascending order of interface crystallographic coherency: incoherent, semi-coherent and coherent. Some precipitates form coherent interface with the metallic matrix with quite small lattice parameter mismatch, such as Al-Al_3Sc system (Novotny and Ardell, 2001). For Fe – TiB_2 MMCs fabricated by eutectic solidification wherein TiB_2 particles are in situ formed exothermically from liquid melt, good interfacial coherency and bonding were found although the lattice unit cells of TiB_2 and ferrite are quite different (Cha et al.,

2012). Good interfacial cohesion has also been observed for the steel composites produced by powder metallurgy (Bacon et al., 2011).

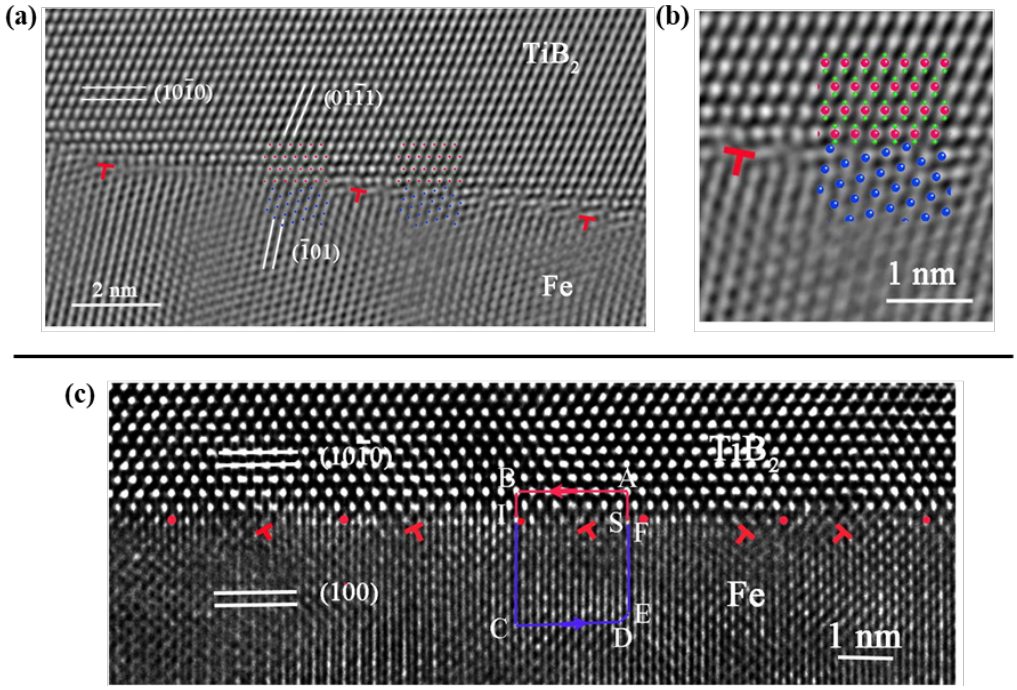

Fig. 3.8. Interfaces parallel to prismatic planes of TiB_2. Top: (a) HRTEM image of a faceted Fe- TiB_2 interface. The projection axis is $[\mathbf{1\bar{2}13}]_{\mathbf{TiB_2}} // [\mathbf{111}]_{\mathbf{Fe}}$. The periodically spaced dislocations are present at interface in the Fe phase and (b) an enlarged image and a model for the interface (Lartigue-Korinek et al., 2015). Bottom: (c) HRTEM image of an interface parallel to $(\mathbf{10\bar{1}0})_{\mathbf{TiB_2}}$ and $(\mathbf{100})_{\mathbf{Fe}}$ (Lartigue-Korinek et al., 2015).

As shown in Fig. 3.6, the crystallographic unit cell of TiB_2 is hexagonal and ferrite is body-centered cubic. To accommodate this lattice structure misfit, some interfacial reactions were revealed to take place. It was found that the interfaces between TiB_2 and the ferritic phase are parallel to prismatic $\{10\bar{1}0\}$ planes (in the majority) and the basal $\{0001\}$ planes of TiB_2. For the interface parallel to the prismatic planes (Fig. 3.7c), the presence of periodically spaced dislocations was found to accommodate the lattice mismatch and orientation deviation (Fig. 3.8a and c). In this way, the lattice continuity of local coherency is preserved. For the interface parallel to the basal plane, TiC platelets were found to be present along the basal plane of TiB_2 (Fig. 3.9a). The formation of TiC is mainly due to two reasons: The first is the concentration of titanium is over the stoichiometric amount required for TiB_2 in order to avoid the formation of Fe_2B (Tanaka and Saito, 1999). The second is the solubility of carbon is smaller in

ferrite than in austenite. During γ→ α phase transformation, free carbon in ferrite can precipitate with excess titanium on the basal plane of TiB_2 owing to the very small lattice misfit between the two phases. As revealed in Fig. 3.9c, the coherency between TiB_2 particle and TiC layer is continued by common titanium atoms. It is noteworthy that TiC possesses good interfacial bonding with iron matrix. According to Pagounis and Lindroos (1998), no interface decohesion was observed in TiC-steel MMCs, only particle cracking during straining. This is because, the TiC particle is Ti-terminated which has a highly metallic character giving rise to bonding strength with iron. The crystallographic orientations between TiB_2 particles and ferritic matrix show no preferential relationships in the as-cast composite. It is reasonable because TiB_2 precipitates either in the liquid phase or simultaneously with austenite precipitation whereas the ferrite phase mostly nucleates and grows at austenitic grain boundaries.

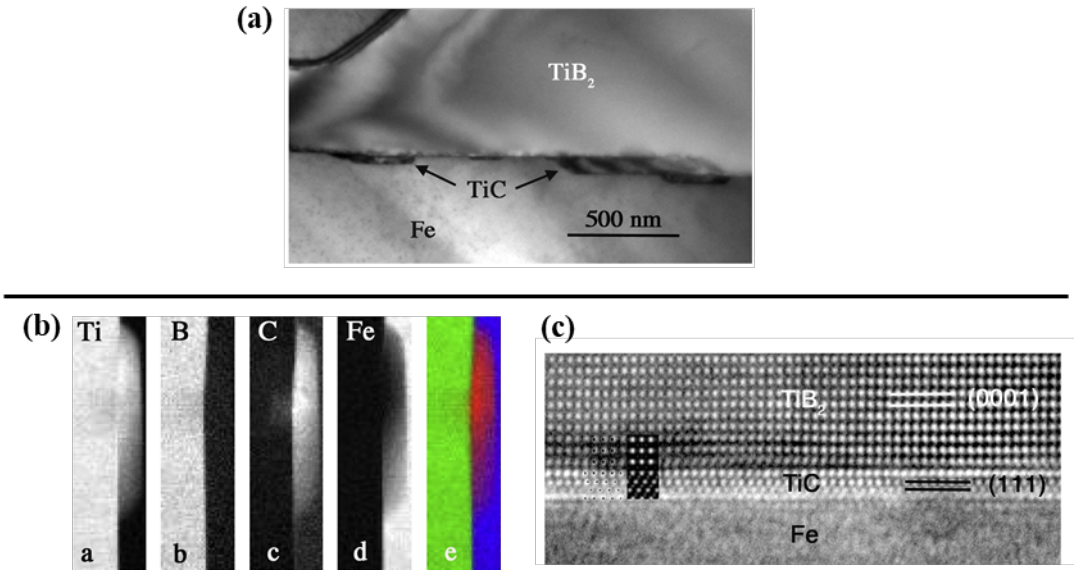

Fig. 3.9. Interfaces parallel to basal planes of TiB_2. (a) Bright field image shows the TiB_2 basal plane covered with TiC (Lartigue-Korinek et al., 2015). (b) Chemical maps showing an interface parallel to a basal plane of TiB_2 with a carbide precipitate (Cha et al., 2012). (c) HRTEM image showing a film of three TiC planes parallel to the basal plane of TiB_2 (Lartigue-Korinek et al., 2015).

3.1.3.2 Co-deformation and damage

Besides the significant change of physical properties (e.g. E/ρ), the addition of hard ceramic particles in metallic matrix can also have large influence on co-deformation

and damage process of MMCs. Direct and indirect strengthening by particles (see section 2.1.4) can result in heavy load on particles and significant accumulation of dislocation density in matrix. The large stiffness (expressed by the Young´s modulus *E*) differences between particle and matrix as well as geometrical constraints imposed by particle morphology (i.e. sharp-edged shape) result in local stress concentrations, promoting damage initiation such as fracture of particles, debonding of interfaces (void nucleation), and void coalescence in matrix (matrix relaxation). The sharp corners created from cracked particles then lead to additional stress concentrations. With increasing strain, dislocations accumulate at opening crack area and large voids can thus form in matrix which result in crack propagation and coalescence. Therefore, final fracture and failure of MMCs material will suddenly take place (Chawla and Shen, 2001; Hadjem-Hamouche et al., 2012).

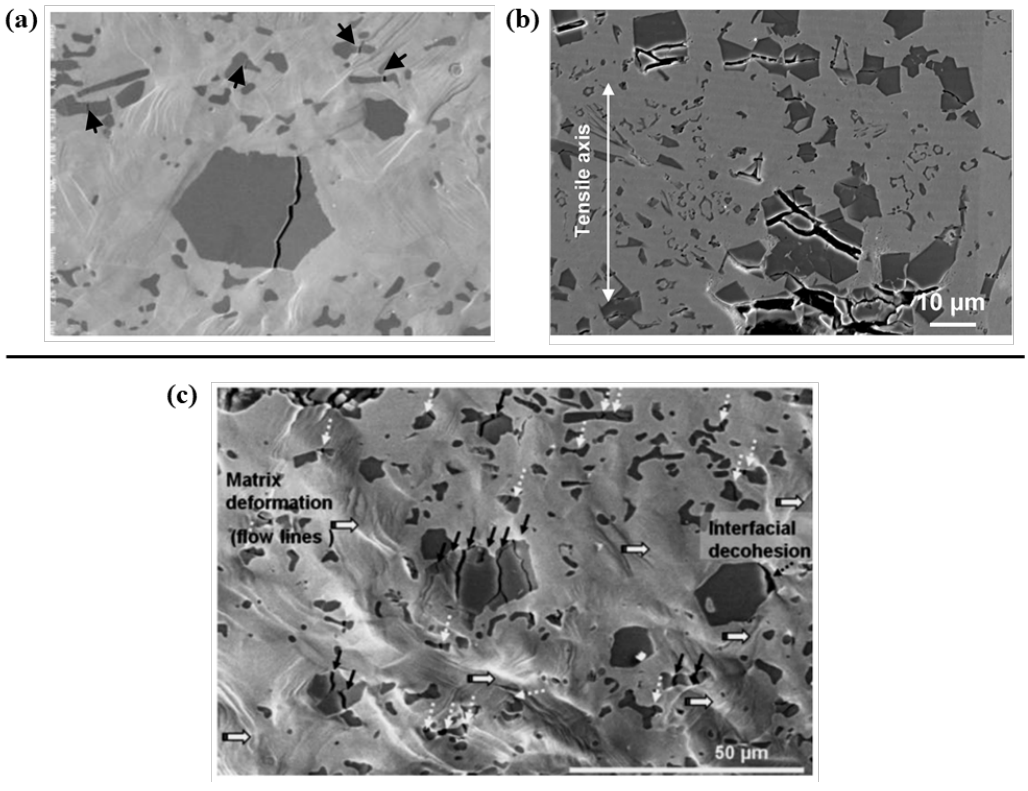

Fig. 3.10. Micrographs of the deformation and fracture behaviour of High Modulus Steel: (a) particle crack of the specimen under four point-bending at ε=8% (Dammak et al., 2013) and (b) SEM image of a section close to the fracture zone of the specimen under tensile loading (Zhang et al., 2016) and (c) the affected zone ahead of the notch in a specimen under three-point bending at 80% of peak load (Hadjem-Hamouche et al., 2012).

Recent studies on deformation behaviour and damage evolution of the Fe-TiB_2 MMCs fabricated by liquid metallurgy were investigated during different strain path testing, such as bending (Dammak et al., 2013; Hadjem-Hamouche et al., 2012), planar simple shearing (Dammak et al., 2014) and tensile testing (Hadjem-Hamouche et al., 2018; Zhang et al., 2016). They all showed that particle fracture (as shown in Fig. 3.10) is the dominating damage mechanisms and the main reason for damage failure of the composite at room temperature, whereas particle interface debonding is rarely and much less frequently observed (as shown in Fig. 3.11a). This demonstrates liquid metallurgy resulting in an excellent interfacial behaviour for load transfer from matrix to particles. The high strength of the particle-matrix interface is supported by previous studies on interfacial structure and chemistry (Cha et al., 2012; Lartigue-Korinek et al., 2015). In addition, a nanoindentation study conducted by Huang and co-workers (Huang et al., 2015) reported some degree of interfacial plasticity, proven by the presence of a high dislocation density at the TiB_2-matrix interfaces, which also support good interfacial compliance and bonding.

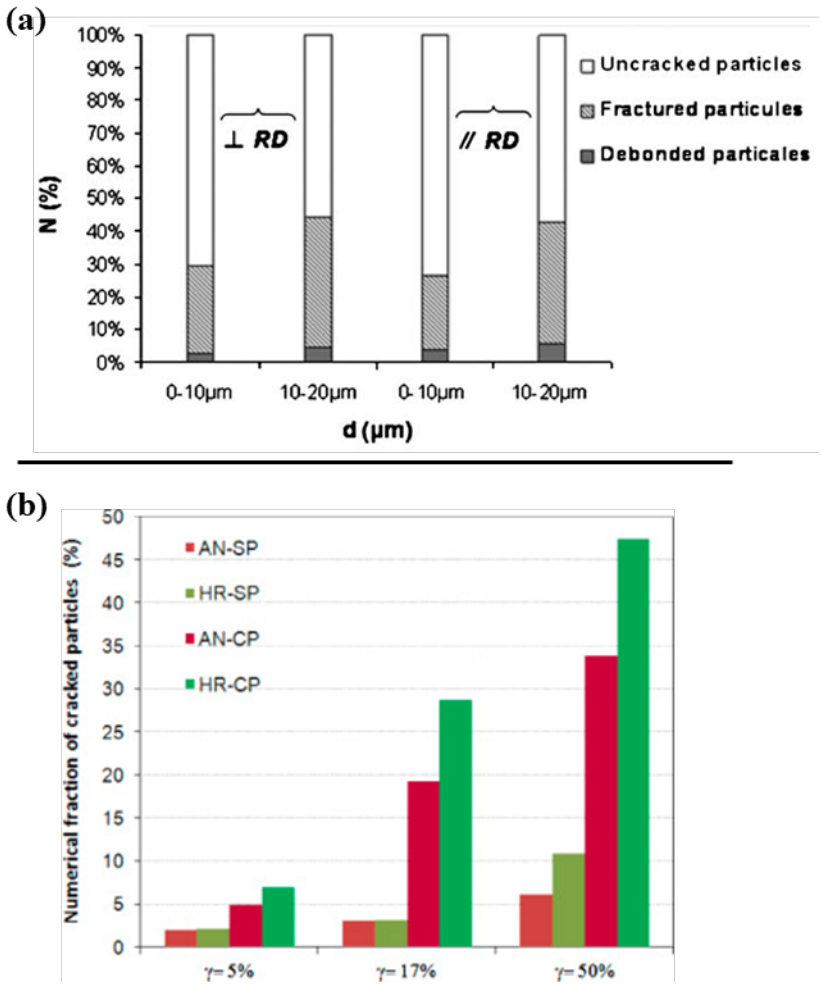

Fig. 3.11. (a) Number fractions of fractured and debonded particles in a specimen under three-point bending at peak of load. (Hadjem-Hamouche et al., 2012). (b) Evolution of the numerical fractions of small (SP) and coarse (CP) fractured particles of annealed (AN) and hot-rolling (HR) composites during planar simple shear (Dammak et al., 2014).

It was found that the large primary TiB_2 particles are fractured more frequently than the small eutectic particles, especially for simple shear testing (Fig. 3.11b). Primary TiB_2 particles are not always single crystals, some of them appear as polycrystalline or in form of crystal aggregates. However, cracks in polycrystalline TiB_2 do not necessarily follow grain boundaries (Dammak et al., 2014). In addition, multi-cracking was observed in large primary particles, especially at high plastic strain (Fig. 3.10b and c). Owing to the stress concentration induced by the crack tips, intragranular shear bands are resulted at an angle roughly equal to 45° to the crack plane, and retard crack propagation and coalescence between fractured particles (Hadjem-Hamouche et al., 2018). In this way, the whole matrix become fragmented. Low angle sub-boundaries

will develop to accommodate the plastic strain and the stress at the matrix-particle interface (Lu and Sass, 1995). However, with increasing plastic strain, the accumulation of dislocations at or near the interface will then promote void nucleation in the matrix and result in crack coalescence and final fracture of the material.

3.1.3.3 Challenges for Fe-TiB_2 MMCs design

Although many aspects about Fe-TiB_2 MMCs, such as fabrication process, alloying element influence, interfacial structure and properties, deformation and damage behaviour, have been thoroughly and clearly investigated and understood, the design of this novel HMS material still face great challenges. As already mentioned above, the main concern on the performance of HMS is their tendency to have relatively low ductility and fracture toughness. Irrespective of the good interfacial properties, the cracking of particles and the associated damage initiation into the adjacent matrix during deformation still results in loss of composite toughness and ductility (Dammak et al., 2014; Kulikowski et al., 2000a; Rana, 2014; Weiland et al., 2009). This issue poses a major concern on the application of such composites as structural materials in automotive industry. The main challenge is the complex microstructure of the reinforcements and its interactions with iron-based matrix. These complexities can be large variations of particle size, morphology, dispersion, and volume fraction. They create an associated complexity in the landscape of the internal stress and strain field across the matrix. thereby exerting a strong influence on particle damage behaviour and the progress of damage initiation (Li et al., 2016; Song et al., 1996). In addition, wide spectrum of matrix microstructure ranging from different phases, grain size, grain boundaries, etc., can also have influence on particle damage and the associated matrix fracture. It is possible to manipulate particle configuration, for example, by controlled solidification such as the decrease in particle size by fast solidification or rendering a regular distribution by eutectic remelting (Springer et al., 2015). The particle morphology can also be controlled by different alloying elements and heat treatments (Aparicio-Fernández et al., 2016). However, the great efforts and large cost associated with the systematic experimental study render them often impractical, since particle

size, morphology and dispersion for example cannot be independently varied. Therefore, simulation approach can be used to overcome these difficulties. The corresponding modelling studies can speed this process up and provide basic constitutive and morphological insights into suited microstructures. However, the mechanical modelling of fracture process in a ductile metallic matrix with hard second phase is difficult which requires good compatibility and combination of local damage events between brittle particles and ductile matrix.

So far, the parametric studies regarding deformation and damage mechanisms in MMCs by modelling were mostly carried out in aluminium-matrix composites reinforced with alumina or silicon carbide. For instance, Segurado et al. (Segurado et al., 2003; Segurado and Llorca, 2006), studied the effect of the particle spatial distribution on the mechanical behaviour in model aluminium-alumina MMCs with up to 15 vol.% of reinforcement. They found that the probability of particle fracture increases 3-6 times even for small degrees of particle clustering. Similar findings were also reported by Ayyar et al. (Ayyar et al., 2008) in a simulation study on aluminium-carbide MMCs. Experimental studies on particle fracture in Al matrix composites (Brechet et al., 1991; Caceres and Griffiths, 1996; Jamaati et al., 2011; Kouzeli et al., 2001; Llorca, 1995; Song et al., 1996) reported that composites containing larger particles are more likely to experience particle fracture during deformation. However, these studies focused only on small sets of samples and without systematic variation of particle distribution and particle size (Davis et al., 1998; Hall et al., 1994; Hauert et al., 2009). Therefore, systematic simulation study with varied particle configurations is needed to provide guidelines for optimum microstructure. In this way, synthesis strategies can be derived for the next generation of HMS with superior physical and mechanical properties.

3.2 Heterogeneous strain patterning

As the background for the second study subject of this thesis, this section will introduce the heterogeneous subdivision of the microstructure, i.e. cell blocks structure, deformation bands and shear bands in f.c.c crystals. Since the dislocation activities play a dominant role on the development of such heterogeneous strain patterning, the underlying mechanism of the associated dislocation interactions will also be introduced in this section.

3.2.1 Cell blocks structure

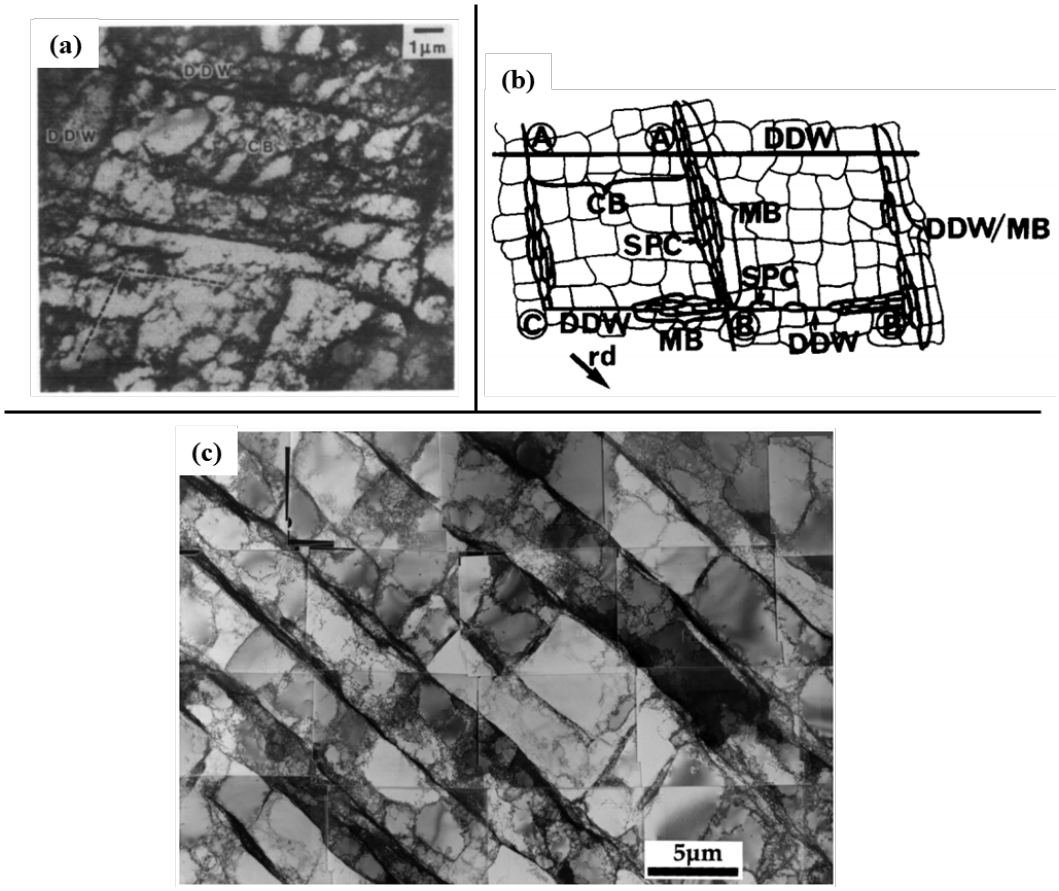

Fig. 3.12. (a) Microstructure parallel to the longitudinal plane in pure nickel rolled to 20% reduction. The continuous dense dislocation wall (DDW) delineating cell block (CB) consisting of ordinary dislocation cells (Bay et al., 1992). (b) Idealized microstructure parallel to a longitudinal section of an f.c.c such as aluminium after rolling. The microstructure includes DDWs and microbands (MBs) which always occur in the combination of DDW-MBs. DDW-MBs are boundaries delineating CBs composed of ordinary dislocation cells. MBs are composed of strings of "small pancake shaped cells" (SPCs) with 1 to 4 layers width. Arrow rd marks the rolling direction (Bay et al., 1989). (c) Microstructure parallel to the transverse section in aluminium rolled to 10% reduction. The ordinary dislocation cells are delineated

by parallel DDWs (Leffers, 2001).

Crystalline ductile materials, i.e. metals, often develop heterogeneous deformation patterns during plastic deformation. As shown in Fig. 3.12a and c, individual grains of polycrystalline materials with a medium or high stacking fault energy (SFE), such as aluminum or nickel alloys, always subdivide into dislocation cell blocks (CBs) which deform by fewer slip systems (less than five) than that specified by the Taylor criterion for strain compatibility (Bay et al., 1989). The idealized cell structure is given in Fig. 3.12b. After a small amount of plastic deformation, the microstructure develops to a structure consisting of dislocation cells from initial "tangled" dislocations due to dislocation interactions (Hirth and Lothe, 1982). As the deformation increases, groups of small ordinary equiaxed dislocation cells are divided further into big CBs which are delineated by the boundaries of dense dislocation walls (DDWs). The dislocation density is low for inner cell interiors but high for cell walls. At some sections, the DDWs tend to split into microbands (MBs) with width of double or multiple layers. The morphology of MBs can be strings of "small pancake shaped cells" (SPCs). Therefore, the boundaries in the combination of DDW-MBs delineate CBs composed of ordinary dislocation cells. The size of cell blocks will decrease with increasing strain (Gracio et al., 1989). In this way, the materials develop into such CBs structures are called "cell forming" metals. As described in Taylor model (Bishop and Hill, 1951; Taylor, 1938), dislocation slip is homogeneous within individual grain of a polycrystal and at least five slip systems are required for an arbitrary deformation. Therefore, crystals which do not form distinct cell blocks but are composed of sets of parallel dislocations with quasi-uniform dislocation density are called Taylor lattices (Kuhlmann-Wilsdorf, 1989), such as f.c.c metals with low SFE. For cell forming metals, the number of operating slip systems in any CBs is usually less than that required for an arbitrary deformation, but groups of neighboring CBs can fulfill the Taylor criterion collectively (Bay et al., 1992). The dislocations in CBs and DDWs are trapped via the formation of low-energy dislocation structures (LEDS) which is a principle described by Kuhlmann-Wilsdorf (Kuhlmann-Wilsdorf, 1989, 1999b). The LEDS theory is

actually an union of the models by Taylor (1938) and model by Bishop and Hill (1951), by requiring minimization of the free energy of the system composed of deforming material and applied traction.

3.2.2 Deformation bands

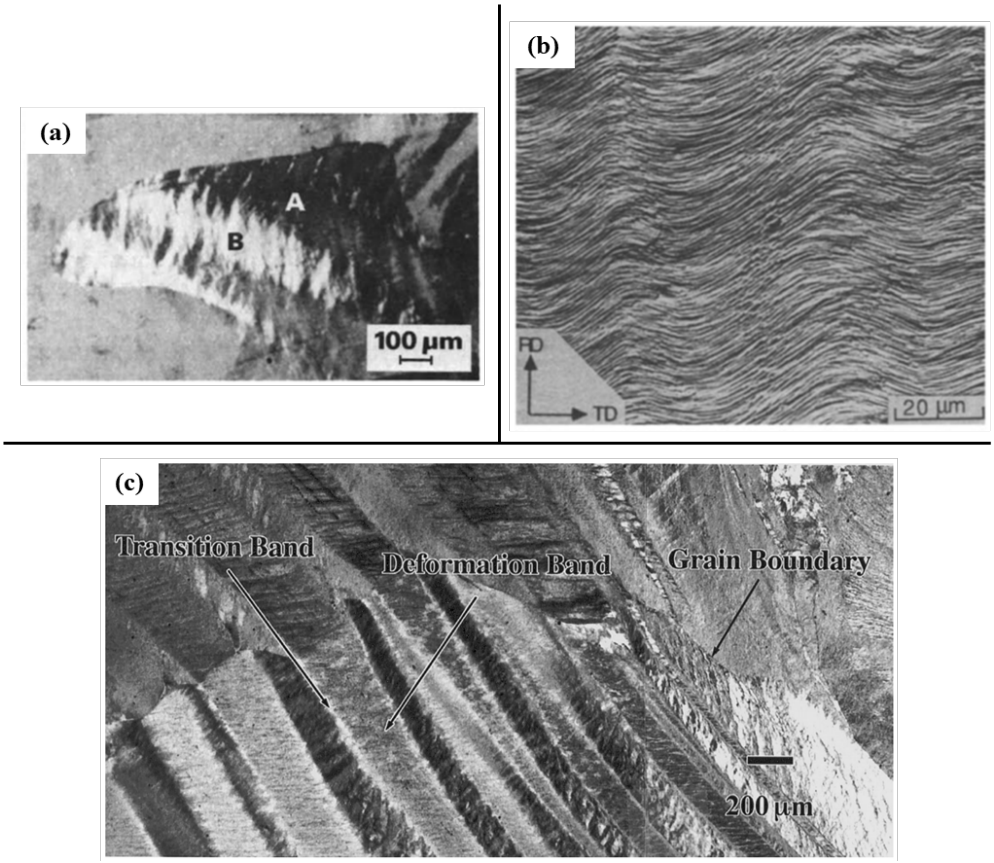

Fig. 3.13. (a) Deformation bands on (001) surface in a [120] grain of aluminium deformed in tension to a strain of 0.05. The rotation angle between area A and B is 2.8° (Bilde-Sørensen, 1986). (b) Rolling plane section of coarse-grained copper cold-rolled to 70%. The grain exhibits an undulating lattice pattern which splits into alternating bands of complementary orientations $(\mathbf{110})[\mathbf{1\bar{1}2}]$ and $(\mathbf{110})[\mathbf{112}]$ (Lee and Duggan, 1993) (c) Optical micrograph of the etched mid-plane of Al-Cu after uniaxial compression to 69% true strain showing distinct deformation bands (Kulkarni et al., 1998).

Besides the mosaic CBs patterns, banding patterns are also very common and typical in plastic deformation for crystalline material. For pure f.c.c metals, deformation bands (DBs) tend to develop during early stage of deformation as a kind of slab-like parallel sequences of dislocation cells with alternating lattice orientation (Kuhlmann-Wilsdorf, 1999a). The optical micrographs of DBs in aluminum and copper alloys are shown in Fig. 3.13a-c. DBs were first systematically studied in aluminum by Barrett and Levenson (1940). Barrett found that the plastic deformation within individual DBs is

caused by simultaneous activation of fewer slip system than that required for homogeneous deformation, which is incompatible with the models of Taylor (1938), Bishop and Hill (1951) and Sachs (1928). In contrast to shear bands, which occur as a localized phenomenon in an otherwise unaffected surrounding, DBs usually occur in a collective manner such that the whole crystal domain is covered by pronounced sub-grain scale bands of concentrated plastic flow (Dmitrieva et al., 2009; Duggan et al., 1978; Hirsch et al., 1988; Morii et al., 1985). Therefore, DBs have a strong influence on deformation textures, recrystallization and mechanical properties during metal forming processes (Kuhlmann-Wilsdorf, 1999a). Thus, understanding DB formation can pave the road not only to a better understating of plastic deformation mechanisms in general, but also can achieve technological and engineering improvement on metal forming process. DBs and the associated laminate structure have been the subject of research for many years (Barrett and Levenson, 1939; Honeycombe, 1951; Kuhlmann-wilsdorf and Wilsdorf, 1953) and are still of scientific interest today (Dmitrieva et al., 2009; Huang and Winther, 2007; Lee and Duggan, 1993; Wert et al., 2003). The existence of DBs generally correlates with the evolution of underlying dislocation structures as the dislocations are the elementary carriers of plasticity (Taylor, 1934). However, DBs did not get enough attention in previous decades due to lack of available theories and good experimental methods for investigation. In recent years, the formation of DBs in metal crystals was explained in terms of the LEDS theory (Kuhlmann-Wilsdorf, 1989, 1999a) and the minimization of the plastic work (Chin and Wonsiewicz, 1969; Lee and Duggan, 1993; Lee et al., 1993) when specific slip systems are active in certain bands. Based on the finding that the occurrence of DBs is energetically preferable over homogeneous plastic deformation, several approaches to model DBs were developed by, e.g., Chin and Wonsiewicz (1969), Lee et al. (1993), Ortiz and Repetto (1999), and others (Kochmann and Hackl, 2011; Miehe et al., 2004; Petryk and Kursa, 2013). They all showed that deformation band patterns can occur as the energetically preferable response of an initially homogeneous material. However, few of the studies placed attention on the role of crystallographic orientation, slip system interactions, and formation processes of the DBs. Therefore, the evolution

mechanisms of DBs can be studied more deeply and thoroughly by robust crystal plasticity simulation which can exceed the experimental limitations at microscopic scale (Wang et al., 2018a).

3.2.3 Shear bands

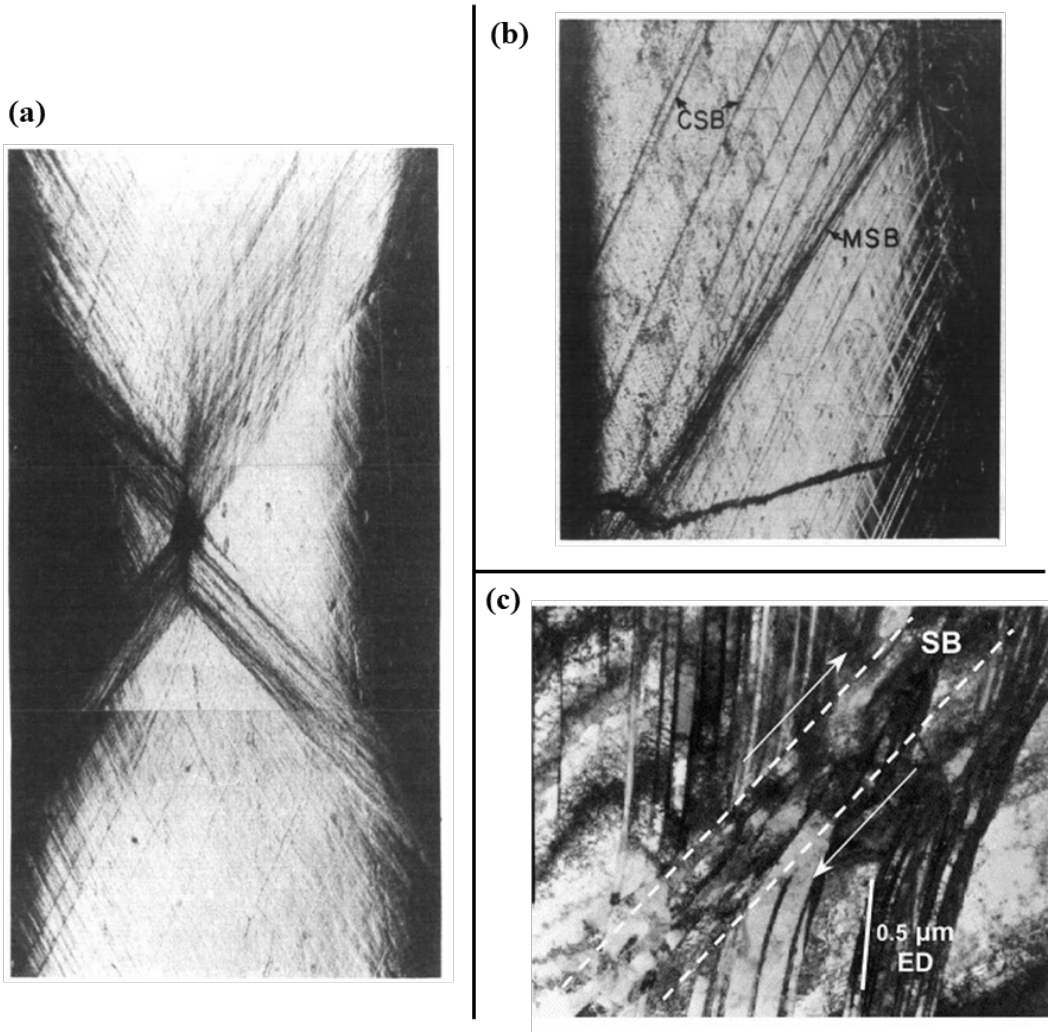

Fig. 3.14. (a) Localized shear bands in a single crystal of Al-2.8 wt% (Chang and Asaro, 1981). (b) The macroscopic shear bands (MSB) misoriented with the coarse slip bands (CSB). CSB are aligned with the operating slip systems (Chang and Asaro, 1981).(c) Early stage of shear band formation being surrounded by thin twin-matrix lamellae (Paul et al., 2002).

At large plastic strain, the most obvious heterogeneous deformation phenomena are localized shearing patterns which develop through the instabilities modes of diffuse necking and shear bands (SBs) (Saimoto et al., 1965). Such localized phenomena get considerable technological attentions since it can cause severe geometric softening and rupture to the metal. The growth of the diffuse necking mode is observed to precede the

onset of localized shear band (Saimoto et al., 1965), as shown in Fig. 3.14a. The diffuse necking causes inhomogeneous lattice rotations which induce geometrical softening: this in turn promotes the formation of shear bands (Peirce et al., 1982). The geometrical softening is the lattice re-orientation with respect to the loading axis so as to increase the shear stress of the operating systems. The resulting effect of the geometrical softening is the reduced flow stress of the crystal (Fig. 3.15). The shear bands can form while the metals are strain hardened. Shear bands can across single crystal or span over several grains and also twin-matrix lamella (Fig. 3.14c) in polycrystals (Paul et al., 2009). According to Chang and Asaro (1981), the onset of shear bands is associated with a critically low value of the ratio of slip plane hardening rate to current flow stress. The instabilities mechanisms which control the bifurcation from the homogeneous deformation into diffuse necking and the subsequent shear bands were given in Peirce et al. (1982) and Asaro (1983). After the occurrence of instabilities, the lattice within shear bands will undergo large misorientations with the surroundings which lead to further geometrical softening. Therefore, the planes of bands are misoriented with respect to the operating slip planes, so shear bands are seen generally non-crystallographic (Fig. 3.14a and b). In this way, tilt boundaries are formed between shear band and matrix, and the intense localized deformation within shear band can cause rapid failure by shear fracture. More fundamental discoveries about SBs can be found in the work of Harren et al. (1988).

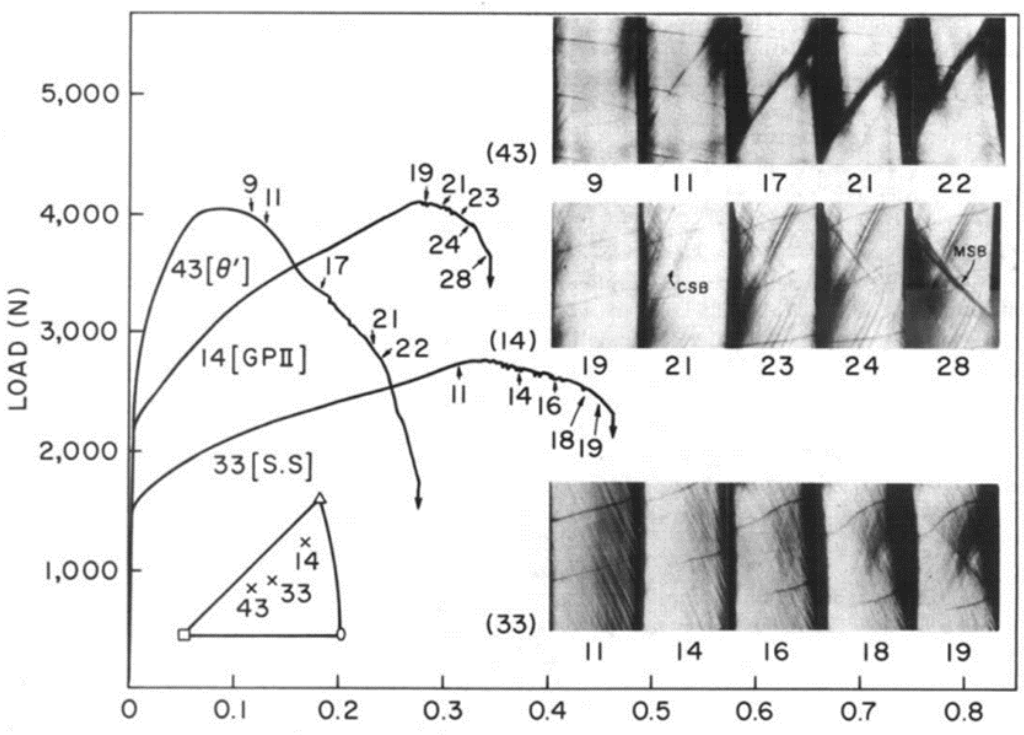

Fig. 3.15. Flow curves plot for samples with various ageing treatment. The evolution of inhomogeneous deformation pattern from coarse slip band (CSB) to macroscopic shear band (MSB) was shown with the number corresponding to the indicated points on the flow curves (Chang and Asaro, 1981).

3.2.4 Crystallographic orientation dependence

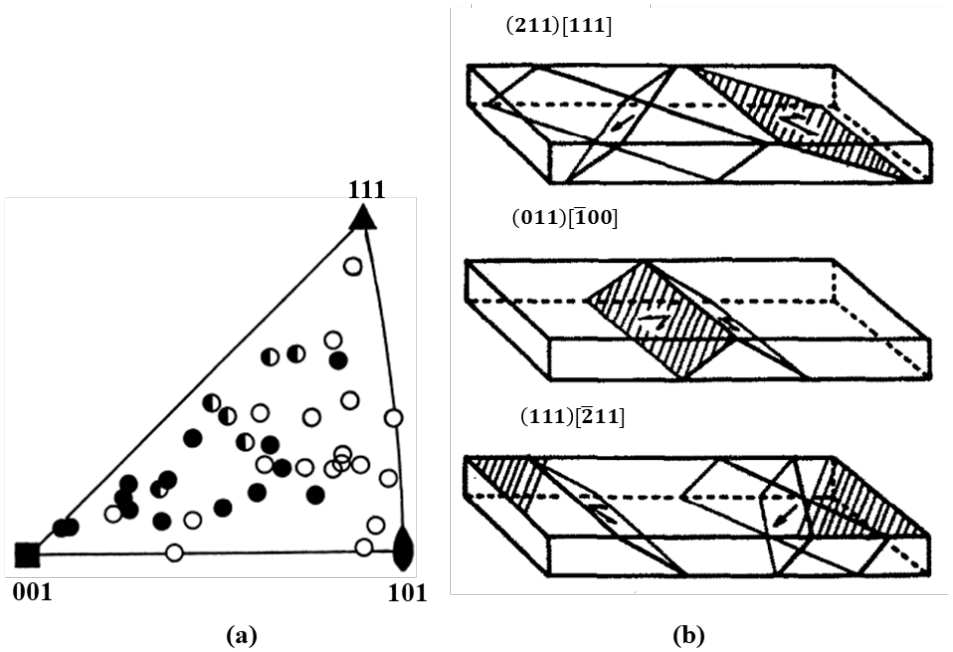

Fig. 3.16. (a) Unit triangle showing the orientation dependence of the tendency towards deformation band formation in compressed aluminum samples according to Barrett and Levenson (1940). ○No bands; ● deformation band. (b) Schematic plot of geometric configuration of active slip system and of the mechanical twin lamellae in the various symmetric crystal orientation. Arrow indicate respective slip

directions. Hatched planes represent lamellae of mechanical twins. (Morii et al., 1985).

It was found that the formation of banding pattern has a strong dependence on crystallographic orientation through single crystal experiments and crystal plasticity simulations (Jia et al., 2012a; Morii et al., 1985; Nakayama and Morii, 1987). Systematic studies of the effect of crystallographic texture on the formation of shear bands in face-centered-cubic single crystals have been done (Jia et al., 2012a; Kuroda and Tvergaard, 2007). It was shown that under near-plane strain rolling conditions, the so-called Copper orientation $\{112\}_{\mathrm{ND}} < 111 >_{\mathrm{RD}}$ shows a pronounced tendency to develop localized bands. This behaviour was also observed in experiment (Dmitrieva et al., 2009). In addition, Brass$\{110\}_{\mathrm{ND}} < 1\bar{1}2 >_{\mathrm{RD}}$ and Brass-R $\{111\}_{\mathrm{ND}} < 11\bar{2} >_{\mathrm{RD}}$ orientation also show tendency to form SBs, whereas such bands do not form in rolled single crystals of cube $\{001\}_{\mathrm{ND}} < 100 >_{\mathrm{RD}}$ and Goss $\{011\}_{\mathrm{ND}} < 100 >_{\mathrm{RD}}$ orientation, respectively. The orientation dependence of the tendency towards DBs formation in compressed aluminum was given by Barrett and Levenson (1940), as shown in Fig. 3.16a. It is worth noting that under symmetric crystallographic orientation, such as [100] and [111], multiple slip with same Schmid factors will simultaneously activate after plastic deformation. The geometric configurations of the slip system activated under such symmetric orientations are shown in Fig. 3.16b. However, due to small inhomogeneity or perturbation in the crystal lattice, the crystal subdivides into distinct regions each of which is dominated by single slip (Piercy et al., 1955). Such slip partition or subdivision process in single crystal is largely influenced by dislocation interactions, i.e. the latent hardening effect on the selection of slip system during deformation process.

3.2.5 Dislocation interactions

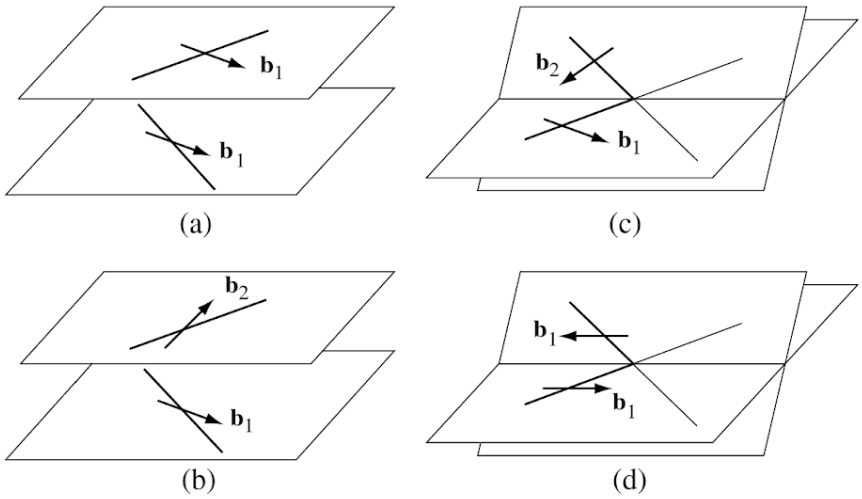

Fig. 3.17. The elementary short-range interactions between perfect dislocations in the f.c.c structure. (a) self-interaction. (b) coplanar interaction. (c) glissile, Lomer or Hirth junctions. (d) collinear interaction (Kubin, 2013).

For crystalline materials, latent hardening between the different slip systems, arising from the interaction of dislocations, strongly influences the strain hardening behaviour and the development of heterogeneous deformation patterns under prescribed deformation. Dislocations, as elementary linear defects, can not only carry plastic flow in crystals, but also can react with each other to form reaction products which might act as barriers to further dislocation motion. To unzip a junction and remobilize the dislocation, a critical resolved stress value must be raised so that dislocation crossing occurs. The Taylor relation (Taylor, 1934) states that the resolved flow stress τ, is proportional to the average distance between the intersecting obstacles in the slip plane and is therefore proportional to the square root of the dislocation density ρ. The dislocation density is assimilated to either the total density (Kocks and Mecking, 2003) or the total density of forest obstacles, so that the relation is also called “forest model”. The relationship is as follows:

$$\tau = \alpha \mu b \sqrt{\rho} \tag{3.2-1}$$

where μ is the shear modulus, b is the magnitude of the Burgers vector of the mobile dislocations and α is an average resistance value of the junction strength over all existing dislocation reactions. The magnitude of α has been estimated both theoretically

(Saada, 1960; Schoeck and Frydman, 1972) and experimentally (Basinski and Basinski, 1979; Neuhaus and Schwink, 1992) and it was suggested that $\alpha = 0.35 \pm 0.15$ in f.c.c metals (Gil Sevillano, 1993).

However, due to the wide spectrum of possible dislocation reactions, the average strength value α is not applicable when considering dislocation densities on different slip systems individually. Therefore, an extension of the classical Taylor's relation was developed to account for the anisotropy of interactions between slip systems, where the dislocation density is decomposed into densities ρ^j per slip system (j). Eq. (3.2-1) is expanded in the form after Franciosi et al. (1980):

$$\tau_c^i = \mu b \sqrt{\sum_j a^{ij} \rho^j} \tag{3.2-2}$$

where τ_c^i is the critical resolved shear stress for the activation of slip system (i), which depends on dislocation densities in all slip systems. a^{ij} is a matrix of coefficients expressing the average strength of the interactions and reactions between slip systems (i) and (j). In f.c.c crystals, the interaction matrix a^{ij} has $12 \times 12 = 144$ coefficients. However, due to the diagonal symmetry of the matrix and the four <111> axes with ternary symmetry, the number of independent coefficients is reduced to six. Hence, only six distinct types of interactions are associated with the self and latent hardening. The interactions are schematically illustrated in Fig. 3.17. Two of them involve non-contact elastic interactions between dislocations gliding in parallel slip planes, namely self and coplanar interaction, Fig. 3.17a and b. Direct annihilation or the formation of dipoles or multipoles may result from self- and coplanar interactions. However, the probability of occurrence of such configuration is quite low. Three of them account for the formation of junctions or locks through forest interactions between non-coplanar slip systems (Fig. 3.17c), i.e. the Lomer-Cottrell lock, the Hirth lock and the glissile junction. The Hirth lock results from the interaction of non-copnanar dislocations with orthogonal Burgers which is slightly weaker. The glissile junction with the resulting Burgers vector along the intersection line which can glide in one of the two slip planes. The Lomer-Cottrell lock occurs between dislocations with dissociated partial parts

which result in sessile junction of edge character. This junction is a strong barrier to dislocation glide in f.c.c crystals. The last interaction, collinear interaction occurs between dislocations of parallel Burgers vectors gliding in two cross-slip planes (Fig. 3.17d), lead to dislocation annihilations. In recent years, the collinear interaction was found to be the strongest among all interactions (Devincre et al., 2005; Madec et al., 2003). In f.c.c crystals, the very strong collinear interaction can play a crucial role on the heterogeneous subdivision of systems in disconnected zones of the crystal, which was investigated in the present thesis.

4 Simulation theory

This section will present the fundamental knowledge of simulation theories related to this thesis. The simulations presented in this thesis were conducted by the crystal plasticity simulation using a spectral method. The fundamental theory for crystal plasticity modelling is continuum mechanic that deals with the analysis of the mechanical behaviour of crystalline materials. Below continuum mechanics, the relationship between stress and strain is governed by constitutive models. The evolution of damage interface is solved by a novel phase field damage model which has been introduced recently. Finally, the spectral method is briefly presented which has been developed in recent decade to solve the mechanical boundary value problems for the crystal elasto-viscoplasticity at finite strains.

4.1 Continuum mechanics

Continuum mechanics considers the modeled materials as a continuous mass of that the substance completely fills the space rather than discrete particles. It uses linear algebra to describe the strains in objects and relate them to the resulting stresses. Figure 3.1 shows an object in both its undeformed and deformed states. The mechanical behaviour of the object from undeformed state to deformed state is described by the kinematics. The undeformed configuration could be also called the reference configuration which does not depend on time. The deformed configuration is time-dependent deformed state and is also called the current configuration. In assumption, both configurations use the same coordinate system with the same unit vectors. Therefore, if we define the location of the material points in the reference configuration

by vector $\boldsymbol{x}$ and in the current configuration by vector $\boldsymbol{y}$, we could describe the deformation in both configurations.

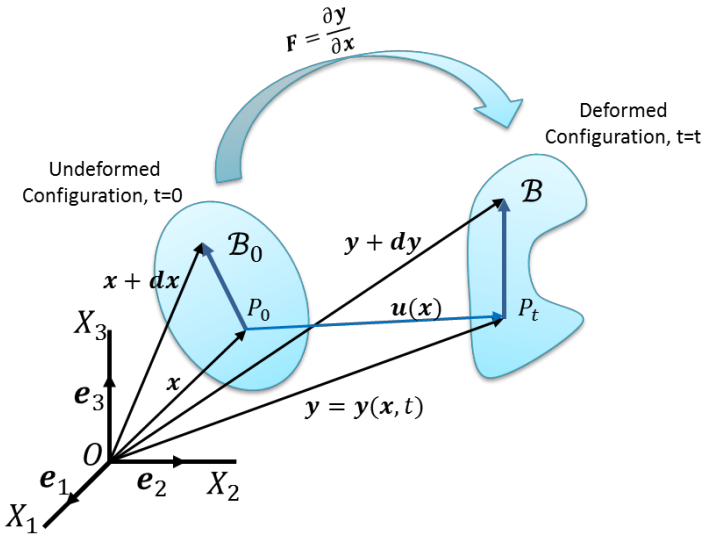

Fig. 4.1. The reference and current configurations.

The displacement of a material point could be described by a difference vector $\boldsymbol{u}$ from the location of a point in reference configuration to that in the deformed configuration:

$$\boldsymbol{u} = \boldsymbol{y} - \boldsymbol{x} \tag{4.1-1}$$

This leads to

$$\boldsymbol{y} = \boldsymbol{x} + \boldsymbol{u} \tag{4.1-2}$$

and the infinitesimal line segment $d\boldsymbol{x}$ in the neighbor of a material point in the reference configuration is transformed into the current configuration by:

$$\boldsymbol{y} + \mathrm{d}\boldsymbol{y} = \boldsymbol{y} + \frac{\partial \boldsymbol{y}}{\partial \boldsymbol{x}} \cdot \mathrm{d}\boldsymbol{x} + \boldsymbol{\mathcal{O}}(\mathrm{d}\boldsymbol{x}^2) \tag{4.1-3}$$

$d\boldsymbol{y}$ could be written as by neglecting terms of higher order:

$$\begin{gathered} \mathrm{d}\boldsymbol{y} = \frac{\partial \boldsymbol{y}}{\partial \boldsymbol{x}} \cdot \mathrm{d}\boldsymbol{x} = \boldsymbol{F} \cdot \mathrm{d}\boldsymbol{x} \\ \boldsymbol{F} = \frac{\partial \boldsymbol{y}}{\partial \boldsymbol{x}} \end{gathered} \tag{4.1-4}$$

where $\boldsymbol{F}$ is called deformation gradient. The deformation gradient tensor maps the vector $d\boldsymbol{x}$ in the reference configuration to the vector $d\boldsymbol{y}$ in the current configuration.

Therefore, it is a 2-point tensor. The inverse of the deformation gradient $\boldsymbol{F}^{-1}$, which "pull back" the vector element from the current to the reference configuration, is called the spatial deformation gradient in contrast to the "push forward" by the material deformation gradient $\boldsymbol{F}$.

$$\boldsymbol{F} = \frac{\partial(\boldsymbol{x} + \boldsymbol{u})}{\partial \boldsymbol{x}} = \boldsymbol{I} + \frac{\partial \boldsymbol{u}}{\partial \boldsymbol{x}} \tag{4.1-5}$$

$\boldsymbol{H} = \frac{\partial \mathbf{u}}{\partial \mathbf{x}}$ is called the displacement gradient which is also a 2-point tensor. The tensor $\boldsymbol{I}$ is the identity or unit matrix. Deformation gradient $\boldsymbol{F}$ and displacement gradient $\boldsymbol{H}$ are means of describing deformation of material points in continuum mechanics.

Normally, an object is not only stretched but also rotated under deformation. A pure rotation does not contribute to strain. So it is necessary to partition the stretch and rotation mechanisms out of $\boldsymbol{F}$ in order to determine stress and strain state. For the convenience of calculation and implementation, the tensor can be decomposed into a component of pure distortion and a pure rotation. For the deformation gradient, the decomposition reads as:

$$\boldsymbol{F} = \boldsymbol{V} \cdot \boldsymbol{R} = \boldsymbol{R} \cdot \boldsymbol{U} \tag{4.1-6}$$

Where $\boldsymbol{R}$ is the rotation matrix, $\boldsymbol{V}$ and $\boldsymbol{U}$ are symmetric matrices describing the deformation that is responsible for stress, strain, fatigue, cracks, fracture, etc. Note the process is read from right to left order. $\boldsymbol{V}$ is called the left stretch tensor and $\mathbf{U}$ the right stretch tensor. $\boldsymbol{F}$, $\boldsymbol{U}$ and $\boldsymbol{V}$ have the same JACOBIAN determinant (J). The strain measure depends on $\boldsymbol{V}$ or $\boldsymbol{U}$ only.

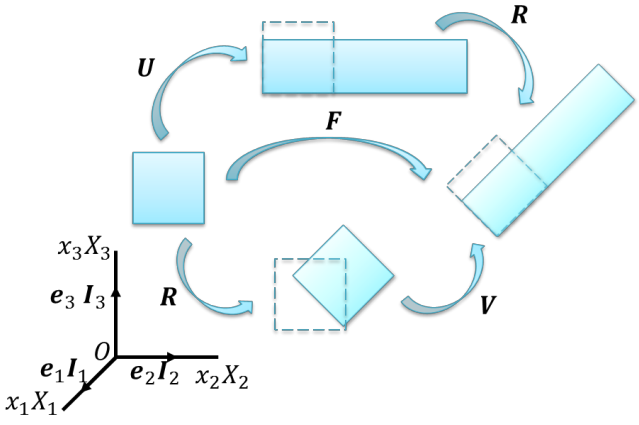

Fig. 4.2. Polar decomposition of deformation gradient.

To measure the strain during deformation, the change of the element length (i.e. a strain) can be expressed as:

$$\begin{aligned} d\boldsymbol{y} \cdot d\boldsymbol{y} - d\boldsymbol{x} \cdot d\boldsymbol{x} &= d\boldsymbol{x} \cdot (\boldsymbol{F}^T \cdot \boldsymbol{F}) \cdot d\boldsymbol{x} - d\boldsymbol{x} \cdot d\boldsymbol{x} \\ &= d\boldsymbol{x} \cdot (\boldsymbol{C} - \boldsymbol{I}) \cdot d\boldsymbol{x} \end{aligned} \tag{4.1-7}$$

$\boldsymbol{C} = \boldsymbol{F}^T \cdot \boldsymbol{F} = \boldsymbol{U}^2$ is a symmetric tensor completely in the reference configuration which is called the right CAUCHY-GREEN deformation tensor. $\boldsymbol{E}_0 = \frac{1}{2}(\boldsymbol{C} - \boldsymbol{I}) = \frac{1}{2}(\boldsymbol{F}^T \cdot \boldsymbol{F} - \boldsymbol{I})$ is called the GREEN-LAGRANGE strain tensor which is a valid strain measure completely in the reference configuration.

The change of length under a deformation expressed in the current configuration:

$$\begin{aligned} d\boldsymbol{y} \cdot d\boldsymbol{y} - d\boldsymbol{x} \cdot d\boldsymbol{x} &= d\boldsymbol{y} \cdot d\boldsymbol{y} - d\boldsymbol{y} \cdot (\boldsymbol{F}^{-T} \cdot \boldsymbol{F}^{-1}) \cdot d\boldsymbol{y} \\ &= d\boldsymbol{y} \cdot (\boldsymbol{I} - \boldsymbol{B}^{-1}) \cdot d\boldsymbol{y} \end{aligned} \tag{4.1-8}$$

$\boldsymbol{B}^{-1} = \boldsymbol{F}^{-T} \cdot \boldsymbol{F}^{-1}$ or $\boldsymbol{B} = \boldsymbol{F}^T \cdot \boldsymbol{F} = \boldsymbol{V}^2$ is a symmetric tensor completely in the current configuration which is called the left CAUCHY-GREEN deformation tensor. $\boldsymbol{E}_c = \frac{1}{2}(\boldsymbol{I} - \boldsymbol{B}^{-1}) = \frac{1}{2}(\boldsymbol{I} - \boldsymbol{F}^{-T} \cdot \boldsymbol{F}^{-1})$ is called the EULER-ALMANSI strain tensor which is a valid strain measure completely in the current configuration.

In continuum mechanics, to ensure that body deformed without developing any gaps or overlaps (i.e. compatible body), the deformation gradient field need to be determined under compatibility condition:

$$\boldsymbol{0} = \text{Curl}\, \boldsymbol{F} = \boldsymbol{\nabla} \times \boldsymbol{F} \tag{4.1-9}$$

Different stress measures exist depending on in which configuration the force and area are defined. In the current configuration, the CAUCHY traction $\boldsymbol{t}_c$ is defined by a force $\Delta \boldsymbol{r}_c$ acting on an area Δa_c with normal vector $\boldsymbol{n}_c$:

$$\boldsymbol{t}_c(\boldsymbol{n}_c) = \lim_{\Delta a_c \to 0} \frac{\Delta \boldsymbol{r}_c}{\Delta a_c} = \frac{\mathrm{d}\boldsymbol{r}_c}{\mathrm{d}a_c} \tag{4.1-10}$$

where $\boldsymbol{t}_c = \boldsymbol{\sigma} \cdot \boldsymbol{n}_c$, $\boldsymbol{\sigma}$ is the CAUCHY stress tensor which is a 2nd order tensor in spatial coordinates. If we transform the CAUCHY traction $\boldsymbol{t}_c$ into the traction $\boldsymbol{t}_{0,c}$ acting on the area in reference configuration $\mathrm{d}a_0$ but with the same resulting force $\mathrm{d}\boldsymbol{r}_c$, the relationship is followed as:

$$\mathrm{d}\boldsymbol{r}_c = \boldsymbol{t}_c \cdot \mathrm{d}a_c = \boldsymbol{t}_{0,c} \cdot \mathrm{d}a_0 \tag{4.1-11}$$

Where $\boldsymbol{t}_{0,c} = (J\,\boldsymbol{\sigma} \cdot \boldsymbol{F}^{-T}) \cdot \boldsymbol{n}_0$ follows the area vector relationship of $\mathrm{d}\boldsymbol{a}_c = J\,\boldsymbol{F}^{-T} \cdot \mathrm{d}\boldsymbol{a}_0$. Therefore, $\mathbf{P} = J\,\boldsymbol{\sigma} \cdot \boldsymbol{F}^{-T}$ is called the 1st PIOLA-KIRCHHOFF stress which is a non-symmetric 2-point tensor. The 1st PIOLA-KIRCHHOFF stress is energy conjugate to the deformation gradient $\boldsymbol{F}$.

If we pull back the resulting force $\mathrm{d}\boldsymbol{r}_c$ in the current configuration to the reference configuration, the stress measure can be determined in the reference configuration only:

$$\mathrm{d}\boldsymbol{r}_0 = \boldsymbol{F}^{-1} \cdot \mathrm{d}\boldsymbol{r}_c = \boldsymbol{F}^{-1} \cdot \boldsymbol{t}_{0,c} \cdot \mathrm{d}a_0 \tag{4.1-12}$$

Where $\boldsymbol{t}_0 = (J\,\boldsymbol{F}^{-1} \cdot \boldsymbol{\sigma} \cdot \boldsymbol{F}^{-T}) \cdot \boldsymbol{n}_0$ is the traction vector in the reference configuration. The tensor $\boldsymbol{S} = J\,\boldsymbol{F}^{-1} \cdot \boldsymbol{\sigma} \cdot \boldsymbol{F}^{-T}$ is called the 2nd PIOLA-KIRCHHOFF stress tensor which a symmetric tensor of 2nd order.

To ensure the static equilibrium, the stress field in the large strain formulation need to satisfy the following equilibrium condition:

$$\mathbf{0} = \mathrm{Div}\,\boldsymbol{P} = \boldsymbol{\nabla} \cdot \mathbf{P} \tag{4.1-13}$$

4.2 Crystal plasticity model

Crystal plasticity (CP) model deals with the deformation response of a crystalline materials to an external load. This relationship is described by the constitutive law in a CP model. In continuum mechanics, the total deformation gradient, $\mathbf{F} = \frac{\partial \mathbf{y}}{\partial \mathbf{x}}$, can be multiplicatively decomposed as (Lee, 1969; Reina and Conti, 2014):

$$\boldsymbol{F} = \boldsymbol{F_e F_p} \tag{4.2-1}$$

where $\boldsymbol{F}_e$ is the elastic part of the deformation gradient that describes both the elastic stretches and the rigid-body rotation. $\boldsymbol{F}_p$ is the plastic part of the deformation gradient that is due to crystallographic slip and also other mechanisms. It should be noted that $\boldsymbol{F}_p$ in general can be partitioned into polar decomposition as $\boldsymbol{F}_p = \boldsymbol{R}_p \cdot \boldsymbol{U}_p$, which implies that $\boldsymbol{F}_p$ does include a rotational part.

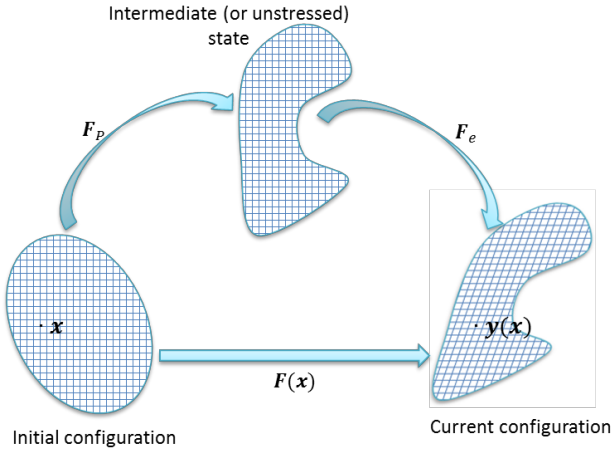

Fig. 4.3. Successive decomposition of deformation gradient of a body.

As shown in Fig. 4.3 above, the total deformation gradient is decomposed into a reference configuration, an intermediate configuration and a current configuration. The intermediate configuration is also called the relaxed configuration due to the undistorted lattice structure at this stage. The plastic deformation gradient $\boldsymbol{F}_p$ projects a material point from the reference configuration to the intermediate configuration. Correspondingly, the elastic deformation gradient $\boldsymbol{F}_e$ maps the point from the intermediate configuration to the current configuration. However, the real deformation process does not correspond to this kind of decomposition order. We utilize this

decomposition for computational convenience.

For elastic deformation, linear elasticity is assumed. The 2nd PIOLA-KIRCHHOFF stress is determined by its relationship with the elastic GREEN-LAGRANGE strain and the anisotropic elastic stiffness $\mathbb{C}$:

$$\boldsymbol{S} = \mathbb{C}\,(\boldsymbol{F_e}^{T}\boldsymbol{F_e} - \boldsymbol{I})/2 \tag{4.2-2}$$

The stress $\boldsymbol{S}$ acts as the driving force for the plastic deformation. During the deformation and movement of a material body, the material velocity field reads as:

$$\boldsymbol{v} = \frac{\boldsymbol{du(x)}}{\boldsymbol{dt}} = \dot{\boldsymbol{u}} = \dot{\boldsymbol{y}} \tag{4.2-3}$$

where $\dot{\boldsymbol{u}} = \dot{\boldsymbol{y}}$ holds because of the static reference configuration, i.e, $\frac{\mathrm{d}\boldsymbol{x}}{\mathrm{d}t} = 0$. Therefore, the spatial gradient of the velocity field is:

$$\boldsymbol{L} = \frac{\boldsymbol{\partial v}}{\boldsymbol{\partial y}} = \dot{\boldsymbol{F}} \cdot \boldsymbol{F^{-1}} \tag{4.2-4}$$

where $\boldsymbol{L}$ is called the velocity gradient. Due to the decomposition of deformation gradient, the plastic velocity gradient $\boldsymbol{L_p}$ is determined in the intermediate configuration following eq.(4.2-4):

$$\boldsymbol{L_p} = \dot{\boldsymbol{F}}_{\boldsymbol{p}} \cdot \boldsymbol{F_p^{-1}} = \boldsymbol{f}(\boldsymbol{S}, \boldsymbol{\xi}, \dots) \tag{4.2-5}$$

where $\boldsymbol{L_p}$ is driven by the stress $\boldsymbol{S}$ and influenced by the underlying microstructure change represented by state variable vector $\boldsymbol{\xi}$ and possibly other variables. The function $\boldsymbol{f}$ is described in the used CP model. For all CP model, the resolved shear stress on slip system α is calculated from the applied stress depending on SCHMIDS law (Schmid and Boas, 1968):

$$\tau^{\alpha} = \mathbf{S} \cdot (\mathbf{b}^{\alpha} \otimes \mathbf{n}^{\alpha}) \tag{4.2-6}$$

where $\mathbf{S}$ is the applied 2nd Piola-Kirchhoff stress (eq.(4.2-2), $\mathbf{b}^{\alpha}$ and $\mathbf{n}^{\alpha}$ are unit vectors along the slip direction and slip plane normal, respectively. To describe the plastic behaviour of the crystalline material, the plastic velocity gradient $\mathbf{L}_\mathrm{p}$ is determined by the superposition of the slip shear rates $\dot{\gamma}^{\alpha}$ on each slip system.

$$\mathbf{L}_{\mathrm{p}} = \dot{\mathbf{F}}_{\mathrm{p}}\mathbf{F}_{p}{}^{-1} = \sum_{\alpha} \dot{\gamma}^{\alpha}\, \mathbf{b}^{\alpha} \otimes \mathbf{n}^{\alpha} \tag{4.2-7}$$

Depending on the crystal structure, different slip systems are considered. In addition, the evolution function of the material state variable $\boldsymbol{\xi}$ is also defined specifically in the CP model:

$$\dot{\boldsymbol{\xi}} = \boldsymbol{g}(\boldsymbol{S}, \boldsymbol{\xi}, \dots) \tag{4.2-8}$$

The set of non-linear eqs.(4.2-1) to (4.2-5) are coupled to each other which need to be solved iteratively according to the calculation loop as shown in Fig. 4.4. More details about the iteration schemes for the state update are given by Kords (2013).

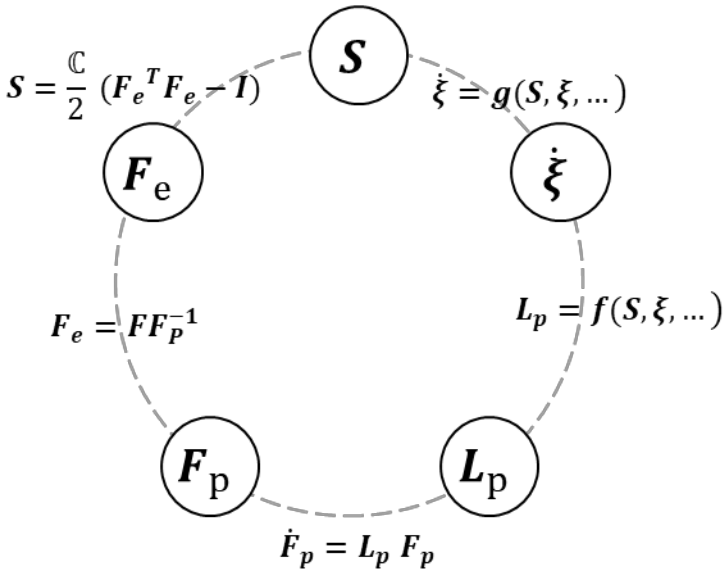

Fig. 4.4. Generalised elasto-viscoplastic calculation loop (Roters, 2011; Roters et al., 2012).

4.2.1 Phenomenological constitutive model

The phenomenological constitutive model is a conventional crystal plasticity model suggested by Rice (1971); Hutchinson (1976); Peirce et al. (1982); Peirce et al. (1983) for face-centered cubic (f.c.c) metallic crystals. This model usually uses a critical resolved shear stress g^{α} as state variable for each slip system α. The plastic deformation is assumed to occur on a slip system when the resolved shear stress exceeds a critical value. For f.c.c crystal these are twelve $\{111\}\langle\bar{1}10\rangle$ slip systems, for body-centered cubic (bcc) crystal these are twelve <111>{110} and twelve <111>{112} slip systems, respectively. The kinetic law of slip shear rate equation is given by

$$\dot{\gamma}^{\alpha} = \dot{\gamma^{0}} \left| \frac{\tau^{\alpha}}{g^{\alpha}} \right|^{n} \operatorname{sgn}(\tau^{\alpha}) \tag{4.2-9}$$

The plastic slip $\dot{\gamma}^{\alpha}$ on a slip system α occurs when the resolved shear stress τ^{α} exceeds a critical value g^{α} . The slip resistance values g^{α} evolve asymptotically towards g_{∞} as a function of the shear on other slip systems γ^{β} according to the relationship

$$\dot{g}^{\alpha} = \dot{\gamma}^{\beta} h_{0} \left| 1 - \frac{g^{\beta}}{g_{\infty}} \right|^{m} \operatorname{sgn}(1 - \frac{g^{\beta}}{g_{\infty}}) h_{\alpha\beta} \tag{4.2-10}$$

With initial hardening h_0 and a numerical strain hardening parameter m. The hardening matrix $h_{\alpha\beta}$ phenomenologically captures the interaction among the different slip systems. Eqs.(4.2-7) and (4.2-9) construct a detailed formulation for eq.(4.2-5) and eq.(4.2-10) constructs one for eq.(4.2-8).

4.2.2 Dislocation density based constitutive model

The dislocation density based constitutive crystal plasticity model (Jia et al., 2012b; Ma and Roters, 2004; Ma et al., 2006), implemented in the open source modeling framework DAMASK (Roters et al., 2018; Roters et al., 2012) is recapitulated briefly in the following.

The evolution law for the dislocation densities in this work follows the work of Ma and Roters (Ma and Roters, 2004). The selected model includes two processes that contribute to the evolution of the mobile dislocation density, namely multiplication as a source and dipole formation as a sink. The evolution of the dipole density is described following the work of Blum and Eisenlohr (Blum and Eisenlohr, 2009). The crystallographic shear rate of slip system α follows from the Orowan equation:

$$\dot{\boldsymbol{\gamma}}^{\boldsymbol{\alpha}} = \boldsymbol{\rho}_{\mathbf{sgl}}^{\boldsymbol{\alpha}} \mathbf{b} \mathbf{v}^{\boldsymbol{\alpha}} \tag{4.2-11}$$

with the unipolar dislocation density ρ_{sgl}^{α} and the length of the Burgers vector b. The velocity of the dislocation is calculated based on the assumption of a thermally activated motion through obstacles like forest dislocations:

$$\mathbf{v}^{\alpha} = \mathbf{v_0}\mathbf{exp}\left[\left(-\frac{\mathbf{Q_0}}{\mathbf{k_B T}}\left(\mathbf{1}-\frac{|\boldsymbol{\tau}^{\alpha}|}{\hat{\boldsymbol{\tau}}^{\alpha}}\right)^{\mathbf{p}}\right)^{\mathbf{q}}\right]\mathbf{sign}(\boldsymbol{\tau}^{\alpha}) \tag{4.2-12}$$

where v_0 is the dislocation velocity on the slip system when subjected to slip resistance $\hat{\tau}^{\alpha}$, Q_0 is the activation energy for dislocation slip, k_{B} is the Boltzmann constant, and T is the temperature, p and q are numerical parameters to adjust the obstacle profile, τ^{α} is the current resolved shear stress following eq.(4.2-6). The slip resistance (mechanical threshold stress) $\hat{\tau}^{\alpha}$ depends on the local dislocation densities and reads

$$\hat{\boldsymbol{\tau}}^{\boldsymbol{\alpha}} = \boldsymbol{\tau}_{\mathbf{solute}} + \mathbf{Gb}\left(\sum_{\boldsymbol{\alpha'}=\mathbf{1}}^{\mathbf{N_{slip}}} \boldsymbol{\xi}_{\boldsymbol{\alpha\alpha'}}\left(\boldsymbol{\rho}^{\boldsymbol{\alpha'}} + \boldsymbol{\rho}_{\mathbf{dip}}^{\boldsymbol{\alpha'}}\right)\right)^{\mathbf{1/2}} \tag{4.2-13}$$

where τ_{solute} is a constant glide resistance stemming from solid solution, **G** the shear modulus, ρ_{dip}^{α} the dipolar dislocation density, $\xi_{\alpha\alpha'}$ the interaction strength between different slip systems α and α'. The possible interaction types are self, coplanar, collinear, orthogonal, glissile, and sessile (Kubin et al., 2008). The shear modulus **G** is calculated as:

$$\mathbf{G} = \frac{C_{11}^{iso} - C_{12}^{iso}}{2} \text{ with } C_{11}^{iso} = \frac{3C_{11}+2C_{12}+4C_{44}}{5} \text{ and } C_{12}^{iso} = \frac{C_{11}+4C_{12}-2C_{44}}{5} \tag{4.2-14}$$

Comparing eq.(4.2-11) and (4.2-12) with eq.(4.2-9) and eq.(4.2-13) with eq.(4.2-10) shows the dislocation density based formulation allows a more detailed physical description of plastic behaviour.

4.3 Phase field damage model

The phase field model (PFM) derived for brittle fracture was recently successfully coupled with crystal plasticity constitutive laws (Shanthraj et al., 2016; Shanthraj et al., 2017b) to investigate the crack propagation process in the material under loading. Shanthraj et al. (2016) initially proposed and formulated this brittle fracture phase field approach for finite strain elasto-viscoplastic material, which is capable of successfully predicting physically realistic crack patterns when applied to a full field microstructure scenario and can be solved using a corresponding finite-element (FE) or spectral solver implementation. In the current study the model was further developed and implemented into a spectral method to handle the numerical solution of the coupled field equations (Shanthraj et al., 2017a). The phase field variable is a scalar non-local damage variable φ between the initially undamaged ($\varphi = 1$) and fully damaged, viz. open state ($\varphi = 0$). The damage evolution process is based on the variational theory of brittle fracture (Bourdin et al., 2000), and the method is closely related to gradient models employed in brittle (Bourdin et al., 2011; Kim et al., 2010) and ductile damage theory (Miehe et al., 2016). The stress relaxation associated with brittle damage is a result of a degradation of the material integrity and hence stiffness. The brittle damage evolution is driven by the continuous release of stored elastic energy at local material point, i.e. $\psi_E = \varphi^2 \mathbf{S} \cdot \mathbf{E}$ ($\mathbf{S}$: 2nd Piola-Kirchhoff stress, $\mathbf{E}$: elastic Green-Lagrange strain), from an undamaged state to a fully damaged state. As a resistance to the creation of crack surface, the associated damage surface energy takes the form of a Landau-type phase field approximation:

$$\psi_{surf} = \frac{G_0}{l_0}(1 - \varphi) + G_0 l_0 |\nabla \varphi|^2 \tag{4.3-1}$$

where ψ_{surf} is scaled by the effective interface thickness, l_0, and critical energy density, G_0/l_0, of the interfacial region, and G_0 is associated with the fracture energy. In the current work, the initiation of local damage nucleation is dependent on the critical energy density, which is referred to as critical strain energy $W_e^{crit} = G_0/l_0$.

On the kinetic side, φ is modelled as a non-conservative phase field. The evolution of φ is resulted from the relaxation of the total free energy according to the classical (time-dependent) Ginzburg-landau model (Allen and Cahn, 1979):

$$\dot{\varphi} = -M\left[2\varphi\mathbf{S}\cdot\mathbf{E} - \frac{G_0}{l_0} - \nabla G_0 l_0 \nabla\varphi\right] \tag{4.3-2}$$

with mobility *M*. Details about the phase field damage model and its coupling with crystal plasticity are described in Refs. (Shanthraj et al., 2016; Shanthraj et al., 2017b).

4.4 Spectral method

To resolve the numerical solution of intricate heterogeneous deformation fields for (static) equilibrium (eq.(4.1-13)) and strain compatibility (eq.(4.1-9)) under the given boundary conditions (BCs), the efficient and fast spectral method (Eisenlohr et al., 2013; Shanthraj et al., 2015) based on fast FOURIER transform (FFT) was used in this thesis instead of the well-established crystal plasticity finite element method (CPFEM) (Beaudoin et al., 1996; Becker, 1991; Harren et al., 1988; Mika and Dawson, 1998; Peirce et al., 1982; Roters et al., 2010; Sachtleber et al., 2002; Zhao et al., 2008). The use of a spectral method for solving the mechanical boundary value problem was pioneered by Moulinec and Suquet (Moulinec and Suquet, 1994, 1998), was developed further by Lebensohn (Lebensohn, 2001) and has been since developed further in computational material mechanics (Lebensohn et al., 2012; Lee et al., 2011). There are mainly two advantages of the spectral method. One is its straightforward use of periodic geometry of regularly arranged points. Such a geometry feature is not only convenient for generation of representative volume element (RVE) but can also be implemented without having to treat explicit border effects. The other advantage is its improved computational efficiency of heterogeneous materials compared to finite element method (FEM) because of its use of trigonometric polynomials as ansatz functions and also its repetitive operation of a fast FOURIER transform (FFT) which allows for a very time- and memory-efficient iterative solution algorithm (Eisenlohr et al., 2013). This efficiency of spectral method over FEM has been demonstrated by previous studies (Eisenlohr et al., 2013; Liu et al., 2010; Prakash and Lebensohn, 2009). For the application to heterogeneous materials with large contrast of local properties, the convergence was improved and accelerated greatly by several approaches developed in recent years, such as accelerated scheme (Eyre and Milton, 1999), augmented Lagrangian scheme (Lebensohn et al., 2013; Michel et al., 2000), polarization-based scheme (Monchiet and Bonnet, 2011) and efficient alternatives to the fix-point method (Brisard and Dormieux, 2010; Zeman et al., 2010). The recent improvement of the computational efficiency of the spectral solver as coded in DAMASK (Shanthraj et al.,

2015), make it particularly suited for heterogeneous materials with large local stiffness contrast among the adjacent phases. In this thesis, the advanced constitutive laws which couple crystal plasticity and/or phase field damage model was used to simulate co-deformation of heterogeneous materials. Incorporating the above-mentioned advantages of spectral method, systematic study with large number of individual simulations can be conducted efficiently at low computational costs.

5 Simulation setup

5.1 Fe-TiB_2 MMCs for particle damage simulation

To investigate the microstructural influence on particle damage in Fe-TiB_2 MMCs, different variations related to the particle clustering degree, particle size and particle volume fractions were studied. Simulations were performed with a coupled phenomenological crystal plasticity model (section 4.2.1) and phase field damage model (section 4.3) by the multi-physics simulation package DAMASK (Roters et al., 2018; Roters et al., 2012). A spectral solver (section 4.4) was employed to solve the mechanical boundary value problem and the governing phase field kinetic evolution predicting the initiation and growth of particle damage. The simulation setup presented in this section is published by Wang et al. (2018b).

5.1.1 Generation of the particle microstructure

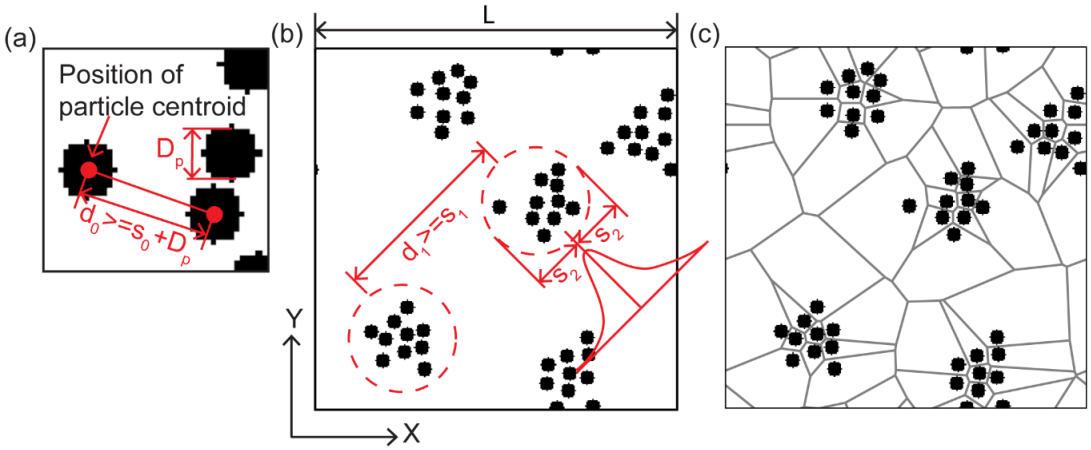

Fig. 5.1. Schematic of composite microstructure: (a) particle geometry, (b) microstructure of clustered distribution and (c) its Voronoi tessellation.

To investigate the effects of different particle parameters on particle damage behaviour, several types of particle microstructures were generated. In this study, two-

dimensional periodic composite microstructures are built with simplifications such as uniform particle size, circular particle shape and single crystal ferritic matrix. For generating a random reference distribution, the particle centroid position (the red point indicated in the Fig. 5.1a) was placed in the matrix following the random sequential adsorption (RSA) algorithm (Rintoul and Torquato, 1997; Segurado et al., 2003; Segurado and Llorca, 2006). This process is expressed as: $d_0 = \left|\left|\boldsymbol{x_i} - \boldsymbol{x_j} + \boldsymbol{h}\right|\right| \geq s_0 + D_p, \boldsymbol{h} = (h, k)$, where h, k can assume the values 0, L, -L, where L is the side length of the modelled RVE geometry. The position of the particle centroid i is placed at a distance exceeding the sum of minimum interparticle distance s_0 and particle diameter D_p from other particles j in the matrix. The term D_p added on the right side is for applying the boundary condition that particles do not overlap. Besides this, the vector term $\boldsymbol{h}$ added on the left side is for implementing periodic boundary conditions of the RVE. That is, the particles being placed near to the RVE edge should also meet the minimum distance requirement from the particles adjacent to the opposite RVE edge. For generating an RVE with a clustered distribution of the hard inclusions (Fig. 5.1b), several cluster centroids N_c are placed at a minimum cluster distance s_1 using the same RSA process. About each cluster centroid, a specific number of particles N_{pc} are placed at distances derived in a way so as to match a normal distribution (Myles et al., 1995; Yang et al., 2001) with standard deviation s_2. This inter-cluster arrangement protocol also considers a certain prescribed minimum particle distance s_0 and periodic boundary conditions of RVE. Following these topological rules, the modelled particle microstructures can be well controlled in its key statistical features by adjusting these geometrical factors.

5.1.2 Inhomogeneity quantification of the particle distribution

The degree of inhomogeneity of the generated particle distributions was quantified in terms of the coefficient of variance of the mean near-neighbour distance (COV_d). Boselli and Yang et al. (Boselli et al., 1999; Yang et al., 2001) found that the COV_d value, derived from a finite-body tessellation, was very sensitive to inhomogeneity

variations but essentially independent of particle morphology, size, orientation and volume fraction. In this thesis, Voronoi/Dirichlet tessellation was used to identify the near and nearest particle neighbours (Fig. 5.1c) and calculate the corresponding particle spacing based on the tessellation method used. COV_d is defined as:

$$COV_d = \frac{{s_d}^2}{d} \quad (1).$$

where ${s_d}^2$ is the variance of the mean near-neighbour distances of all particles and d is the average of the mean near-neighbour distances. The higher the COV_d, the more "clustered" the particles are. For a random particle distribution, the COV_d value is close to 0.36 (Ayyar et al., 2008; Yang et al., 2001).

5.1.3 Model parameters and boundary conditions

To simulate particle-induced damage in Fe-TiB_2 MMCs, the phase field model of brittle fracture and the crystal plasticity Fast Fourier Transformation simulation were coupled in this thesis. The elastic stiffness parameters of TiB_2 (Table 5.1-1) were taken from first-principles pseudo-potential calculations by Milman and Warren (2001). From that the fracture interface energy of the TiB_2 particles was calculated as $G_0 = {K_{IC}}^2/_E \approx 68\ ^J/_{m^2}$, where K_{IC} is the fracture toughness (around 6.2 MPa.$m^{1/2}$ from Munro (2000)) and E is the Young's modulus (about 565GPa at 23°C (ArcelorResearchGroup, 2008; Milman and Warren, 2001; Shurin and Panarin, 1974)) of the TiB_2 particles. The effective damage interface thickness l_0 was taken as 0.5µm, corresponding to 2 Fourier points in the modelled geometry. Hence, the critical strain energy for damage nucleation is $W_e^{crit} = \frac{G_0}{l_0} = 1.36 \times 10^8 \cdot \frac{J}{m^3}$.

The phenomenological crystal plasticity model was used for the Fe-α matrix and the material parameters were adopted from earlier works (Diehl et al., 2016; Tasan et al., 2014a; Tasan et al., 2014b), Table 5.1-2. The modelled 2D square composite representative volume element is discretized into an equidistance grid of $250 \times 250 = 62{,}500$ Fourier points (FPs), i.e. $N_X \times N_Y$ where $N_{X,Y}$ are the counters of the FPs along the **X** and **Y** directions, respectively, thus the side length of the RVE geometry amounts

to L = 250 FPs. All the simulations were conducted under uniaxial tensile loading along the **X** direction. Uniaxial tension was applied at a rate of 0.01 s^{-1} with a time step of 0.01 s.

Table 5.1-1: Values of the elastic stiffness of TiB_2 (Milman and Warren, 2001)

Property		Value	Unit
Elastic Constants for HCP lattice structure	C_{11}	656	GPa
	C_{12}	66	GPa
	C_{13}	98	GPa
	C_{33}	461	GPa
	C_{44}	259	GPa
	C_{66}	295	GPa
The ratio of lattice constants	c/a	1.0629	

Table 5.1-2: Crystal plasticity constitutive parameters of the elastic and plastic response of the ferrite matrix (Diehl et al., 2016; Tasan et al., 2014a; Tasan et al., 2014b)

Property		Value	Unit
Elastic Constants for BCC lattice structure	C_{11}	233.3	GPa
	C_{12}	135.5	GPa
	C_{44}	118.0	GPa
Reference shear rate	$\dot{\gamma}_0$	0.001	s^{-1}
Initial and saturation slip resistance on {110} or {112} slip family, respectively	$g_0, \{110\}$	95	MPa
	$g_\infty, \{110\}$	222	MPa
	$g_0, \{112\}$	97	MPa
	$g_\infty, \{112\}$	412	MPa
Initial hardening	h_0	1	
Interaction coefficients	Coplanar $h_{\alpha\beta}$	1	
	Non-coplanar $h_{\alpha\beta}$	1.4	
Inverse shear rate sensitivity	n	20	
Numerical parameter	m	2.25	

5.2 Nickel single crystal for deformation patterning simulation

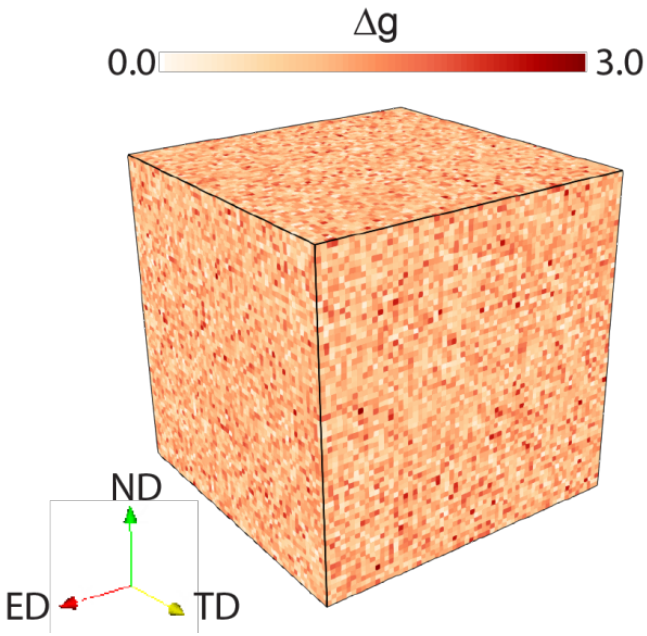

Fig. 5.2. The initial geometry: the misorientation ($\boldsymbol{\Delta g}$) field of the modeled cubic volume element consisting of $\mathbf{64 \times 64 \times 64 = 262,144}$ Fourier points. The orientation sactter half-width is 6° around copper orientation $(\mathbf{112})[\mathbf{11\bar{1}}]$ prior to loading.

To investigate the reasons for DBs patterning, crystal plasticity simulations of an f.c.c nickel single crystal with initial near-Copper orientation deformed in plane strain compression were conducted in this thesis. The simulation setup presented here is published by Wang et al.(2018a). Fig. 5.2 shows the modeled 3D cubic single crystal volume element discretized into an equidistant grid of $64 \times 64 \times 64 = 262{,}144$ FPs ($N_{ED} \times N_{TD} \times N_{ND}$ where $N_{ED,TD,ND}$ are the numbers of FPs along elongation direction (ED), transverse direction (TD), and normal direction (ND) respectively). Since the employed crystal plasticity model is a local model, i.e. the behaviour of a given point does not depend on the constitutive state of its neighbors, the physical size is of no importance and for simplicity a unit size of $1\ \text{a.u.} \times 1\ \text{a.u.} \times 1\ \text{a.u.}$ is assigned to the cube (a.u.: arbitrary unit).

Previous studies showing that banding is initiated stochastically from small

perturbations in lattice orientation (Arul Kumar and Mahesh, 2012; Mahesh, 2006). Following this hypothesis, a perturbed lattice is assumed in this study. To this end, each material point in RVE gets an individual initial orientation assigned, which deviates from the Copper-orientation $(112)[11\bar{1}]$ such that the overall crystallographic texture shows a total orientation scatter of 6° full width at half maximum (FWHM) (Raabe and Roters, 2004; Raabe et al., 2004). Following Raabe and Roters (Raabe and Roters, 2004), a rejection sampling algorithm is used to obtain a Gaussian misorientation distribution around the nominal orientation from a random, uniform one. For a FWHM of 6°, more than 95 percent (2.4 times the standard deviation) of all orientation have a misorientation of less than 3°. Hence, the perturbations are small and spatially uncorrelated.

The crystal plasticity model based on dislocation density evolution (section 4.2.2), implemented in the open source modeling framework DAMASK (Roters et al., 2018; Roters et al., 2012), was used. The material parameters (Table 5.2-1) used to model the nickel behaviour are taken from a simulation study on indentation in single-crystalline nickel, where a very good agreement with experimental results was achieved when a similar constitutive model (Reuber et al., 2014) was used. Plane strain compression was applied along ND at a strain rate of $0.001\ s^{-1}$ until a final strain of 5.5% in loading direction is reached. As it is inherent to the spectral method solution, periodic boundary conditions are applied, i.e. the applied loading rate is a volume average and the same holds for the vanishing displacement along TD and stress along ED.

Table 5.2-1: Constitutive parameters of single-crystalline nickel used for the present simulation.

Property		Value	Unit	Ref.
Elastic Constants for FCC lattice structure	C_{11}	246.5	GPa	Hirth and Lothe (1982)
	C_{12}	147.3	GPa	Hirth and Lothe (1982)
	C_{44}	124.7	GPa	Hirth and Lothe (1982)
Burgers vector length	b	0.248	nm	Cordero et al. (2008)
Initial dipole density	$\rho_{dip,0}$	1.0	m^{-2}	
initial dislocation density	$\rho_{sgl,0}$	$2.88 \cdot 10^{12}$	m^{-2}	
Dislocation glide activation energy	Q_0	$1.8 \cdot 10^{-19}$	J	
Glide velocity	v_0	10^{-4}	$m\,s^{-1}$	
Solid solution strength	τ_{solute}	8.3	MPa	
Bulk diffusion coefficient	D_0	$1.9 \cdot 10^{-4}$	$m^2 s^{-1}$	Gottstein (2004)
Dislocation climb activation energy	Q_{sd}	$5.1 \cdot 10^{-19}$	J	
Exponent parameter	p, q	1.0		

Interaction type	Self	Coplanar	Collinear	Orthogonal	Glissile	Sessile
Interaction coefficient (from Kubin et al. (2008))	0.122	0.122	0.625	0.07	0.137	0.122

6 Particle-induced damage in Fe –TiB_2 metal matrix composite steels[1]

This chapter is the results for the first study subject of this thesis. The aim of this study is to derive the optimal particle configuration guidelines for the production of Fe – TiB_2 HMS an optimized property profile, namely to maximize the composites ductility by tailoring the particle microstructure to minimize damage under loading. The effects of different particle parameters, such as spatial distributions, size and volume fraction, on particle damage initiation were systematically investigated by conducting tensile loading in crystal plasticity Fast Fourier transformation simulation coupled with phase field damage model, deriving the variation of initial particle damage behaviour as function of different microstructural parameters.

6.1 Example of damage simulation analysis

The crystal plasticity simulations coupled with the phase field damage model are capable of predicting the particle damage process in the composite microstructure. This is revealed by an example of the simulated particle damage patterns (as shown in Fig. 6.1). It shows that the initial particle damage (Fig. 6.1a), i.e. the earliest particle fracture occurs at a macroscopic strain level of 24.61% translating to microscopic strain levels up to around 100%. The damage area inside the particles, where the local damage variable φ drops to zero, is shown in black color. To reveal the details of the individual particle damage events, the areas around the fractured particles are highlighted in the local enlarged images and the positions of the particle damage are indicated by the black

1 The results of this study are published by Wang et al.(2018b).

arrows. To give a micromechanical analysis of the earliest particle fracture event, the corresponding von Mises true stress distributions are drawn in the same enlarged area at the loading step just before and after particle crack (Fig. 6.1a). The step before particle crack is the stage before the local damage variable φ starts to decrease below 1.0. At this step, a maximum stress point of about 6.63GPa is found inside the particle which will induce the earliest damage event. After particle crack, the stress inside the particle decreases, especially for the damaged area where the minimum stress point is found. After the initial fracture of one particle others also break in adjacent microstructure regions as highlighted in Fig. 6.1b. With further loading, particle damage also spreads to other areas as indicated in Fig. 6.1c and d. At a macroscopic strain level of 24.94% (Fig. 6.1d), about 55% of all particles are fractured. This process corresponds to the particle damage process observed in the damage evaluation experiment of the Fe – TiB_2 HMS (Hadjem-Hamouche et al., 2012).

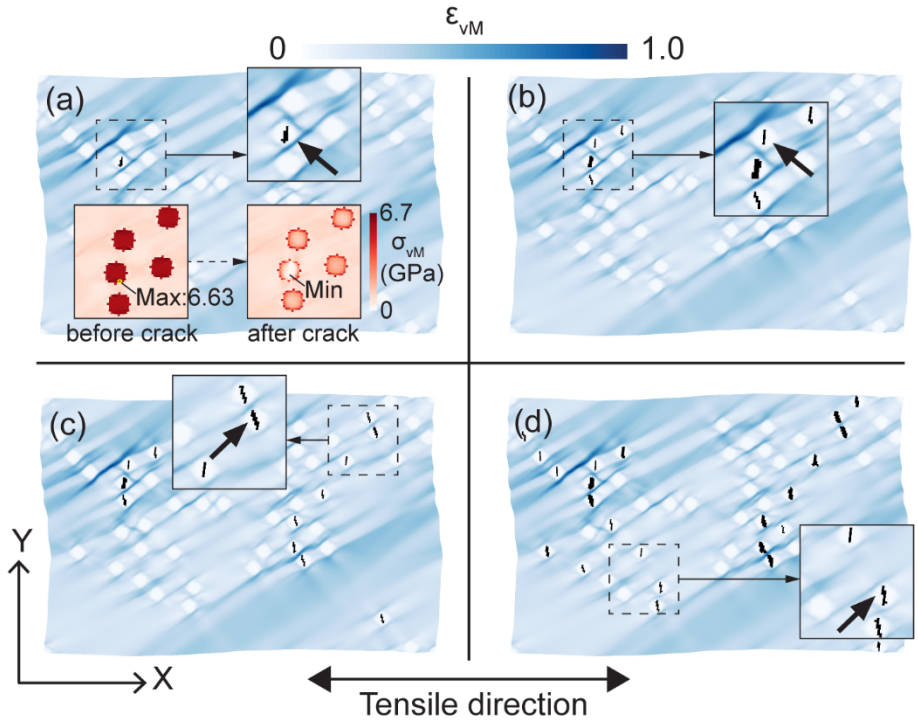

Fig. 6.1. Patterns of progressive particle damage (black area) coupled with von Mises true strain ε_{vM} distributions at successive global strains of: (a) 0.2461; (b) 0.2467; (c) 0.2473; (d) 0.2494. In (a), the von Mises true stress σ_{vM} distributions of the area including the earliest damage event are drawn at the loading step just before and after particle crack. The maximum stress point inside the particle before crack and the minimum stress point inside the particle after crack are indicated. The heterogeneity degree of the modelled microstructure is $COV_d \approx 0.55$ and the particle size is $D_p=0.04L$, where L is the side length of

the RVE geometry. The details of particle damage are highlighted in magnified images and indicated by black arrows. The white blocky regions indicate positions where the hard particles are located.

To reveal the load transfer from matrix to particle, the average von Mises stress versus Global von Mises strain curves for the TiB_2 particle, Fe-α matrix and Fe – TiB_2 composite of this simulation example are plotted respectively (Fig. 6.2). It shows the average stress of the TiB_2 is one magnitude higher than that of the matrix. The non-linearity in the evolution of stress for TiB_2 is observed once the Fe-α matrix plastically deformed. The decrease of stress for TiB_2 is due to particle damage process.

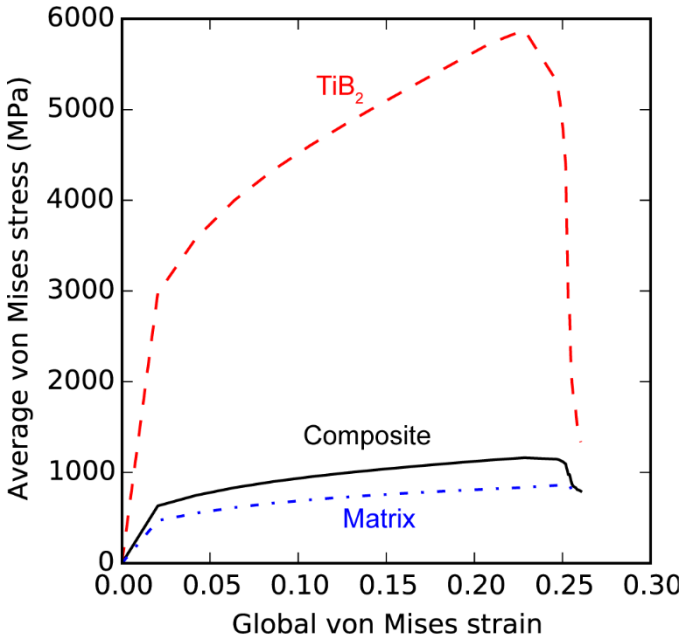

Fig. 6.2. Average von Mises stress versus Global von Mises strain for the TiB_2 particle, Fe-α matrix and Fe – TiB_2 composite.

6.1.1 Evaluation of initial particle damage

Various sets of particle microstructures were generated to study the effects of specific morphological parameters such as the degree of clustering, the average particle size and the volume fraction. Here, the process of initial particle damage was evaluated specifically to show the influence of these microstructure parameters. An initial particle damage event is revealed by the drop of the minimum damage field value φ_{min} to the minimum value of zero. For evaluating this process, three characteristic values are extracted from the simulations as shown in Fig. 6.3. These are the instability strain, the initial damage strain and the damage incubation strain. The instability strain ε_I is the

global strain value where the minimum damage value φ_{min} starts to decrease below 1.0. This means at this strain level the particle becomes mechanically instable and particle fracture is initiated. The initial damage strain ε_D is the global strain value when the structure variable φ_{min} reaches zero, i.e. marks the load when the first part of an particle is fully fractured. This means that the fracture of the particle is completed and the associated flow stress of the composite decreases due to the stress release of the damaged particle. The damage incubation strain $\varepsilon_{Inc}=\varepsilon_D-\varepsilon_I$ is the strain measure which represents the difference among the two values before, i.e. it quantifies essentially how long the decohesion took from its onset until total particle fracture. Fig. 6.3 shows the characteristic values ε_D and ε_{Inc} and how they develop as a function of certain microstructure parameters which will be identified in the ensuing analysis. Such mechanisms are then used as a basis to identify the governing micromechanical structure-property relations which in turn provide improved design guidelines for HMS with good ductility.

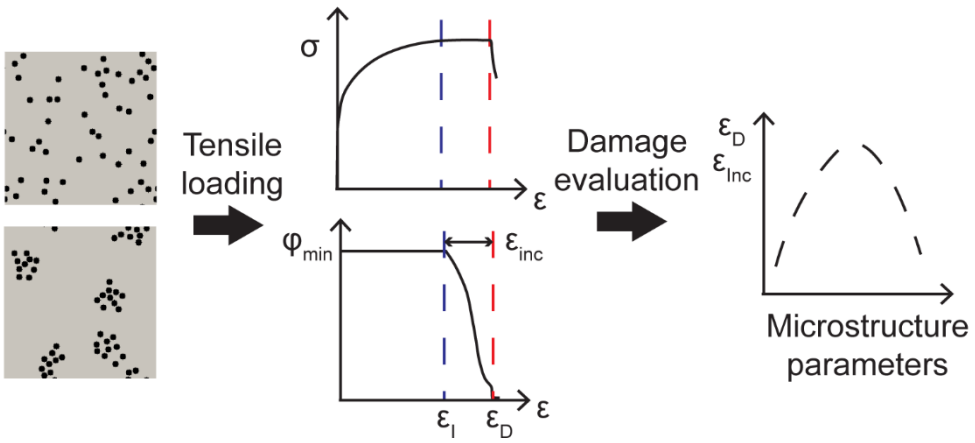

Fig. 6.3. Damage evaluation of the initial particle damage process in the simulations. From the evolution curve of the minimum damage field variable φ_{min} with global strain ε, three characteristic values were derived: the instability strain ε_I , the initial damage strain ε_D and the damage incubation strain ε_{Inc}. The characteristic values ε_D and ε_{Inc} are here exemplarily plotted as a function of certain microstructure parameters which are derived in the following analysis.

6.2 Simulation results

6.2.1 Increasing the degree of particle clustering

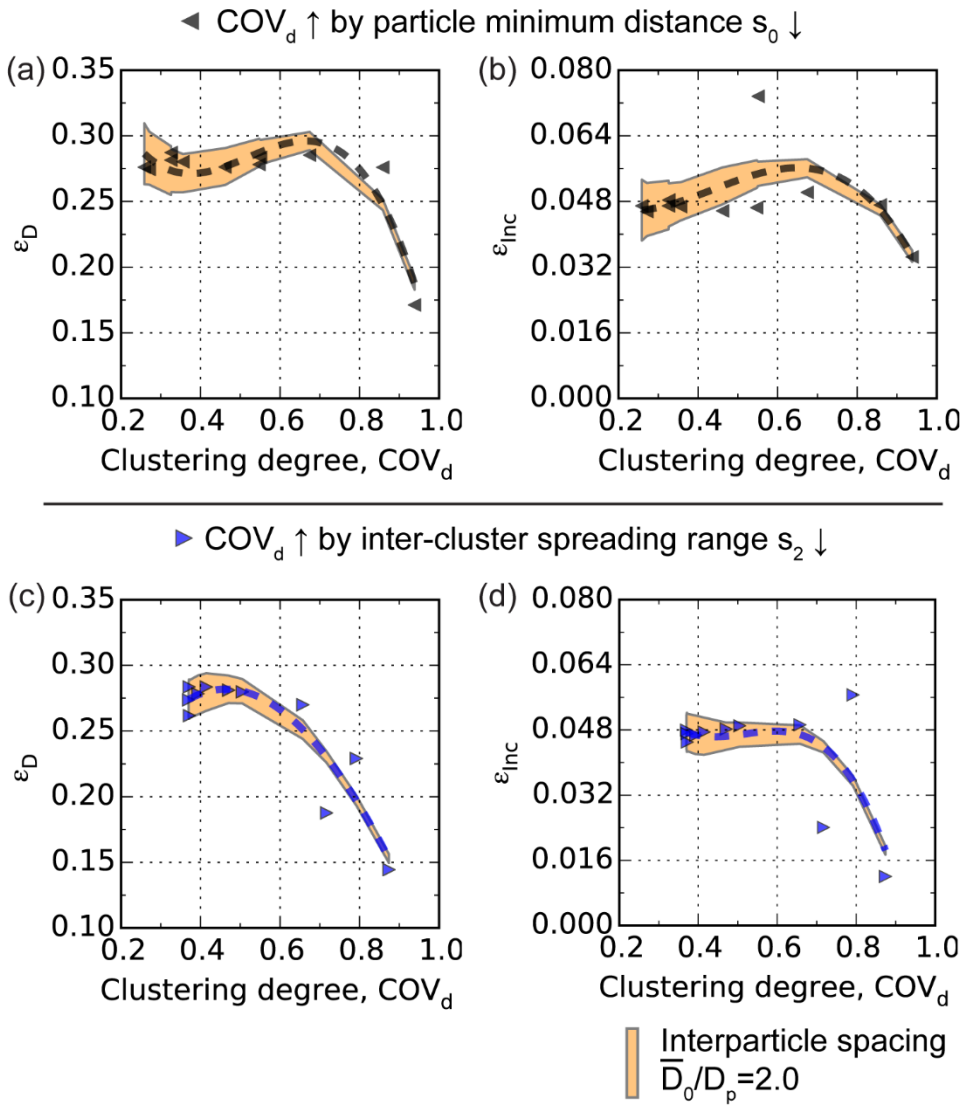

Fig. 6.4. The initial damage strain ε_D and damage incubation strain ε_{Inc} as function of the particle clustering degree COV_d. The increase of the clustering degree was achieved by either concentrating particles towards each other (a, b), or by shrinking the cluster size (c, d). The average interparticle spacing of the particle distribution is qualitatively represented by the height of the orange area. The reference height of the orange area, which is in the bottom of the figure, corresponds to $\overline{D}_0 = 2D_p$.

To study the clustering degree effect, the change in the particle spatial distribution was considered while keeping the particle size and particle number constant. The relative particle diameter is $D_p = 0.04L$, where L is the side length of the modelled RVE geometry. The total particle number is 50 with 5 clusters i.e. each cluster contains 10

particles. In this study, the inhomogeneity degree COV_d (section 5.1.2) is used to quantify the clustering degree of particle distribution. The values of the particle size and particle numbers were varied so as to cover a large range of the clustering degree COV_d from about 0.26 to 0.94. The minimum cluster distance s_1 was set to $6D_p$. An increase of the clustering degree was achieved by either reducing the interparticle spacing or by shrinking the cluster size. The interparticle spacing decreases significantly from about $1.8D_p$ to nearly $0.2D_p$ with the increase of the clustering degree. For this microstructure change, the simulation results yield early and rapid particle fracture for the case of a high clustering degree. Fig. 6.4 quantifies this result in terms of the variation of the initial damage strain ε_D and damage incubation strain ε_{Inc} as function of the clustering degree COV_d. For cases of homogeneous and random particle distribution with COV_d values below 0.4, the initial damage strain ε_D stabilize in a range of about 0.27 and the damage incubation strain ε_{Inc} is about 0.048. Correspondingly for a clustering degree COV_d above 0.7 (interparticle spacing below $0.5D_p$), the trends of ε_D and ε_{Inc} (dashed lines) both decrease as the clustering degree increases. The trend of ε_D decreases to around 0.15 (at $COV_d \approx 0.87$ in Fig. 6.4c), i.e. about 50% lower strain values than that of homogeneous distributions. Meanwhile the trend of ε_{Inc} drops to nearly 0.016 (at $COV_d \approx 0.87$ in Fig. 6.4d), about 67% lower strain values. Thus, in view of such early damage instability for the case of a highly clustered distribution, a COV_d value above 0.7 can be regarded as a critical threshold value marking particle distributions that will lead to early and rapid particle damage.

6.2.2 Increasing the particle size

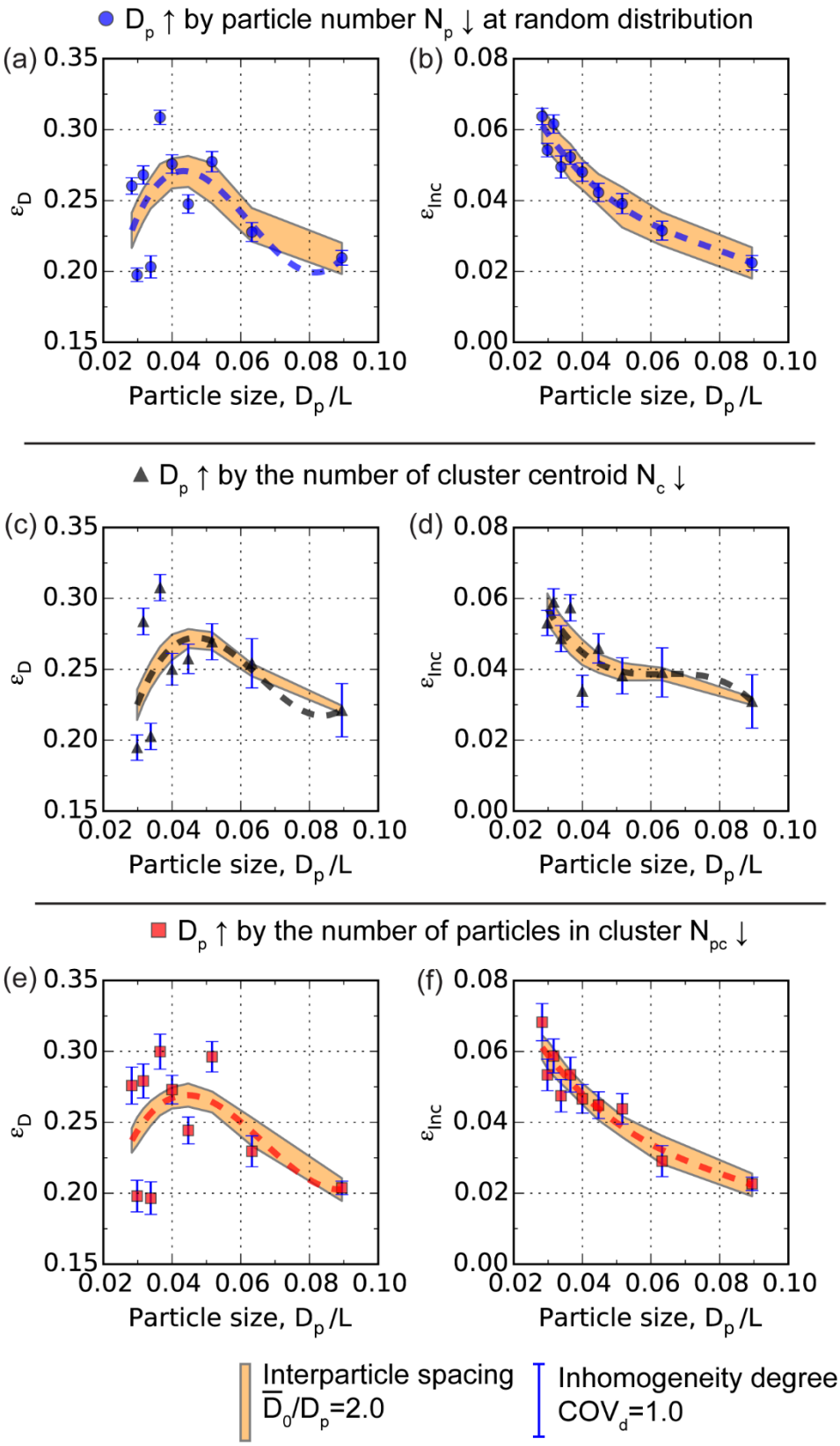

Fig. 6.5. The initial damage strain ε_D and damage incubation strain ε_{Inc} as function of the relative particle size D_p/L. The increase of particle size is associated with reducing the particle number under constant

volume fraction: (a, b) by reducing the particle number N_p at random distribution, (c, d) by reducing the number of cluster centroid N_c at inhomogeneous distribution, and (e, f) by reducing the number of particles about each cluster centroid N_{pc}. The average interparticle spacing $\overline{D}_0/D_p$ of the particle microstructure is qualitatively presented by the height of the orange area. The heterogeneity degree COV_d of the particle distribution is revealed by the length of blue error bar. Located in the bottom of the figure, the reference height of the orange area corresponds to $\overline{D}_0 = 2D_p$ and the reference length of the blue error bar represents COV_d=1.0.

By changing the particle size, we cannot avoid the associated change of particle number, especially under constant volume fraction. The combination of these variations will ultimately result in diverse distribution change which might as well affect particle damage behaviour. In real MMCs microstructure, the particle size change is always correlated with distribution change due to the specific physical and chemical reasons. For instance, in HMS, the large primary particles in 10μm tend to cluster together (Zhang et al., 2016) and the small eutectic particles with 1μm width are more likely to disperse homogeneously (Springer et al., 2015). Therefore, to simulate this change, diverse distributions were made for the study of particle size effect. As shown in Fig. 6.5, the inhomogeneity degree COV_d and the average interparticle spacing of the particle distribution are qualitatively presented by the length of blue error bar and the width of the orange area respectively. The particle size is described here as a ratio D_p/L (abscissa values in Fig. 6.5) where D_p is the particle diameter and L is the side length of modelled geometry. In this study, the particle size D_p increases from about 0.03L to 0.09L with the decrease of particle number from 100 to 10 under constant volume fraction. For the generation of the modelled particle microstructure, three different ways for the increase of particle size were considered: (i) by reducing the particle number N_p (from 100 to 10) in random distribution; (ii) by reducing the number of cluster centroids N_c (from 9 to 1, each cluster contains 10 particles) in the inhomogeneous distribution; and (iii) by reducing the number of particles about each cluster centroid N_{pc} (from 20 to 2, the number of cluster centroid N_c fixed at 5). In this way, almost each particle size can have three different distributions to compare.

Interestingly, quite similar values and trend of damage behaviour with particle size change were obtained from these three groups except for some differences caused by high clustering degree. Fig. 6.5 quantifies the results in terms of the variation of the initial damage strain ε_D and damage incubation strain ε_{Inc} as function of the particle size D_p/L. As shown in Fig. 6.5 a, c and e, the trend of ε_D (dashed lines) increases initially with fluctuation (about 0.1 strain values) to the peak value of about 0.27 at the particle diameter D_p range of 0.03~0.06L. The highest discrete point of ε_D is at the particle diameter of 0.037L. After the peak value, the trend of ε_D decrease continuously to about 0.2 with the increase of particle diameter from 0.06L to 0.09L. As shown in Fig. 6.5b, d and f, the trend of ε_{Inc} decreases monotonically from about 0.07 to 0.02 with the increase of particle diameter D_p from about 0.03L to 0.09L.

For the particle diameter D_p above 0.06L, it was found that in highly clustered distributions (i.e. COV_d above 0.7), the particles tend to fracture along a specific continuous pathway in the direction perpendicular to the tensile direction, namely the percolation phenomenon of particle damage. For example, it occurs in a modelled microstructure as shown in Fig. 6.6a. The detail of particle damage is highlighted in the magnified image and indicated by the black arrow. This is consistent with an experimental observation made on a ruptured tensile sample: The material probed here is a high modulus steel with 20 vol% TiB_2, prepared in a vaccum induction furnace under argon, cast into a 40mm thick water-cooled mould followed by hot rolling. Tensile tests were conducted along the rolling direction at a constant crosshead speed of 5 um s^{-1}, corresponding to an initial strain rate of 10^{-3} s^{-1}. The image of the area close to fracture surface was taken by a field emission scanning electron microscope (SEM; JEOL-6500F, operated at 15kV). As shown in the SEM image (Fig. 6.6b), in a longitudinal section close to the fracture zone, the damage percolation among the closely packed coarse particles is observed. The fracture of the coarse particles is highlighted in the enlarged image and indicated by the white arrow. This correspondence not only validates our simulation results, but also demonstrate that the clustered distribution with large particles tend to result in damage percolation during loading which might contribute much on the failure of MMCs.

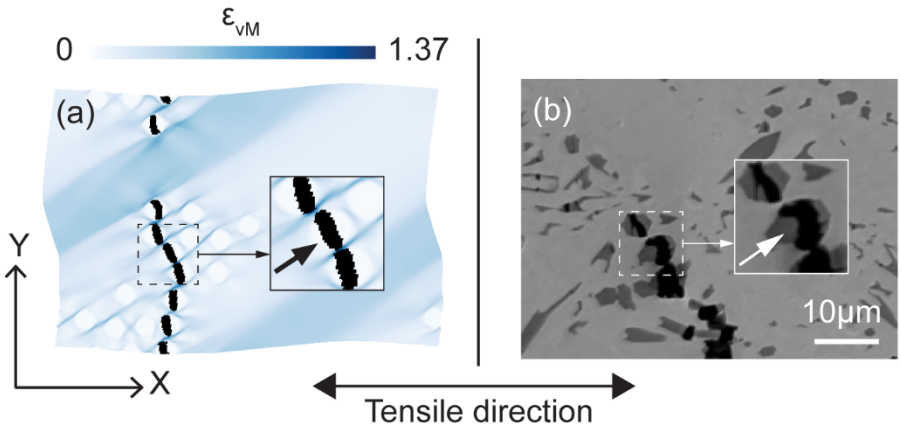

Fig. 6.6. Percolation of particle damage observed in simulations and also in experiment. (a) The simulated particle damage pattern (black area) is shown together with the von Mises equivalent strain ε_{vM} distribution at a macroscopic strain level of 23.02%. The heterogeneity degree of the modelled microstructure is $COV_d \approx 0.87$ and the particle size is $D_p=0.063L$. The detail of particle damage is highlighted in the magnified image and indicated by the black arrow. The white blocky regions indicate positions where the hard particles are located. (b) Experimental image showing damage percolation of fractured coarse particles in a longitudinal section close to the fracture zone. The total elongation is about 7%. The detail of particle damage is highlighted in the magnified image and indicated by the white arrow.

6.2.3 Increasing the particle volume fraction

To study the particle volume fraction effect, the increase of volume fraction was achieved by either increasing particle size or adding more particles in the matrix. For the Fe- TiB_2 HMS alloy, it should be noted that the characteristics of particle microstructures will be changed during increasing TiB_2 volume fraction and this was also considered in this study. For TiB_2 above 12 vol% (~6.3 mol%), the Fe-TiB_2 alloy is above the eutectic TiB_2 concentration (pseudo-binary eutectic reaction (Shurin and Panarin, 1974)) and as a consequence, the average particle size increases significantly as large primary particles resulted from primary solidification. In this study, such changes correspond to the first route (Fig. 6.7) of the increase of the particle volume fraction from 2.26vol% to 42.47vol% by increasing particle size D_p (from 0.024L to 0.104L, L is the side length of the modelled RVE geometry) in random and clustered distributions. For hypo-eutectic alloy with TiB_2 below 12vol%, the matrix contains fine eutectic TiB_2 particles of similar size (Baron et al., 2016). Thus, this corresponds to the second route (Fig. 6.8) of the increase of the particle volume fraction from 1.26vol%

to 12.57vol% by adding particles of constant diameter (D_p=0.04L) under different ways: (i) by increasing particle number from 10 to 100 at random distribution (Fig. 6.8 a and b), (ii) by increasing the number of cluster centroids N_c from 1 to 10 with each cluster containing 10 particles (Fig. 6.8 c and d) and (iii) by increasing the number of particles about each cluster centroid N_{pc} from 2 to 20 with the number of cluster centroid N_c fixing at 5 (Fig. 6.8 e and f). In this way, different particle distributions can be introduced.

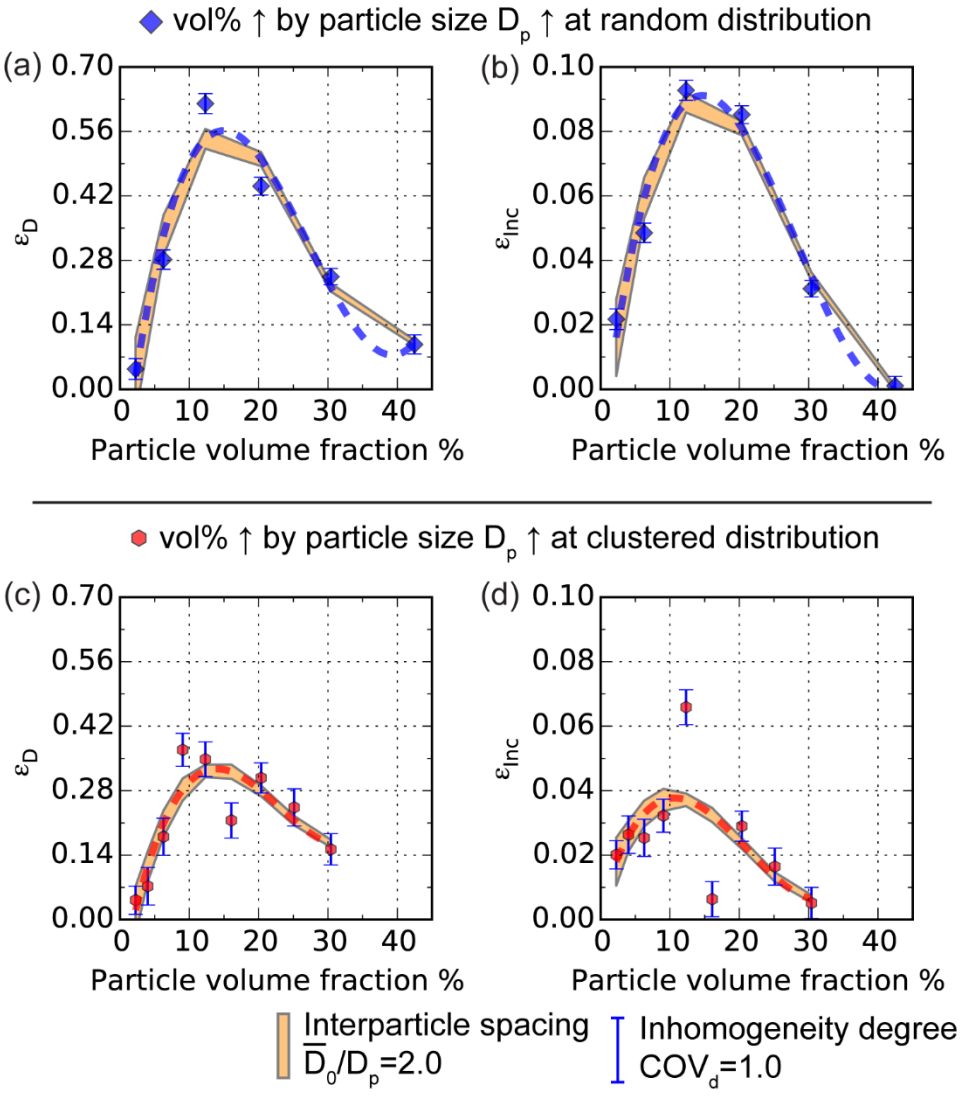

Fig. 6.7. The initial damage strain ε_D and damage incubation strain ε_{Inc} as function of the particle volume fractions. The increase of volume fraction was achieved by increasing particle size D_p: (a, b) at random distribution and (c, d) at clustered distribution.

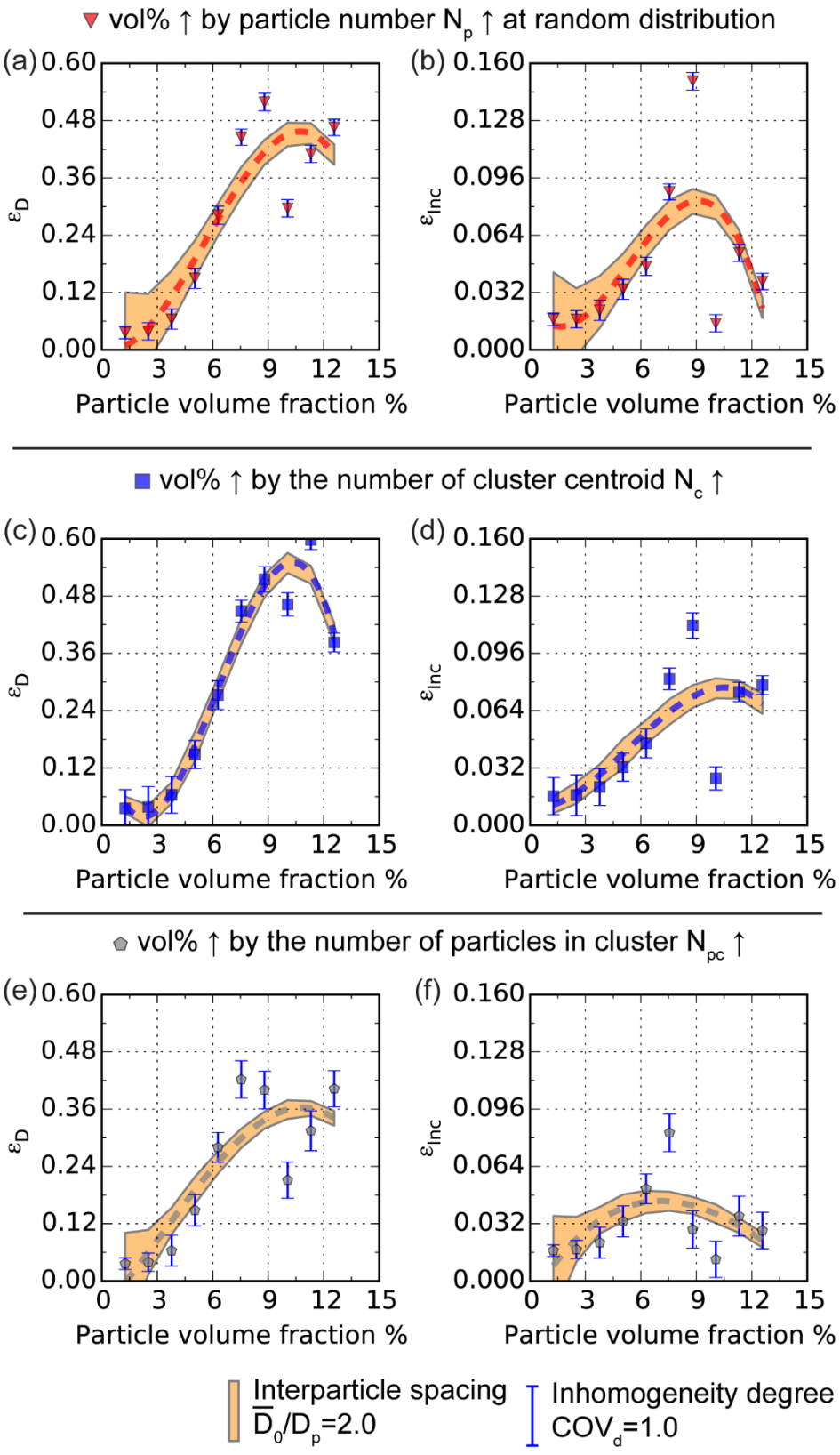

Fig. 6.8. The initial damage strain ε_D and damage incubation strain ε_{Inc} as function of the particle volume fractions. The increase of volume fraction was achieved by adding particles under three different ways: (a, b) by adding particles at random distribution, (c, d) by increasing the number of cluster centroids N_c, and (e, f) by increasing the number of particles about each cluster centroid N_{pc}.

Fig. 6.7 and Fig. 6.8 show the results in terms of the variation of the initial damage strain ε_D and damage incubation strain ε_{Inc} as function of the particle volume fraction vol%. The trend of ε_D (dashed lines) increases from about 0.02 to the peak values (between 0.3 and 0.6 strain values in different cases) as the volume fraction increases from 1.26 (Fig. 6.8a, c, e) or 2.26vol% (Fig. 6.7a and c) to the range of 7~15vol%. After the peak values, the trend of ε_D decreases below 0.2 as the volume fraction increases above 30vol% (Fig. 6.7a and c). Similar trend is also observed for the variation of ε_{Inc}. In addition, the results in Fig. 6.7 and Fig. 6.8 show the peak values of ε_D and ε_{Inc} for the homogeneous distributions (COV_d below 0.4) are about 30% higher than that for the inhomogeneous distributions (COV_d above 0.4), indicating significantly higher performance on particle damage obtained for more homogeneous distributions.

The volume fraction effect on the load transfer from matrix to particle is illustrated in the average von Mises stress versus global von Mises strain curves of the TiB_2 particle, Fe-α matrix and Fe – TiB_2 composite (Fig. 6.9). Fig. 6.9a shows the TiB_2 particles are subjected to decreasing level of the average stress from 5GPa to 1GPa with increasing volume fraction from 2.26vol% to 42.47vol%, especially during the elastic deformation of the composite. For 2.26vol% and 3.77vol%, the average stress level of the TiB_2 reaches above 5GPa at a very early loading stage (global strain less than 3%) followed by the initiation of particle damage. For 42.47vol%, the average stress of the TiB_2 is observed a little higher than that of 30.41vol% (magnified image in Fig. 6.9a). For the stress-strain curves of the matrix (Fig. 6.9b), not much differences are observed between different volume fractions. For the stress-strain curves of the composite (Fig. 6.9c), both strength and modulus increase significantly for the high-volume fractions above 20vol%.

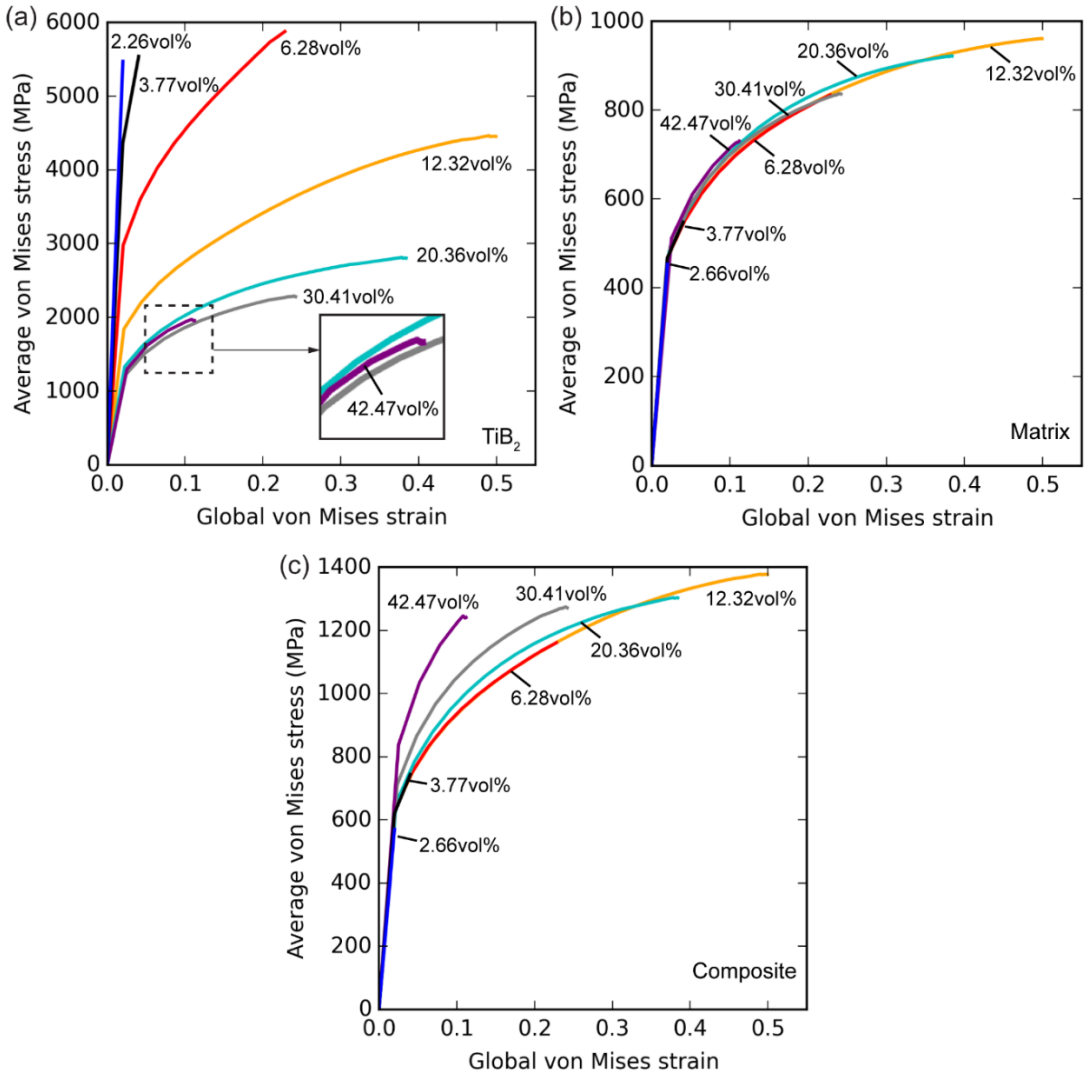

Fig. 6.9. For the composite microstructures with different TiB_2 volume fractions, the average von Mises stress versus Global von Mises strain curves are plotted before initial particle damage for (a) the TiB_2 particles, (b) α-Fe matrix and (c) Fe – TiB_2 composite. The particle distributions of the composite microstructures are homogeneous with COV_d less than 0.4.

6.3 Discussion

For Fe – TiB_2 HMS, one of main challenge for enabling HMS as lightweight materials lies in improving ductility by minimizing particle damage. This can be achieved by tailoring the particle microstructure, such as spatial distributions, size and volume fraction, according to their effects on particle damage. In this study, the simulation results allow to systematically evaluate the effects of different particle parameters in view of their suitability for composite design of high performance on particle damage behaviour. This is shown in Fig. 6.10, where characteristic values which are essential for evaluating particle damage in this study, i.e. the initial damage strain ε_D and the damage incubation strain ε_{Inc}, are summarised. The optimum particle damage behaviour is represented by simultaneously high characteristic values, ε_D and ε_{Inc}. Consequently, areas of ε_D vs ε_{Inc} for diverse groups of particle parameters are indicated in this modified Ashby map. Based on this diagram, the significant effects of these particle parameters will be discussed in the following.

6.3.1 The effect of particle clustering degree

The heterogeneity degree COV_d was used to quantify the clustering degree of the studied particle distributions. Even random distributions contain already several closely packed regions. In clustered distributions, this situation becomes more severe as the average interparticle spacing is significantly decreased (Fig. 6.4). This study covers a broad range of statistically relevant configurations with a total of 22 microstructures, varying the clustering degree COV_d from about 0.26 to 0.94. This allow us to determine critical values for particle clustering. Another important progress of this study lies in the use of advanced constitutive laws which couple crystal plasticity and phase field damage model to simulate co-deformation of heterogeneous composite materials. As illustrated in Fig. 6.10a, the particle distributions with COV_d below 0.4 show optimal performance with high values of initial damage strain ε_D and damage incubation strain ε_{Inc}. However, the distributions with COV_d above 0.7 exhibit much lower values of ε_D and ε_{Inc}, which indicates a significantly increasing preference for particle fracture in

highly clustered microstructure. This corresponds well to the experimental observation in the study by Zhang el al.(Zhang et al., 2016). They showed that particle fracture events were concentrated in regions of high degree clustering, especially in the area close to the material fracture surface. Similar observation was also found in highly clustered areas by Szczepaniak el al.(Szczepaniak et al., 2017). In other systems, such as Al-SiC composites, studies on the effect of particle spatial distribution also revealed that the particle fracture probability significantly increased in very inhomogeneous microstructure both in experiments (Davidson, 1993; Lewandowski et al., 1989; Lloyd, 1991; Williams et al., 2010) and simulations (Ayyar et al., 2008; Segurado et al., 2003; Segurado and Llorca, 2006).

6.3.2 The effect of particle size

From the analysis of simulation results (Fig. 6.5 and Fig. 6.10b), it shows that particle damage is sensitive to different particle size. Our study revealed that particles fractured early and rapidly with large particle size (above 0.06L). This corresponds well to the experimental observations by Hadjem-Hamouche et al.(Hadjem-Hamouche et al., 2012; Hadjem-Hamouche et al., 2018) and Li et al.(Li et al., 2016) which showed that the large primary TiB_2 particles were fractured more frequently than the small eutectic particles. In their studies, the main damage initiation mechanism was dominated by the fracture of the coarse primary particles. This is due to that a larger load transfer from the matrix to the particle for large particles (Chawla and Shen, 2001; Davis et al., 1998; Hall et al., 1994). Similar observations were also found in Al-SiC composites (Chawla and Shen, 2001; Hall et al., 1994; Sun et al., 2011). From the damage pattern comparison between simulation and experiment in our study (Fig. 6.6), the good correspondence of shape and orientation of particle cracks can not only validate our simulation results, but also demonstrate that the clustered large particles tend to result in damage percolation during loading which could induce failure of MMCs. As illustrated in Fig. 6.10b, the intermediate particle size (0.03~0.06L) in our study exhibited relatively good and stable damage performance. The optimal performance is observed at a specific particle diameter D_p of 0.037L. With further decreasing particle

size (below 0.03L), large fluctuation was observed which splits into two sub-areas with different damage performance. This indicates that the small particles are more sensitive to the partitioning of the internal stress and strain field across the matrix. Therefore, corresponding alloy design efforts should be directed towards the intermediate particle size for obtaining stable performance on particle damage behaviour and for avoiding producing any large particles.

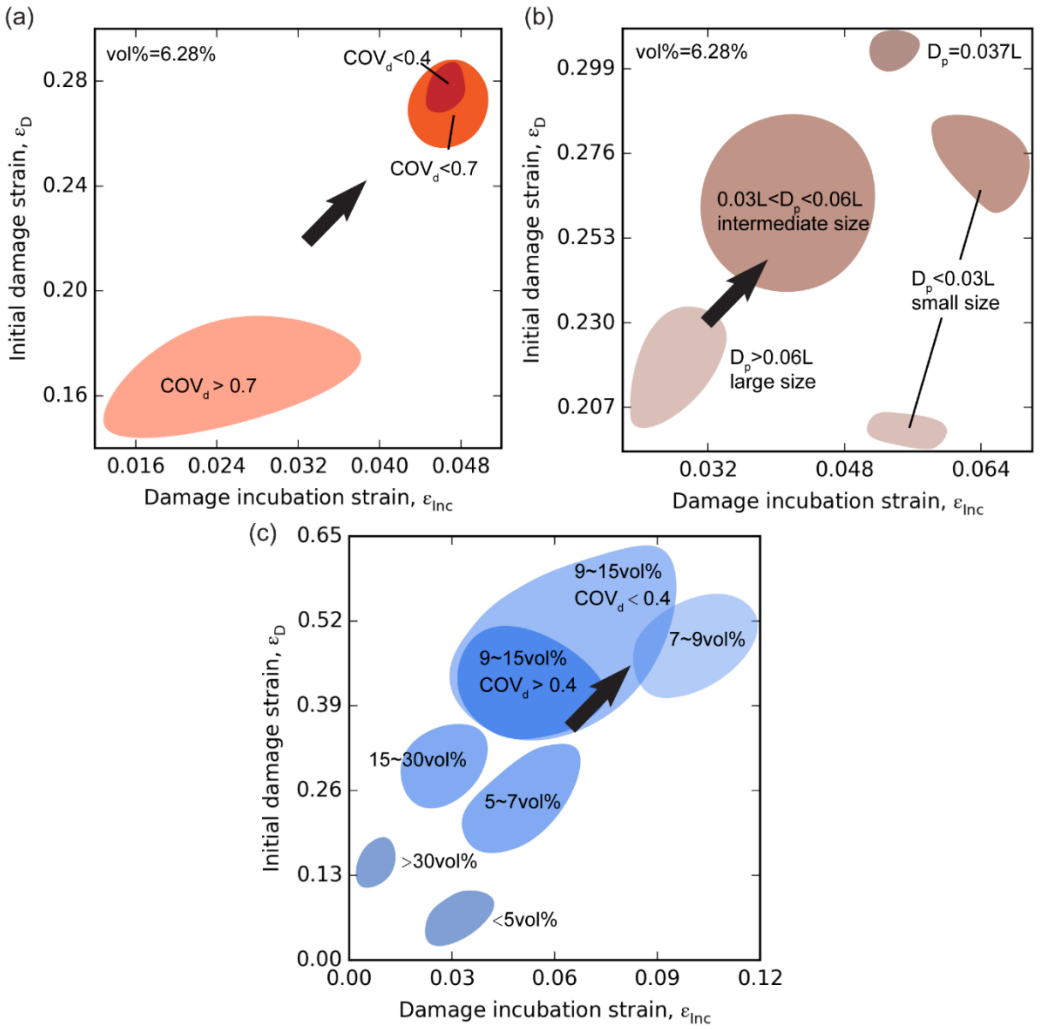

Fig. 6.10. Ashby-type diagrams for the characteristic parameters for evaluating the individual particle damage phenomena and their role for the design of high stiffness composite steels. Here focus is placed on the initial damage strain ε_D vs. damage incubation strain ε_{Inc} for different effects of particle parameters: (a) heterogeneity degree COV_d, (b) particle size D_p, (c) particle volume fraction vol%. The design directions for obtaining high performance on particle damage behavior are indicated by the black arrows. L: the side length of the modelled RVE geometry.

6.3.3 The effect of particle volume fraction

Compared to the effects of particle clustering degree and particle size, the simulation results (Fig. 6.7 and Fig. 6.8) show that the particle volume fraction has the most significant impact on particle damage. As summarized in Fig. 6.10c, it reveals that the optimal performance on particle damage is in the range of 7~15vol% with a homogeneous particle distribution (COV_d below 0.4). The volume fractions of Fe-TiB_2 MMCs fabricated by liquid metallurgy synthesis in previous studies were typically in the range of 10~20vol% (Baron et al., 2016; Hadjem-Hamouche et al., 2012; Hadjem-Hamouche et al., 2018; Springer et al., 2015; Zhang et al., 2016). It was reported (Baron et al., 2016) from the experimental tensile testing that the Fe-TiB_2 composites with 10vol% TiB_2 exhibits higher ductility with 48% tensile elongation (TE) than the composites with 20vol% TiB_2 which shows only 15% TE. Our study corresponds to this result as shown in Fig. 6.7 and Fig. 6.9c. For higher particle volume fractions, our study showed the composite exhibits very poor damage performance. In experiment, Tanaka and Saito (1999) reported that they fabricated Fe-TiB_2 composites – but via powder metallurgy synthesis – by incorporating about 30vol% TiB_2 in an Fe-Cr alloy, however such composites are often brittle and exhibit relatively poor fracture properties (Lewandowski, 2000). For low volume fraction (<5vol%), little attention was paid by research and engineering because such small reinforcement volume cannot achieve significant improvement of physical and mechanical properties.

6.3.4 The effect of particle interface

The interface between TiB_2 particle and iron matrix plays a key role to achieve significant composite effect on strengthening and good enough ductility during deformation. This is because the interface is responsible for carrying the load between the matrix to the particles (Chawla and Shen, 2001). According to previous experimental investigations, good interfacial coherency and high interfacial strength were found (Cha et al., 2012; Huang et al., 2015; Lartigue-Korinek et al., 2015; Li and Huang, 2017) for Fe-TiB_2 MMCs fabricated by eutectic solidification. In addition, the

recent studies (Dammak et al., 2014; Dammak et al., 2013; Hadjem-Hamouche et al., 2012; Hadjem-Hamouche et al., 2018; Li et al., 2016) on the deformation behaviour and damage evolution of Fe-TiB_2 MMCs showed that particle fracture is the dominating damage mechanisms and the main reason for damage failure of the composite at room temperature, whereas particle interface debonding is rarely and much less frequently observed. Therefore, the effect of interface decohesion on the damage behaviour of Fe-TiB_2 MMCs is negligible. Because of this reason, we regard good interfacial bonding of Fe-TiB_2 interface as assumption and did not introduce the mechanism of interfacial decohesion in the study. As a result, the particle fracture is the major damage mechanism in our study which corresponds well to the experimental observations in Fe-TiB_2 composites (as shown in Fig. 6.6).

6.3.5 The effect of composite strengthening

In our study, the direct strengthening resulted from the load transfer from matrix to particle is obvious. As shown in Fig. 6.2, the average stress of the TiB_2 particles is about one order of magnitude higher than that of the matrix. For the volume fraction effect, as illustrated in Fig. 6.9c, the strengthening increases with volume fractions. This is mainly due to more load transfer from matrix to particles as particle volume increases. Meanwhile, the average stress of the matrix did not change much (Fig. 6.9b). Such strengthening effect corresponds well to the previous studies (Davis et al., 1998; Yang et al., 1991). However, although the strength of the composites can be improved greatly by increasing particle volume fraction, the ductility could be reduced significantly by the early onset of particle fracture (Fig. 6.7 and Fig. 6.9c) as the poor damage performance for high volume fractions (>30vol%).

6.4 Conclusions

The aim of this study is to derive the optimal particle configuration guidelines for the production of Fe – TiB_2 HMS an optimized property profile, namely to maximize the composites ductility by tailoring the particle microstructure to minimize damage under loading. the effects of different particle parameters were systematically investigated, such as spatial distributions, size and volume fraction, on particle damage initiation by conducting tensile loading in crystal plasticity Fast Fourier transformation simulation coupled with phase field damage model, deriving the variation of initial particle damage behaviour as function of different microstructural parameters. From the obtained results, the following conclusions can be drawn:

(1) By using the spectral method, the computational efficiency of heterogeneous material can be greatly improved. The recent improvement of the computational efficiency of the spectral solver as coded in DAMASK make it particularly suited for MMC materials with large local stiffness contrast among the adjacent phases. Incorporating the advanced constitutive laws which couple crystal plasticity and phase filed method to simulate co-deformation of heterogeneous composite materials, this simulation method in our study can open pathways to the ICME approach with high-throughput simulations, which can further significantly speed up the material design process of the novel heterogeneous material with superior properties.

(2) For the effect of particle clustering, the simulation results revealed a significantly increasing preference for early and rapid particle fracture in highly clustered microstructures, especially for COV_d values above 0.7. In homogeneous distributions (COV_d below 0.4), the simulation results showed a significantly high performance on particle damage.

(3) For the effect of particle size, the simulation results revealed that particles fractured early and rapidly with large particle size (above 0.06L). Composites with intermediate particle size (0.03~0.06L) showed relatively good and stable damage performance. The optimal performance was observed at a specific particle diameter

D_p of 0.037L. Composites with small particle size (below 0.03L) exhibited large fluctuation of damage behaviour.

(4) For the effect of particle volume fraction, the simulation results revealed that the particle volume fraction has the most significant impact on particle damage, comparing to the particle clustering and particle size. Our study showed the optimal damage performance is in the range of 7~15vol% with a homogeneous particle distribution (COV_d below 0.4). Very poor damage performance was found for high volume fractions (> 30vol%) and very low volume fractions (< 5vol%). The particle volume fraction also has strong influence on composite strengthening. Due to the load transfer from matrix to particles, our study showed significant strengthening occurs for volume fraction higher than 30vol%. However, the ductility could be reduced greatly due to very poor damage performance in such high volume fraction composites.

(5) From the analysis of simulation results, the above guidelines correspond well to the observations from previous experimental studies. Therefore, more pathways could be opened and further novel design of Fe-TiB_2 composites can be conducted based on these findings. In summary, the Fe - TiB_2 MMCs microstructures containing more homogeneous particle distribution (COV_d below 0.4) with 7~15vol% TiB_2 and avoiding large primary TiB_2 particles, are most favorable for obtaining HMS with superior ductility.

7 The formation of laminate deformation patterning in nickel single crystal[1]

This chapter is the results for the second study subject of this thesis. The study was focused on investigating the reasons for severe deformation patterning observed in crystal plasticity simulations. The plane strain compression loading was loaded on an f.c.c nickel single crystal with initial near-Copper orientation. The results showed that the microstructure lamination is the result of a complex interplay between available deformation systems, strain hardening, kinematics, and deformation energetics. During strain hardening, the strong collinear interaction strength causes—depending on the initial deviation from the nominal orientation—the selection of a single prevalent slip system in clearly delimited regions. This behaviour is explained by the lower global deformation energy in comparison to a homogeneous double slip behaviour. It was also revealed that only interaction strength values in the range predicted by discrete dislocation dynamic simulations result in deformation bands.

7.1 Investigation of deformation bands formation

7.1.1 Slip system geometry and Schmid factor

Out of the twelve slip systems, the two systems termed A6 and D6 according to Schmid and Boas (1968) have the highest resolved shears stress, i.e. Schmid factor (Table 7.1-1). The geometry of the two prevalent slip systems is illustrated in Fig. 7.1 from which the alignment of the common slip direction of A6 and D6 with ND can clearly be seen. Due to the initial orientation scatter (Raabe and Roters, 2004; Raabe et

1 The results of this study are published by Wang et al.(2018a).

al., 2004), minor fluctuations of the Schmid factor exist already at the beginning of the simulation. As shown for two selected points (termed "A" and "B") in Table 7.1-1, these fluctuations will introduce a certain sequence at each point between these two kinematically preferred systems. However, due the large difference to the slip systems with the second highest Schmid factor, no other slip system will become the easiest one to shear.

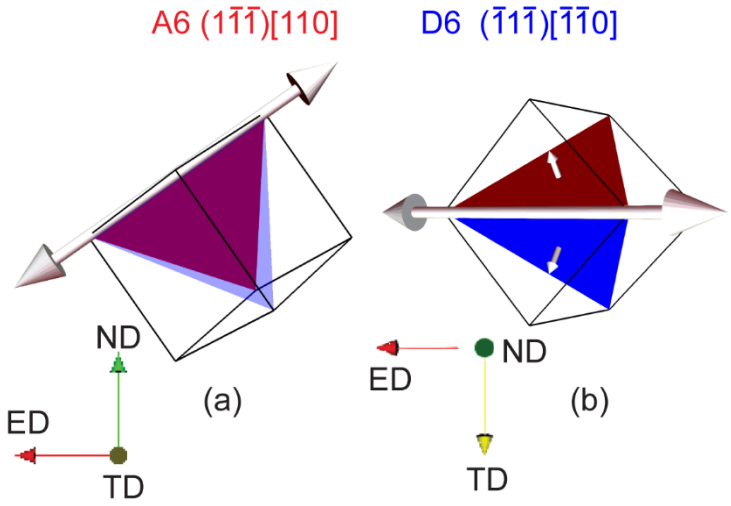

Fig. 7.1. Unit cell outline with slip system geometries of collinear systems A6 (slip plane in red). And D6 (slip plane in blue) systems in Copper orientation $(\mathbf{112})[\mathbf{11\bar{1}}]$. The large arrow depicts the common slip direction, the small arrows depict the slip plane normal. (a) shows the front view parallel to the ED-ND plane and (b) shows the top view parallel to the ED-TD plane.

7.1.2 Deformation bands patterning

At the final load of 5.5% applied strain, pronounced deformation bands (DBs) in the form of a laminate structure have evolved as shown in Fig. 7.2a in terms of the equivalent strain and in Fig. 7.2b and Fig. 7.2c in terms of the accumulated shear on the dominant slip systems A6 and D6. Comparing Fig. 7.2a with Fig. 7.2b reveals that the highly strained regions correspond to regions alternately dominated by shear on either A6/D6 slip systems while the low strained regions are found in the transition regions between them. From the three-dimensional view in Fig. 7.2b and c, in which only regions with high accumulated shear on A6/D6 systems are shown, the shape of the DBs becomes visible: The laminate structure of DBs exists throughout the volume and

the lamellar DBs visible on the front do not traverse along TD, but distribute in flat layers perpendicular to TD. On each layer, the lamellar DBs are inclined with respect to ED/ND at a very similar angle.

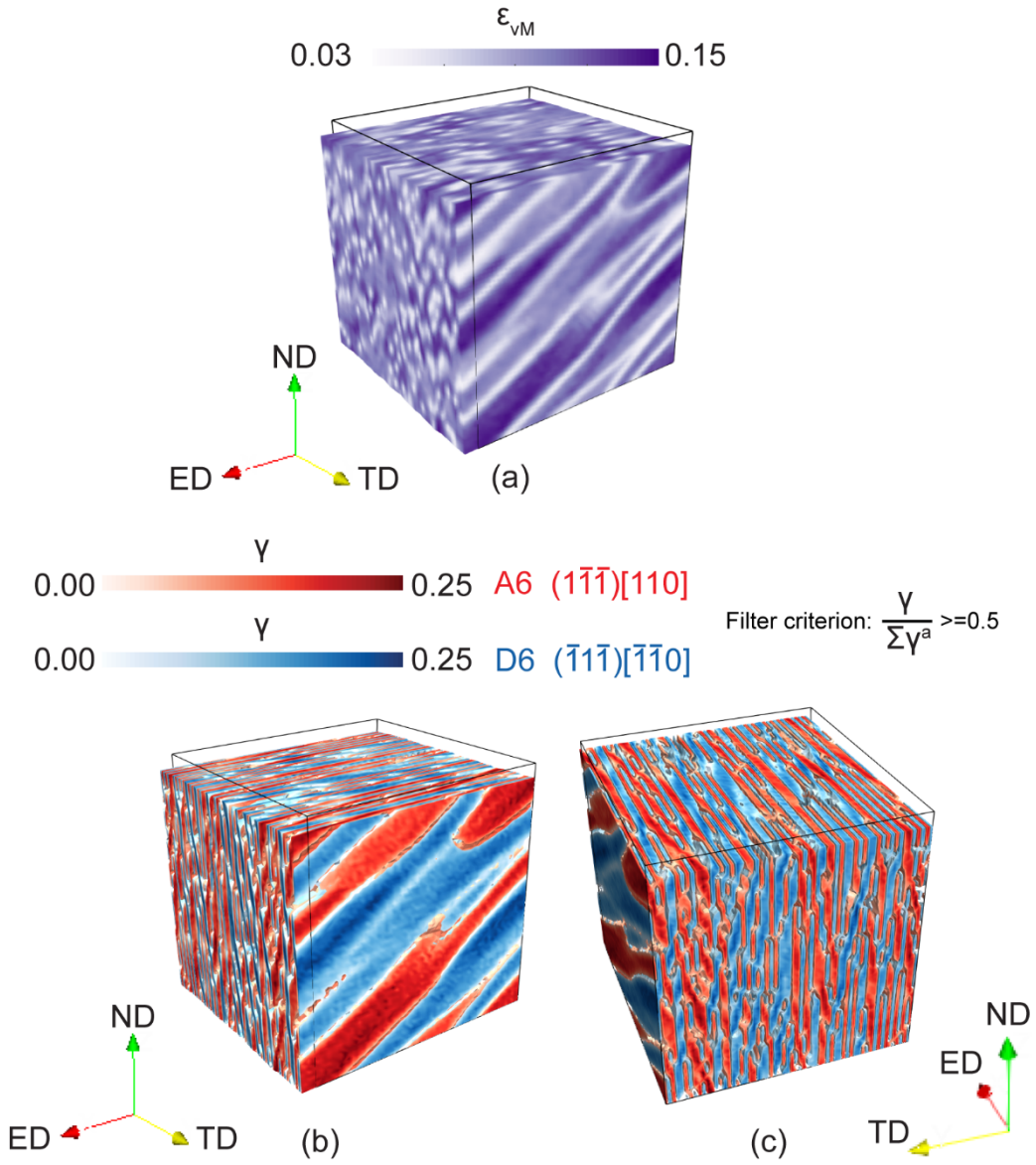

Fig. 7.2. The deformation bands pattern: (a) Distributions of von Mises strain showing deformation bands patterning at final deformation of 5.5% strain in loading direction (-ND). (b, c) Different views of filtered distribution of accumulated shear on A6 and D6 slip systems showing the inner structure of the deformation bands. Regions are selected if one of the considered slip systems contributes with more than 50% to the total shear: $\frac{\gamma}{\Sigma\gamma^{\alpha}} \geq \mathbf{0.5}$. For simulating plane strain deformation, the space coordinates are set as elongation direction (ED), transverse direction (TD) and normal direction (ND) respectively.

Table 7.1-1: Schmid factors under plane strain compression for the octahedral slip systems of the f.c.c lattice. The ideal Copper orientation is compared to the perturbed orientations found on two grid positions (Point A and B). The Schmid factor is calculated as $\boldsymbol{m^{\alpha}} = |\frac{\boldsymbol{\sigma}}{\|\boldsymbol{\sigma}\|} : (\boldsymbol{s^{\alpha}} \otimes \boldsymbol{n^{\alpha}})|$ where here $\boldsymbol{\sigma}$ is the stress tensor for an ideal plane strain compression, i.e. σ_{zz}=-1, σ_{yy}=-0.3, σ_{xz}=σ_{zx}=0.1 and zero otherwise. $\boldsymbol{s^{\alpha}}$ and $\boldsymbol{n^{\alpha}}$ are the slip direction and slip plane normal of slip system $\boldsymbol{\alpha}$. The systems with the highest Schmid factor are given in bold font. The notation follows Schmid and Boas (Schmid and Boas, 1968).

Slip System label	**Slip plane n^{α}**	**Slip direction m^{α}**	**Copper-orientation (90°,35°,45°) (112)[11$\bar{1}$]**	**Point A: (92.7°, 36.9°, 43.8°) Initial A6**	**Point B: (87.8°,34.1°,46.8°) Initial D6**
A2	$(1\bar{1}\bar{1})$	$[0\bar{1}1]$	0.0342	0.0527	0.0249
A3	$(1\bar{1}\bar{1})$	$[\bar{1}0\bar{1}]$	0.2340	0.2263	0.2339
A6	$(1\bar{1}\bar{1})$	$[110]$	**0.2682**	**0.2790**	0.2588
B2	(111)	$[01\bar{1}]$	0.1906	0.1621	0.2080
B4	(111)	$[\bar{1}01]$	0.1906	0.1705	0.1965
B5	(111)	$[1\bar{1}0]$	0.0000	0.0084	0.0116
C1	$(\bar{1}\bar{1}1)$	$[0\bar{1}\bar{1}]$	0.0776	0.1085	0.0623
C3	$(\bar{1}\bar{1}1)$	$[101]$	0.0776	0.0986	0.0673
C5	$(\bar{1}\bar{1}1)$	$[\bar{1}10]$	0.0000	0.0100	0.0050
D1	$(\bar{1}1\bar{1})$	$[011]$	0.2340	0.2179	0.2455
D4	$(\bar{1}1\bar{1})$	$[10\bar{1}]$	0.0342	0.0427	0.0299
D6	$(\bar{1}1\bar{1})$	$[\bar{1}\bar{1}0]$	**0.2682**	0.2606	**0.2753**

An ED/ND section is shown in Fig. 7.3 to investigate the pattern in more details. Plots of both local strain (along the direction shown in Fig. 7.3b) and the accumulated shear of different slip systems are shown in Fig. 7.3d and e. It is confirmed that the deformation plateaus are alternately dominated by A6/D6 slip systems while the accumulated shear on other systems is significantly lower and the minor contributions result mainly from the B2/B4 systems. On the contrary, the transition zones between the DBs possess much lower activity of A6/D6 systems.

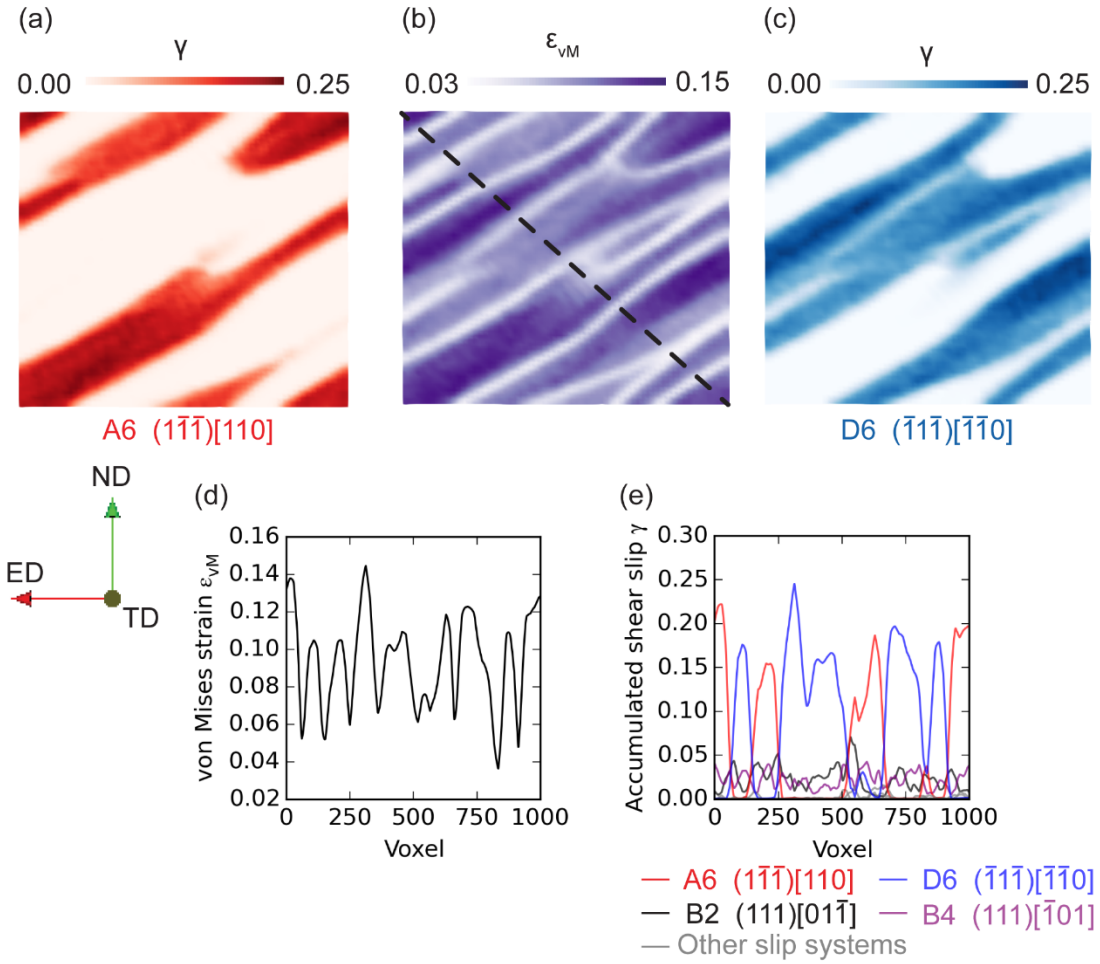

Fig. 7.3. The patterning on the front ED-ND plane of the deformed crystal at 5.5% applied strain: (a) accumulated shear on the A6 slip system (Table 7.1-1;$(\mathbf{1\bar{1}\bar{1}})[\mathbf{110}]$); (b) local von Mises true strain; (c) accumulated shear on the D6 slip system (Table 7.1-1;$(\mathbf{\bar{1}11})[\mathbf{\bar{1}\bar{1}0}]$). Local profiles were plotted along the diagonal line in subfigure (b): (d) local von Mises true strain profile and (e) local accumulated shear profiles revealing the contributions of the different slip systems.

7.1.3 The formation and evolution process of deformation bands

In the following, the temporal evolution of the DBs is investigated. The local equivalent strain, given at increasing load levels in Fig. 7.4a, shows that the DBs form already at a very early deformation stage, i.e. <0.5% global strain. The inclination of the DBs in the initial deformation stage (e.g. at 0.5% global strain) is almost perfectly aligned with the slip trace of the A6/D6 systems on the front ED-ND plane (Fig. 7.1a). The microstructure laminates, once formed, remain very stable and self-similar at increasing intensity during the later loading stage.

To investigate kinematic aspects of the DB formation process, the *local Taylor factor*

(Raabe et al., 2001; Zhao et al., 2008) is considered. In geometric terms, that is without regarding strain hardening details, the Taylor factor quantifies the total amount of the crystallographic shear that is required for a deformation step to match a certain strain boundary condition. Thus, the *local Taylor factor* is defined as $M^{\mathrm{local}} = \sum \gamma^{\mathrm{local}} / \varepsilon_{\mathrm{p}}{}^{\mathrm{local}}$, where γ^{local} is the accumulated *local* crystal shear, and $\varepsilon_{\mathrm{p}}{}^{\mathrm{local}}$ is the plastic portion of the *local* von Mises strain [47]. According to this definition, a higher Taylor factor is typically associated with a higher kinematic hardness of a crystal region (Raabe et al., 2003; Sachtleber et al., 2002). Thus, the local strain hardening during the lamination process can be seen in the *local Taylor factor* pattern plots at different global strains as given in Fig. 7.4b. The rapid partitioning of the local Taylor factor pattern from initially random distribution into banded regions agrees with the evolution of the von Mises true strain shown in Fig. 7.4a. Lower Taylor factor values are mainly observed inside DBs, whereas interfacial regions showing higher values.

Finally, Fig. 7.4c presents the evolution of the accumulated shear, where the A6 system is exemplarily shown and D6 is omitted since it has a similar evolution process. After the initial stage of the plastic deformation, the DBs dominated by the A6 system develop from a random pattern caused by the initial orientation scatter into a distinct banding pattern. The shear patterning at 0.1% strain, leftmost image in Fig. 7.4c, shows that not all points inside regions that are later dominated by shear on the A6 system have an initial orientation preferentially aligned for this system. During ongoing deformation, the slip activities of these points change under the influence of the stress imposed by the neighboring material. To investigate this local slip evolution process, two typical points termed “A” and “B” inside a A6 dominated band are selected. Point A, in contrast to point B, shows initially high slip rates on the A6 system. The shear rate evolution of these two points during the initial deformation stage is shown in Fig. 7.5. For point A (Fig. 7.5a), the initial activated A6 slip system corresponds to the largest Schmid factor (Table 7.1-1) and this dominance is maintained, even after the activation of a secondary slip system (B2) during the early deformation stage. By comparison, point B (Fig. 7.5b) shows a different slip behaviour at the onset of plastic deformation.

The shear rate profile reveals that the initial slip occurs on the D6 system, which also corresponds to the largest Schmid factor (Table 7.1-1). However, the slip activity of system A6 increases quickly afterwards. Already at 0.1% strain, the shear rate on system D6 is completely vanished and shear on the A6 system becomes the dominating deformation mode.

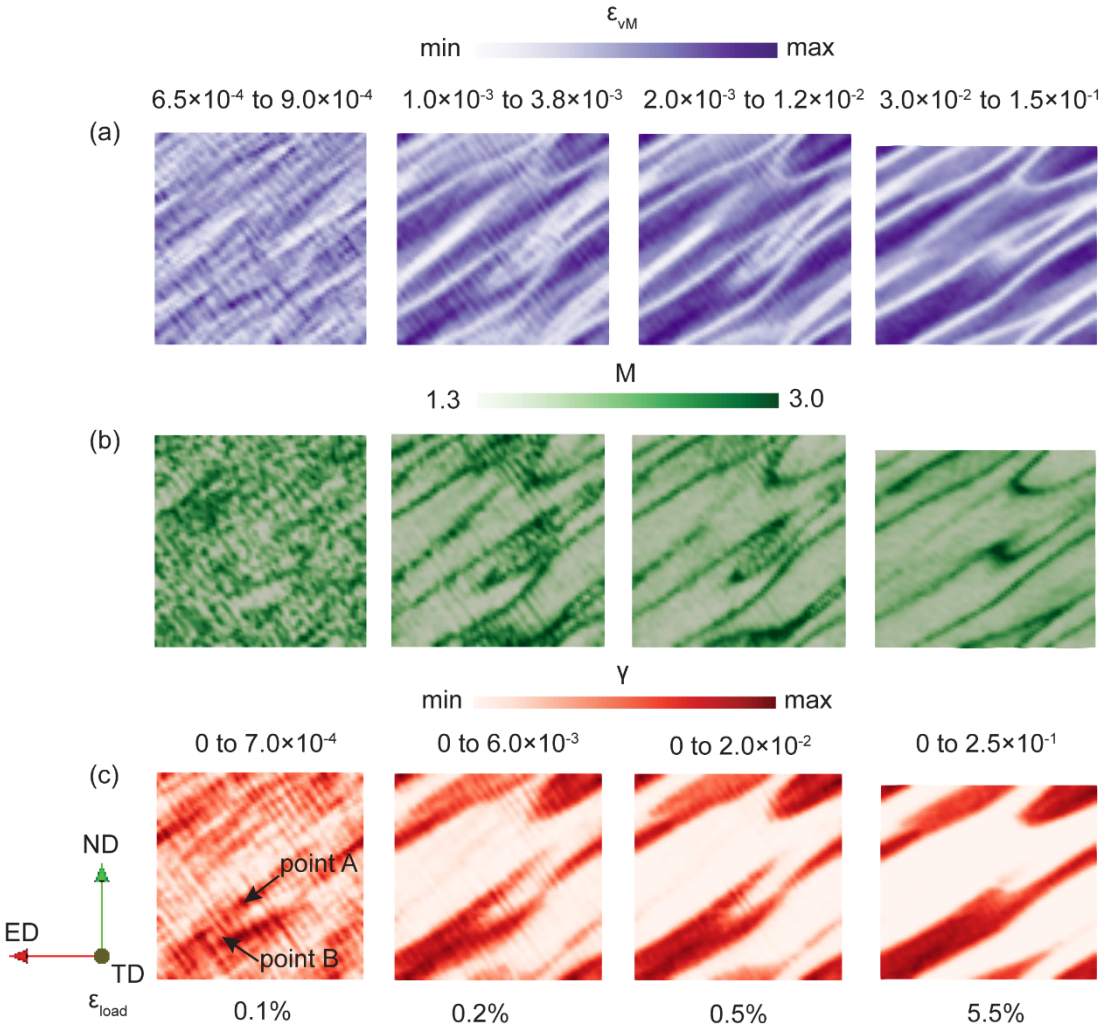

Fig. 7.4. Patterning evolution of (a) local von Mises true strain; (b) local Taylor factor M; (c) accumulated shear on slip system A6 (Table 7.1-1;$(1\bar{1}\bar{1})[110]$) on the ED-ND plane at different applied strains in loading direction: 0.1%, 0.2%, 0.5%, 5.5%.

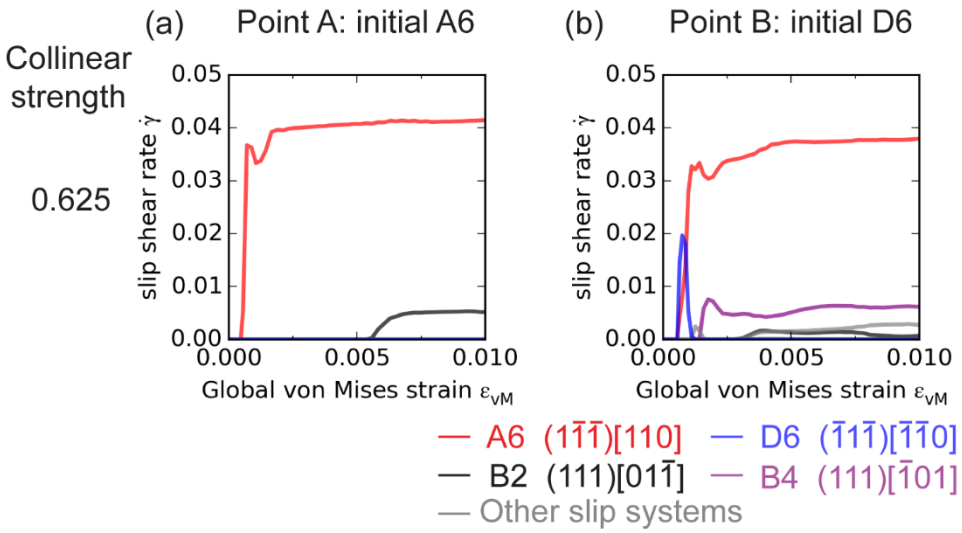

Fig. 7.5. Instantaneous shear rate as a function of global von Mises true strain for (a) point A and (b) point B in the simulations using default collinear strength $\boldsymbol{h_{coll} = 0.625}$ (Table 5.2-1). The locations of point A and B are indicated in Fig. 7.4c.

7.1.4 The influence of collinear dislocation interaction on slip activity

The results presented above reveal that the formation process of the DBs is a result of slip on the collinear A6/D6 slip systems. The DB formation can be understood as an energy minimization process by which the energetically more expensive homogeneous double slip mode is impeded. For the selected Copper orientation, this energy gain is especially large as the collinear interaction strength (h_{coll}) is the largest among all interactions between different slip systems (0.625 in Table 5.2-1) (Kubin et al., 2008). To investigate the influence of the value of the interaction parameter, additional simulations with lower ($h_{coll} = 0.122$, similar to the other interaction types) and higher ($h_{coll} = 3.0$, more than one order of magnitude higher than other types) collinear interaction coefficients were conducted.

The results show that neither of these two coefficients results in distinct DB formation (slip pattern on A6 system in Fig. 7.6). For a low collinear interaction value, $h_{coll} = 0.122$, almost no patterns emerge. The initial slip pattern (at 0.1% global strain, Fig. 7.6a) is similar to the one found for the default interaction parameter value (at 0.1% global strain, Fig. 7.4c), but the slip pattern becomes more and more homogeneous with ongoing deformation (at 5.5% global strain in loading direction, Fig. 7.6a). For the case of high collinear interaction value, $h_{coll} = 3.0$, the slip pattern starts later than for the

default value, i.e. at 0.2% global strain (Fig. 7.6b), and no coarse DBs (at 5.5% global strain, Fig. 7.6b) form. The narrow spaced features formed additionally in this case are aligned in the direction perpendicular to the coarse DB patterns. This kind of pattern is also observed at the initial deformation stage when using the default interaction strength ($h_{coll} = 0.625$, at 0.1% and 0.2% global strain in Fig. 7.4c), but it disappears and develops into DB patterns during the later deformation stages.

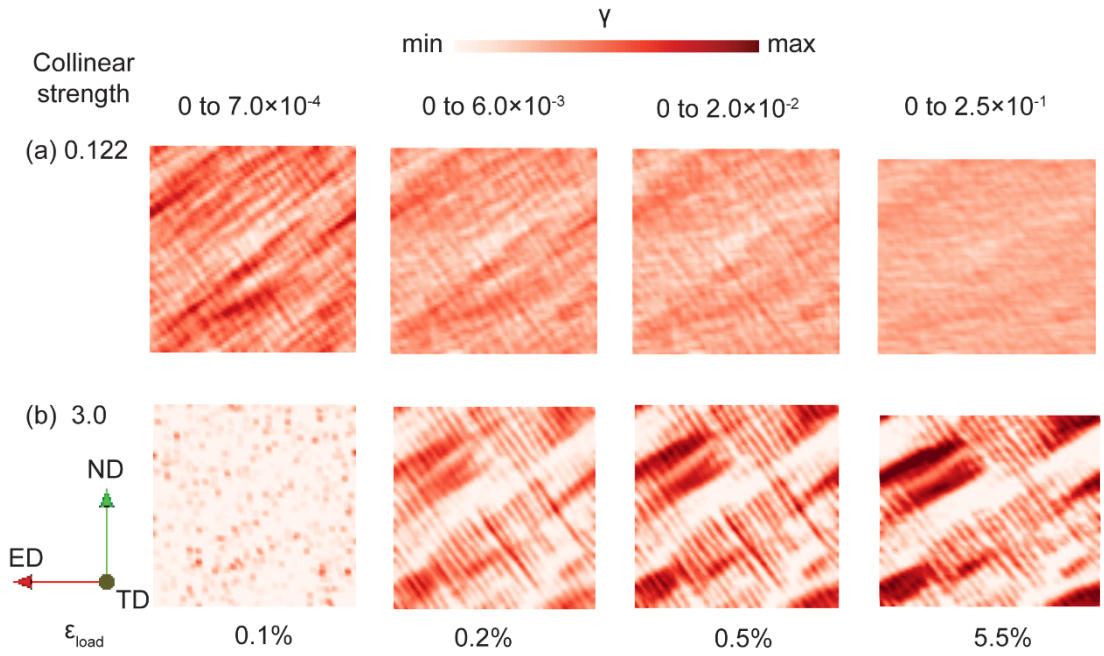

Fig. 7.6. The patterning evolution of accumulated shear on slip system A6 (Table 7.1-1;$(1\bar{1}\bar{1})[110]$) on the ED-ND plane of the deformed crystal with different $\boldsymbol{h_{coll}}$: (a) "low" 0.122 and (b) "high" 3.0). The patterning is shown at different applied strains in loading direction: 0.1%, 0.2%, 0.5%, 5.5%.

Similarly to the results shown in Fig. 7.5, the temporal evolution of the shear rates for the selected points A and B is shown in Fig. 7.7 for the modified interactions parameters. In the case of a low collinear interaction value $h_{coll} = 0.122$ (Fig. 7.7a and b), the initially favored slip system remains dominant but the second collinear system becomes also active. Also note that the sum of the rates on both systems for $h_{coll} = 0.122$ at 0.01% global strain is similar to the value for the dominating system (compare Fig. 7.5a and b with Fig. 7.7a and b). For $h_{coll} = 3.0$ (Fig. 7.7c, d), a different behaviour is observed. Both points deform almost exclusively by shear on the system with the highest Schmid factor. While for point A this is the same behaviour as for the reference situation, comparing Fig. 7.5b with Fig. 7.7d reveals significant differences.

No change from D6 to A6 is observed, but significant contributions from B2 and B4 are seen.

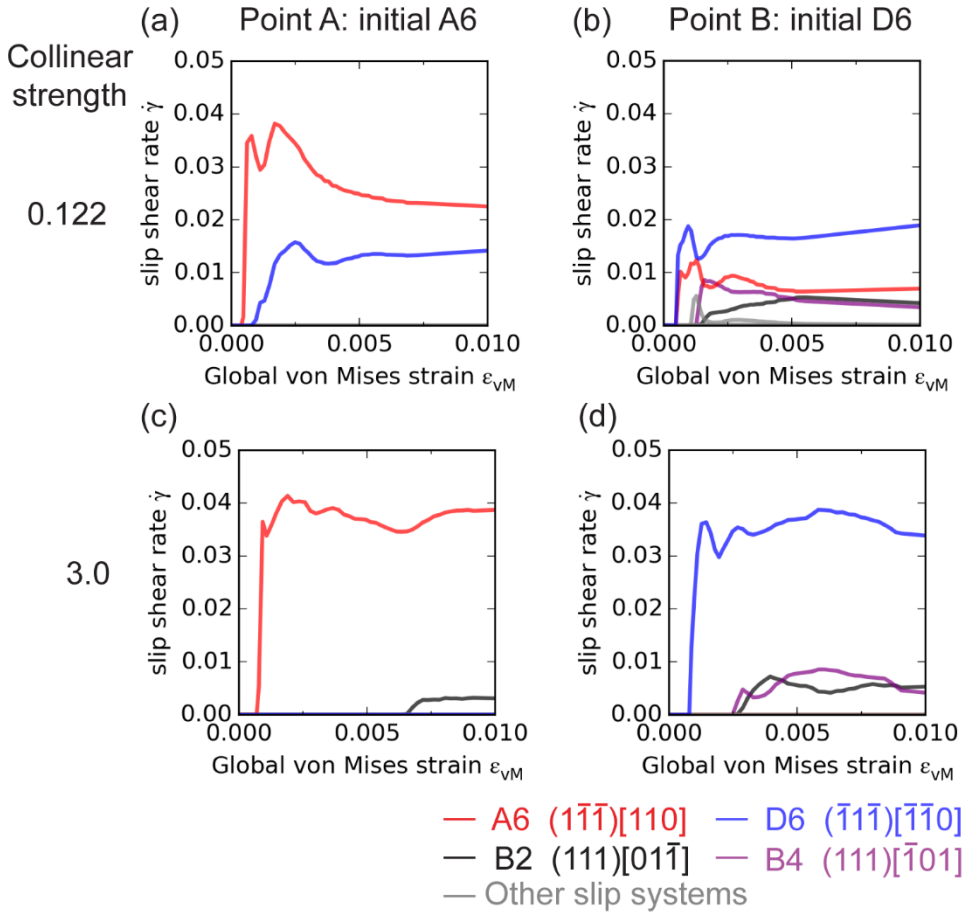

Fig. 7.7. Instantaneous shear rate as a function of global von Mises true strain for point A and B in the simulations using different $\boldsymbol{h_{coll}}$: (a, b) "low" 0.122 and (c, d) "high" 3.0. The locations of point A and B are indicated in Fig. 7.4c.

To compare the global deformation energetics with different h_{coll}, the global stress and strain curves of the different simulations, are shown in Fig.7.8. For $h_{coll} = 0.122$, the curve is initially slightly below the one of the reference solution but increases quickly and crosses it around 2% strain. This indicates that with ongoing deformation, the homogeneous deformation becomes—despite the low interaction strength—energetically more expensive than for the case of inhomogeneous DBs patterning with expensive cross hardening only in the transition zones. The curve for $h_{coll} = 3.0$, i.e. the case of interrupted DBs, is consistently higher. One additional simulation was conducted in which a single point volume element with perfect copper orientation and

default h_{coll} has been subjected to the same load case. This situation promotes the activation of all four slip systems as no pattern can develop. The obtained stress-strain curve is even higher than the one of the full-field simulation with high interaction strength.

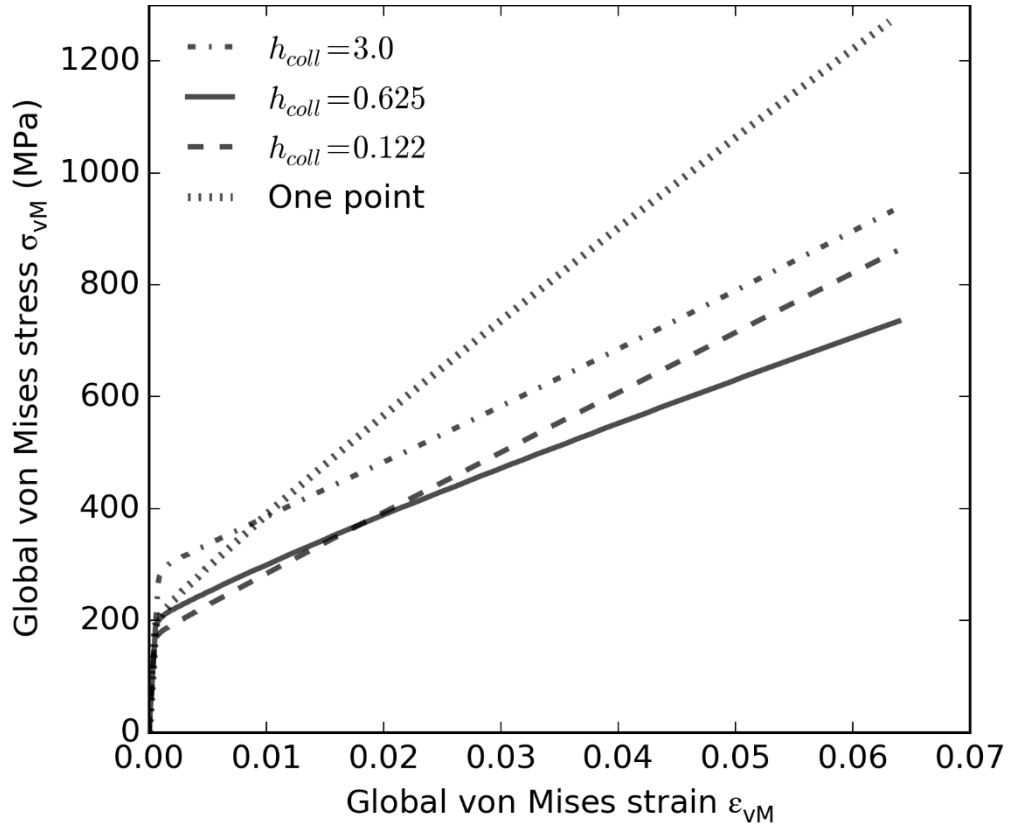

Fig.7.8. The global von Mises stress and strain curves of simulations with different $\boldsymbol{h_{coll}}$. The comparison was also made to a reference simulation with only one single integration point in which no laminate DBs are possible.

7.2 Discussion

The observed laminate DBs formation can be attributed to the minimization of stored energy, which is in agreement with various theories applicable to similar setups (Lee and Duggan, 1993; Lee et al., 1993; Ortiz and Repetto, 1999; Ortiz et al., 2000). In general, the considered single crystal can deform in two ways to comply with the applied boundary conditions. The first type of solution is the spatially homogeneous activation of the same slip systems everywhere such that the imposed global boundary conditions would be fulfilled both, globally and locally. In this case, enforced by using a one-point model (Fig.7.8), the total deformation energy depends on self-hardening as well as on latent hardening parameters of the crystal plasticity models. The second solution is a spatially heterogeneous deformation, i.e. patterning. This split into regions of single slip is—despite the formation of expensive interface transition zones—energetically more favorable in the overall crystal as it reduces energetically expensive collinear hardening in large parts of the crystal. The (lack of) DB formation for the different considered situations can be explained by the dynamic interplay of crystallographic orientation, boundary conditions, and constitutive model as discussed in the following.

7.2.1 Influence of the crystallographic orientation

In the highly symmetric copper orientation, four slip systems have the same highest Schmid factor under the applied load. For the considered single crystal with a texture that deviates by 6° half-width around this orientation, a random activation sequence is introduced among these systems at each point. As the formation of DBs requires one slip system to become dominant in regions comprising several integration points, locally varying stress fields or crystal re-orientation is a requirement for this process. Therefore, a small orientation fluctuation on the one hand is required to initiate the activation of different slip systems, but on the other hand, for a higher scatter the change of the active slip system will become infeasible. Control simulations have shown a lower bound of 1° and an upper bound of 5° scatter to initiate banding for the considered

setup.

7.2.2 Influence of the boundary conditions

The considered generalized plane strain compression boundary conditions exert a strong constraint of deformation along the transverse direction. This constraint prohibits the activation of the B2 and B4 systems (with shear components in TD as shown in Fig. 7.1d) and promotes activation of the A6 and D6 systems due to their slip direction being parallel to the extension direction (Fig. 7.1a and b). Shear along this slip direction thus results in no deformation along TD which matches the imposed boundary conditions. A simulation with uniaxial compression boundary condition (not shown in detail here) shows no patterning and, hence, supports this interpretation.

7.2.3 Influence of the dislocation cross-hardening behaviour

As shown by the parameter variation of the collinear interaction coefficient, its value is decisive for the formation of DBs. For this study, the interaction coefficients for the dislocation interactions in the current F.C.C crystals had been taken from the work of Kubin et al. (Kubin et al., 2008) for the default case (Table 5.2-1). According to the discrete dislocation dynamic (DDD) simulations conducted by Kubin et al., the strength of the collinear interaction h_{coll} is the strongest of all reactions, which was noticed and investigated also in another study (Madec et al., 2003). The simultaneous activation of collinear systems results therefore in strong hardening and is, hence, energetically especially unfavorable. As characterized by the local Taylor factor evolution, the DBs are regions with a low Taylor factor, i.e. they are comparably soft. In other words, the DB mainly deform by shear on one slip system and show only the unavoidable self-hardening (Kuhlmann-Wilsdorf, 1999a). If h_{coll} is smaller than a critical value, there is no significant extra energetic contribution required for the simultaneous activation of the collinear A6/D6 slip systems and the overall deformation becomes homogeneous. If h_{coll} is higher than a critical value, even the double slip required initially to form distinct regions of dominating slip systems out of the random orientation field becomes prohibitive. Therefore, the initial pattern, characterized by two modes intersecting at

90°, persists even though it is associated with a high interfacial energy. Both effects limit the value of h_{coll} to a narrow range that includes the physically sensible value of 0.625. The overall findings of this study are in agreement with a recent study on the influence of the collinear interaction on laminate formation in f.c.c single crystals (Dequiedt et al., 2015). Considering pure plane wave solutions, Dequiedt et al. also found that a laminate microstructure is formed in the early stages of the deformation. Restriction to such idealized pattern, moreover, allows to provide a theoretical justification of the numerical results in the form of instability modes of the homogeneous solution which is hardly feasible for the complex pattern forming in the present study.

7.2.4 Influence of deformation dynamics

While the above presented aspects consider mainly the equilibrium situation, the use of full field simulations as presented here allows deeper insights into the dynamics of the system evolution which are usually not accessible to near equilibrium models. More specifically, the almost homogeneous solution in the case of a small interaction coefficient is not energetically favorable at higher strains as the stored energy is higher than that of the patterning solution in the case of the default interaction parameter setup. Obviously, there is no spontaneous, i.e. energy-minimizing deformation path from the initially favorable homogeneous multi-slip situation to a preferred hypothetical patterning solution. In other words, the system is trapped in a local minima.

7.3 Conclusions

Full-field crystal plasticity simulations have been conducted to investigate self-organisation of a single crystal into complex microstructure laminates in a nickel single crystal with initial near-Copper orientation (3° initial orientation scatter around $(112)[11\bar{1}]$) under plane strain compression boundary conditions. The main conclusions are:

(1) A strain localization pattern develops in the form of alternating parallel laminate bands at a very early loading stage (<0.5% global strain). The contributions of the underlying deformation systems are mainly by collinear A6/D6 slip systems with identical Schmid factors, yet alternatingly dominated in adjacent regions of the same crystal. The deformation bands form gradually from the random orientation scatter into single slip dominated regions during early deformation. Finally, the resulting single-slip bands are separated by narrow localized zones with multiple active slip systems.

(2) The overall deformation energetics shows that the laminate patterning case minimizes the energy contribution due to collinear hardening by selecting a locally prevalent slip system. Promoting spatial separation of shear in the form of alternating bands with an associated transitional interface rather than favoring homogeneous multi-slip throughout the crystal is energetically less costly for the given loading condition compared to the solutions that show no patterning.

(3) The collinear interaction plays an essential role in the formation of the deformation bands. In the presented study, the mutual interaction coefficients of dislocations for f.c.c crystals had been taken from the work of Kubin et al. (Kubin et al., 2008) for the default case (Table 5.2-1). According to Kubin et al., the strength of the collinear interaction is the strongest of all reactions (Madec et al., 2003). This causes high hardening in double slip situations involving collinear slip systems. The alternating selection of only one system is therefore favorable, which corresponds well to the simulation result of alternating laminate bands dominated by either A6 or D6 slip. It is also verified that only in the physically reasonable range of collinear interaction

strength DBs form as there is no patterning or not complete band patterning in the simulation using significantly lower or higher collinear interaction values.

(4) The systematic parameter variation enabled insights into the dynamics of the self-organizing system and reveals that purely energetic considerations may oversimplify the complex phenomena of pattern formation. Specifically, the interplay between lattice (re-)orientation and strain-hardening can lead to situations where the energetically favorable solution is not obtained. Such results emphasize the importance of using highly-resolved full-field simulations to study microstructure evolution during mechanical loading.

The results underline — in agreement with observation reported for example in (Khadyko et al., 2016) — the importance of selecting the correct hardening parameters in crystal plasticity simulations to yield correct results especially in the case of strongly textured materials. In single crystal turbine blades, the most prominent example for the use of nickel single crystals under almost constant load, the observed patterning might lead to early mechanical localization effects promoting damage initiation. Crystal plasticity simulations can also help to identify those single crystal orientations that are—for a given loading situation—not prone to develop deformation patterning.

8 Summary and outlook

8.1 Summary

In this thesis, the parametric studies were conducted for investigating the impact of individual factors on the deformation and/or damage responses of the structural heterogeneities. The effect of individual microstructural features, such as reinforcement configurations and dislocation interactions, were systematically investigated by conducting large number of crystal plasticity Fast Fourier transformation simulations. Two subjects were studied in this thesis: the first is the particle-induced damage in Fe – TiB_2 metal matrix composite steels and the second is the deformation patterning of laminate formation in single nickel crystal.

For Fe – TiB_2 metal matrix composite steels, crystal plasticity simulations were coupled with phase field damage model to predict particle damage process under tensile loading. The specific algorithm for microstructure generation was based on the random sequential adsorption (RSA) method, so that it can construct diverse particle configurations statistically and systematically. The inhomogeneity value COV_d, i.e. the coefficient of variance of the mean near-neighbour distance, can accurately quantify the degree of particle clustering. The simulation results were analyzed based on the variation of the initial damage strain ε_D and damage incubation strain ε_{Inc} as a function of certain microstructure parameters. The effect of particle clustering degree revealed a significantly increasing preference for early and rapid particle fracture in highly clustered microstructures, especially for COV_d values above 0.7. The effect of particle size revealed that particles fractured early and rapidly with large particle size (above 0.06L), whereas composites with intermediate particle size (0.03~0.06L) showed relatively good and stable damage performance. In contrast, composites with small

particle size (below 0.03L) exhibited large fluctuation of damage behaviour. The effect of particle volume fraction revealed that the optimal damage performance is in the range of 7~15vol% with a homogeneous particle distribution (COV_d below 0.4). Very poor damage performance was found for high volume fractions (> 30vol%) and very low volume fractions (< 5vol%). From the comparison analysis, these guidelines correspond well to the observations from previous experimental studies. Therefore, the Fe - TiB_2 MMCs microstructures containing more homogeneous particle distribution (COVd below 0.4) with 7~15vol% TiB_2 and avoiding large primary TiB_2 particles, are most favorable for obtaining HMS with superior ductility.

For the laminate deformation patterning in single crystal plasticity, an f.c.c nickel single crystal with initial near-Copper orientation (3° initial orientation scatter around $(112)[11\bar{1}]$) deformed in plane strain compression was conducted by crystal plasticity simulations to investigate the underlying mechanisms for the dislocation self-organization of deformation bands patterning. The initial small perturbations in lattice orientation were used to initiate the formation of deformation bands. The simulation results showed a strain localization pattern develops in the form of alternating parallel laminate bands at a very early loading stage (<0.5% global strain). This was contributed mainly by collinear A6/D6 slip systems with identical Schmid factors, yet alternatingly dominated in adjacent regions of the same crystal. The strong collinear interaction plays an essential role in the formation of the deformation bands. This causes high hardening in double slip situations involving collinear slip systems. The alternating selection of only one system is therefore favorable, which corresponds well to the simulation result of alternating laminate bands dominated by either A6 or D6 slip. Therefore, the energy contribution can be minimized by the laminate patterning case compared to the no patterning case. This indicates the spatial separation of shear in the form of deformation bands—despite the formation of expensive interface transition zones—rather than homogeneous multi-slip throughout the crystal is energetically less costly and more favorable in the overall crystal for the given loading conditions. In addition, it was also verified in this thesis that only in the physically reasonable range of collinear interaction strength can result in the formation of deformation bands as there is no patterning or

not complete band patterning in the simulation using significantly lower or higher collinear interaction values. Therefore, the selection of the correct hardening parameters is very important in crystal plasticity simulations to yield correct results especially in the case of strongly textured materials.

Overall, in this thesis, the advanced constitutive laws which couple crystal plasticity and/or phase filed method were used to simulate deformation and/or damage responses of heterogeneous materials. Incorporating the efficient spectral method, systematic study with large number of individual simulations can be conducted efficiently at low computational costs. This simulation method can not only enable insights into the dynamics of complex microstructure interactions, but also open pathways to the ICME approach with high-throughput simulations, which can further significantly speed up the material design process of the novel material with superior properties.

8.2 Outlook

1. The crystal plasticity simulations coupled with phase field damage model can be applied in other multiphase heterogeneous materials, such as dual phase steels, pearlitic-ferritic steels, complex phase steels, etc. These materials also have great potential for high strength and lightweight applications. It will hopefully further derive the guidelines through the ICME approach with high-throughput simulations for the material design of these heterogeneous materials with optimized properties.
2. In some materials, such as copper and magnesium, the heterogeneous deformation patterning is strongly influenced by the deformation twinning, besides dislocations. Deformation twinning occurs when there are not enough slip systems to accommodate plastic deformation and/or when the metal has a very low stacking fault energy. Since the twinning mechanisms can be coupled with crystal plasticity model as a kind of phase field model (Liu et al., 2018), systematic studies can be conducted to investigate the role of deformation twinning and its interaction with dislocations on the localized deformation patterning in copper and magnesium. Therefore, more complex microstructural patterns could be predicted besides the deformation bands, and deeper insights could be gained for the underlying deformation mechanisms.

9 Bibliography

Akhtar, F., 2014. Ceramic reinforced high modulus steel composites: processing, microstructure and properties. Canadian Metallurgical Quarterly 53, 253-263.

Allen, S.M., Cahn, J.W., 1979. A microscopic theory for antiphase boundary motion and its application to antiphase domain coarsening. Acta Metallurgica 27, 1085-1095.

Allison, J.E., Cole, G.S., 1993. Metal-matrix composites in the automotive industry: Opportunities and challenges. JOM 45, 19-24.

Aparicio-Fernández, R., Springer, H., Szczepaniak, A., Zhang, H., Raabe, D., 2016. In-situ metal matrix composite steels: Effect of alloying and annealing on morphology, structure and mechanical properties of TiB2 particle containing high modulus steels. Acta Materialia 107, 38-48.

ArcelorResearchGroup, 2008. Bulletin 2008/11, p. 20.

Arsenault, R.J., Shi, N., 1986. Dislocation generation due to differences between the coefficients of thermal expansion. Materials Science and Engineering 81, 175-187.

Arul Kumar, M., Mahesh, S., 2012. Banding in single crystals during plastic deformation. International Journal of Plasticity 36, 15-33.

Asaro, R.J., 1983. Micromechanics of Crystals and Polycrystals, in: Hutchinson, J.W., Wu, T.Y. (Eds.), Advances in Applied Mechanics. Elsevier, pp. 1-115.

Ashby, M.F., Evans, T., Fleck, N.A., Hutchinson, J., Wadley, H., Gibson, L., 2000. Metal foams: a design guide. Elsevier.

Ayyar, A., Crawford, G.A., Williams, J.J., Chawla, N., 2008. Numerical simulation of the effect of particle spatial distribution and strength on tensile behavior of particle reinforced composites. Computational Materials Science 44, 496-506.

Bacon, D.H., Edwards, L., Moffatt, J.E., Fitzpatrick, M.E., 2011. Synchrotron X-ray

diffraction measurements of internal stresses during loading of steel-based metal matrix composites reinforced with TiB2 particles. Acta Materialia 59, 3373-3383.

Baron, C., Springer, H., Raabe, D., 2016. Effects of Mn additions on microstructure and properties of Fe–TiB2 based high modulus steels. Materials & Design 111, 185-191.

Baron, C.H., 2017. On the design of alloys and synthesis for composite steels. RWTH Aachen University, Aachen, pp. 1 Online-Ressource (131 Seiten) : Illustrationen, Diagramme.

Barrett, C.S., Levenson, L.H., 1939. Structure of iron after drawing, swaging, and elongating in tension. Transactions of the American Institute of Mining and Metallurgical Engineers 135, 327-343.

Barrett, C.S., Levenson, L.H., 1940. The structure of aluminum after compression. Transactions of the American Institute of Mining and Metallurgical Engineers 137, 112-126.

Basinski, S.J., Basinski, Z.S., 1979. Plastic deformation and work hardening, in: Nabarro, F.R.N. (Ed.), Dislocations in solids. North-Holland Publishing Company, Amsterdam, New York, Oxford, pp. 261-362.

Bay, B., Hansen, N., Hughes, D.A., Kuhlmann-Wilsdorf, D., 1992. Overview no. 96 evolution of f.c.c. deformation structures in polyslip. Acta Metallurgica et Materialia 40, 205-219.

Bay, B., Hansen, N., Kuhlmann-Wilsdorf, D., 1989. Deformation structures in lightly rolled pure aluminium. Materials Science and Engineering: A 113, 385-397.

Beaudoin, A.J., Mecking, H., Kocks, U.F., 1996. Development of localized orientation gradients in fcc polycrystals. Philosophical Magazine A 73, 1503-1517.

Becker, R., 1991. Analysis of texture evolution in channel die compression—I. Effects of grain interaction. Acta Metallurgica et Materialia 39, 1211-1230.

Bilde-Sørensen, J.B., 1986. Deformation bands in 〈120〉 grains in coarse-grained aluminium. Materials Science and Engineering 81, 211-216.

Bishop, J.F.W., Hill, R., 1951. XLVI. A theory of the plastic distortion of a polycrystalline aggregate under combined stresses. The London, Edinburgh, and

Dublin Philosophical Magazine and Journal of Science 42, 414-427.

Blum, W., Eisenlohr, P., 2009. Dislocation mechanics of creep. Materials Science and Engineering: A 510–511, 7-13.

Bohnenkamp, U., Sandström, R., 2000. Evaluation of the elastic modulus of steels. Steel Research 71, 94-99.

Bonnet, F., Daeschler, V., Petitgand, G., 2014. High modulus steels: new requirement of automotive market. How to take up challenge? Canadian Metallurgical Quarterly 53, 243-252.

Bonollo, F., Guerriero, R., Sentimenti, E., Tangerini, I., Yang, W.L., 1991. The effect of quenching on the mechanical properties of powder metallurgically produced Al□SiC (particles) metal matrix composites. Materials Science and Engineering: A 144, 303-309.

Boselli, J., Pitcher, P.D., Gregson, P.J., Sinclair, I., 1999. Secondary phase distribution analysis via finite body tessellation. Journal of Microscopy-Oxford 195, 104-112.

Bourdin, B., Francfort, G.A., Marigo, J.J., 2000. Numerical experiments in revisited brittle fracture. Journal of the Mechanics and Physics of Solids 48, 797-826.

Bourdin, B., Larsen, C.J., Richardson, C.L., 2011. A time-discrete model for dynamic fracture based on crack regularization. International Journal of Fracture 168, 133-143.

Brechet, Y., Embury, J.D., Tao, S., Luo, L., 1991. Damage initiation in metal matrix composites. Acta Metallurgica et Materialia 39, 1781-1786.

Brisard, S., Dormieux, L., 2010. FFT-based methods for the mechanics of composites: A general variational framework. Computational Materials Science 49, 663-671.

Caceres, C.H., Griffiths, J.R., 1996. Damage by the cracking of silicon particles in an Al-7Si-0.4Mg casting alloy. Acta Materialia 44, 25-33.

Cha, L., Lartigue-Korinek, S., Walls, M., Mazerolles, L., 2012. Interface structure and chemistry in a novel steel-based composite Fe–TiB2 obtained by eutectic solidification. Acta Materialia 60, 6382-6389.

Chang, Y.W., Asaro, R.J., 1981. AN EXPERIMENTAL-STUDY OF SHEAR LOCALIZATION IN ALUMINUM-COPPER SINGLE-CRYSTALS. Acta

Metallurgica 29, 241-257.

Chawla, N., Chawla, K.K., 2013. Metal Matrix Composites. Springer-Verlag New York.

Chawla, N., Shen, Y.L., 2001. Mechanical behavior of particle reinforced metal matrix composites. Advanced Engineering Materials 3, 357-370.

Chin, G.Y., Wonsiewicz, B.C., 1969. Deformation banding and stability of (100)-(111) fiber textures of fcc metals. Transactions of the Metallurgical Society of Aime 245, 871-&.

Cordero, B., Gomez, V., Platero-Prats, A.E., Reves, M., Echeverria, J., Cremades, E., Barragan, F., Alvarez, S., 2008. Covalent radii revisited. Dalton Transactions, 2832-2838.

Dammak, M., Gaspérini, M., Barbier, D., 2014. Microstructural evolution of iron based metal–matrix composites submitted to simple shear. Materials Science and Engineering: A 616, 123-131.

Dammak, M., Ksaeir, I., Brinza, O., Gasperini, M., 2013. Experimental analysis of damage of Fe-TiB2 metal matrix composites under complex loading. 21ème Congrès Français de Mécanique, Bordeaux.

Davidson, D.L., 1993. Fatigue and fracture toughness of aluminium alloys reinforced with SiC and alumina particles. Composites 24, 248-255.

Davis, L.C., Andres, C., Allison, J.E., 1998. Microstructure and strengthening of metal matrix composites. Materials Science and Engineering: A 249, 40-45.

Dequiedt, J.L., Denoual, C., Madec, R., 2015. Heterogeneous deformation in ductile FCC single crystals in biaxial stretching: the influence of slip system interactions. Journal of the Mechanics and Physics of Solids 83, 301-318.

Devincre, B., Hoc, T., Kubin, L.P., 2005. Collinear interactions of dislocations and slip systems. Materials Science and Engineering: A 400-401, 182-185.

Devincre, B., Kubin, L., Hoc, T., 2006. Physical analyses of crystal plasticity by DD simulations. Scripta Materialia 54, 741-746.

Diehl, M., Shanthraj, P., Eisenlohr, P., Roters, F., 2016. Neighborhood influences on stress and strain partitioning in dual-phase microstructures. Meccanica 51, 429-441.

Dmitrieva, O., Dondl, P.W., Müller, S., Raabe, D., 2009. Lamination microstructure in

shear deformed copper single crystals. Acta Materialia 57, 3439-3449.

Duggan, B.J., Hatherly, M., Hutchinson, W.B., Wakefield, P.T., 1978. Deformation structures and textures in cold-rolled 70:30 brass. Metal Science 12, 343-351.

Eisenlohr, P., Diehl, M., Lebensohn, R.A., Roters, F., 2013. A spectral method solution to crystal elasto-viscoplasticity at finite strains. International Journal of Plasticity 46, 37-53.

Eyre, D.J., Milton, G.W., 1999. A fast numerical scheme for computing the response of composites using grid refinement*. Eur. Phys. J. AP 6, 41-47.

F.Ashby, M., 2005. Materials Selection in Mechanical Design, Third ed. Butterworth-Heinemann, Burlington, MA, USA.

Feng, Y., 2013. Strengthening of Steels by Ceramic Phases. Fakultät für Georessourcen und Materialtenik, RWTH Aachen.

Fischmeister, H.F., Navara, E., Easterling, K.E., 1972. Effects of Alloying on Structural Stability and Cohesion between Phases in Oxide/Metal Composites. Metal Science Journal 6, 211-215.

Franciosi, P., Berveiller, M., Zaoui, A., 1980. Latent hardening in copper and aluminium single crystals. Acta Metallurgica 28, 273-283.

Gil Sevillano, J., 1993. The Cold Worked State. Materials Science Forum 113-115, 19-28.

Gottstein, G., 2004. Physical Foundations of Materials Science. Springer Berlin Heidelberg.

Gracio, J.J., Fernandes, J.V., Schmitt, J.H., 1989. Effect of grain size on substructural evolution and plastic behaviour of copper. Materials Science and Engineering: A 118, 97-105.

Hadjem-Hamouche, Z., Chevalier, J.-P., Cui, Y., Bonnet, F., 2012. Deformation Behavior and Damage Evaluation in a New Titanium Diboride (TiB2) Steel-Based Composite. steel research international 83, 538-545.

Hadjem-Hamouche, Z., Derrien, K., Héripré, E., Chevalier, J.P., 2018. In-situ experimental and numerical studies of the damage evolution and fracture in a Fe-TiB2 composite. Materials Science and Engineering: A 724, 594-605.

Hall, J.N., Wayne Jones, J., Sachdev, A.K., 1994. Particle size, volume fraction and matrix strength effects on fatigue behavior and particle fracture in 2124 aluminum-SiCp composites. Materials Science and Engineering: A 183, 69-80.

Harren, S.V., Dève, H.E., Asaro, R.J., 1988. Shear band formation in plane strain compression. Acta Metallurgica 36, 2435-2480.

Hauert, A., Rossoll, A., Mortensen, A., 2009. Particle fracture in high-volume-fraction ceramic-reinforced metals: Governing parameters and implications for composite failure. Journal of the Mechanics and Physics of Solids 57, 1781-1800.

Hirsch, J., Lücke, K., Hatherly, M., 1988. Overview No. 76: Mechanism of deformation and development of rolling textures in polycrystalline f.c.c. Metals—III. The influence of slip inhomogeneities and twinning. Acta Metallurgica 36, 2905-2927.

Hirth, J.P., Lothe, J., 1982. Theory of Dislocations. Krieger Publishing Company.

Honeycombe, R.W.K., 1951. Inhomogeneities in the plastic deformation of metal crystal .2. X-ray and optical micrography of aluminum. Journal of the Institute of Metals 80, 49-&.

Howe, J.M., 1993. Bonding, structure, and properties of metal/ceramic interfaces: Part 1 Chemical bonding, chemical reaction, and interfacial structure. International Materials Reviews 38, 233-256.

Hu, H., 1980. Elastic Properties of Cold-Rolled and Annealed Sheets of Phosphorus Steel Having High Normal Plastic anisotropy. Texture of Crystalline Solids 4, 111-127.

Huang, M.X., He, B.B., Wang, X., Yi, H.L., 2015. Interfacial plasticity of a TiB2-reinforced steel matrix composite fabricated by eutectic solidification. Scripta Materialia 99, 13-16.

Huang, X., Winther, G., 2007. Dislocation structures. Part I. Grain orientation dependence. Philosophical Magazine 87, 5189-5214.

Hutchinson, J.W., 1976. Bounds and self-consistent estimates for creep of polycrystalline materials. Proceedings of the Royal Society of London. A. Mathematical and Physical Sciences 348, 101.

Jamaati, R., Amirkhanlou, S., Toroghinejad, M.R., Niroumand, B., 2011. Effect of

particle size on microstructure and mechanical properties of composites produced by ARB process. Materials Science and Engineering: A 528, 2143-2148.

Jia, N., Eisenlohr, P., Roters, F., Raabe, D., Zhao, X., 2012a. Orientation dependence of shear banding in face-centered-cubic single crystals. Acta Materialia 60, 3415-3434.

Jia, N., Roters, F., Eisenlohr, P., Kords, C., Raabe, D., 2012b. Non-crystallographic shear banding in crystal plasticity FEM simulations: Example of texture evolution in α-brass. Acta Materialia 60, 1099-1115.

Kübarsepp, J., 1992. Hard metals with steel binder. Tallinn Technical University, Tallinn.

Kaczmar, J.W., Pietrzak, K., Włosiński, W., 2000. The production and application of metal matrix composite materials. Journal of Materials Processing Technology 106, 58-67.

Kang, J.H., Rivera-Díaz-del-Castillo, P.E.J., 2013. Carbide dissolution in bearing steels. Computational Materials Science 67, 364-372.

Khadyko, M., Dumoulin, S., Cailletaud, G., Hopperstad, O.S., 2016. Latent hardening and plastic anisotropy evolution in AA6060 aluminium alloy. International Journal of Plasticity 76, 51-74.

Kim, P., Hanen, A., Jean-Jacques, M., Corrado, M., 2010. Gradient Damage Models and Their Use to Approximate Brittle Fracture. International Journal of Damage Mechanics 20, 618-652.

Kochmann, D.M., Hackl, K., 2011. The evolution of laminates in finite crystal plasticity: a variational approach. Continuum Mechanics and Thermodynamics 23, 63-85.

Kocks, U.F., Mecking, H., 2003. Physics and phenomenology of strain hardening: the FCC case. Progress in Materials Science 48, 171-273.

Kords, C., 2013. On the Role of Dislocation Transport in the Constitutive Description of Crystal Plasticity. Berlin: epubli GmbH.

Kouzeli, M., Weber, L., San Marchi, C., Mortensen, A., 2001. Influence of damage on the tensile behaviour of pure aluminium reinforced with ≥40 vol. pct alumina particles. Acta Materialia 49, 3699-3709.

Kubin, L., 2013. Dislocations, Mesoscale Simulations and Plastic Flow. OUP Oxford.

Kubin, L., Devincre, B., Hoc, T., 2008. Modeling dislocation storage rates and mean free paths in face-centered cubic crystals. Acta Materialia 56, 6040-6049.

Kuhlmann-Wilsdorf, D., 1989. Theory of plastic deformation: - properties of low energy dislocation structures. Materials Science and Engineering: A 113, 1-41.

Kuhlmann-Wilsdorf, D., 1999a. Overview No. 131"Regular" deformation bands (DBs) and the LEDS hypothesis. Acta Materialia 47, 1697-1712.

Kuhlmann-Wilsdorf, D., 1999b. The theory of dislocation-based crystal plasticity. Philosophical Magazine A 79, 955-1008.

Kuhlmann-wilsdorf, D., Wilsdorf, H., 1953. The surface structures of deformed aluminium, copper, silver and alpha-brass and their theoretical interpretation. Acta Metallurgica 1, 394-413.

Kulikowski, Z., Godfrey, T.M.T., Wisbey, A., Goodwin, P.S., Langlais, F., Flower, H.M., Zheng, J.G., Davies, D.P., 2000a. Mechanical and microstructural behaviour of a particulate reinforced steel for structural applications. Materials Science and Technology 16, 1453-1464.

Kulikowski, Z., Wisbey, A., Godfrey, T.M.T., Goodwin, P.S., Flower, H.M., 2000b. Mechanical properties of high performance lightweight steels. Materials Science and Technology 16, 925-928.

Kulkarni, S.S., Starke, E.A., Kuhlmann-Wilsdorf, D., 1998. Some observations on deformation banding and correlated microstructures of two aluminum alloys compressed at different temperatures and strain rates. Acta Materialia 46, 5283-5301.

Kuroda, M., Tvergaard, V., 2007. Effects of texture on shear band formation in plane strain tension/compression and bending. International Journal of Plasticity 23, 244-272.

Lartigue-Korinek, S., Walls, M., Haneche, N., Cha, L., Mazerolles, L., Bonnet, F., 2015. Interfaces and defects in a successfully hot-rolled steel-based composite Fe–TiB2. Acta Materialia 98, 297-305.

Lebensohn, R.A., 2001. N-site modeling of a 3D viscoplastic polycrystal using Fast Fourier Transform. Acta Materialia 49, 2723-2737.

Lebensohn, R.A., Escobedo, J.P., Cerreta, E.K., Dennis-Koller, D., Bronkhorst, C.A.,

Bingert, J.F., 2013. Modeling void growth in polycrystalline materials. Acta Materialia 61, 6918-6932.

Lebensohn, R.A., Kanjarla, A.K., Eisenlohr, P., 2012. An elasto-viscoplastic formulation based on fast Fourier transforms for the prediction of micromechanical fields in polycrystalline materials. International Journal of Plasticity 32-33, 59-69.

Lee, C.S., Duggan, B.J., 1993. Deformation banding and copper-type rolling textures. Acta Metallurgica et Materialia 41, 2691-2699.

Lee, C.S., Duggan, B.J., Smallman, R.E., 1993. A theory of deformation banding in cold rolling. Acta Metallurgica et Materialia 41, 2265-2270.

Lee, E.H., 1969. ELASTIC-PLASTIC DEFORMATION AT FINITE STRAINS. Journal of Applied Mechanics 36, 1-&.

Lee, S.B., Lebensohn, R.A., Rollett, A.D., 2011. Modeling the viscoplastic micromechanical response of two-phase materials using Fast Fourier Transforms. International Journal of Plasticity 27, 707-727.

Leffers, T., 2001. A model for rolling deformation with grain subdivision. Part I: The initial stage. International Journal of Plasticity 17, 469-489.

Leslie, W.C., 1972. Iron and its dilute substitutional solid solutions. Metallurgical and Materials Transactions B 3, 5-26.

Lesuer, D.R., Syn, C.K., Sherby, O.D., Wadsworth, J., Lewandowski, J.J., Hunt, W.H., 1996. Mechanical behaviour of laminated metal composites. International Materials Reviews 41, 169-197.

Lewandowski, J.J., 2000. 3.07 - Fracture and Fatigue of Particulate MMCs, in: Kelly, A., Zweben, C. (Eds.), Comprehensive Composite Materials. Pergamon, Oxford, pp. 151-187.

Lewandowski, J.J., Liu, C., Hunt, W.H., 1989. Effects of matrix microstructure and particle distribution on fracture of an aluminum metal matrix composite. Materials Science and Engineering a-Structural Materials Properties Microstructure and Processing 107, 241-255.

Li, B., Liu, Y., Li, J., Gao, S., Cao, H., He, L., 2010. Effect of tungsten addition on the microstructure and tensile properties of in situ TiB2/Fe composite produced by

vacuum induction melting. Materials & Design 31, 877-883.

Li, Y., Lin, Z., Jiang, A., Chen, G., 2003. Use of high strength steel sheet for lightweight and crashworthy car body. Materials & Design 24, 177-182.

Li, Y.Z., Huang, M.X., 2017. Interfacial Strength Characterization in a High-Modulus Low-Density Steel-Based Fe-TiB2 Composite, in: Ikhmayies, S., Li, B., Carpenter, J.S., Li, J., Hwang, J.-Y., Monteiro, S.N., Firrao, D., Zhang, M., Peng, Z., Escobedo-Diaz, J.P., Bai, C., Kalay, Y.E., Goswami, R., Kim, J. (Eds.), Characterization of Minerals, Metals, and Materials 2017. Springer International Publishing, Cham, pp. 453-460.

Li, Y.Z., Luo, Z.C., Yi, H.L., Huang, M.X., 2016. Damage Mechanisms of a TiB2-Reinforced Steel Matrix Composite for Lightweight Automotive Application. Metallurgical and Materials Transactions E 3, 203-208.

Liu, B., Raabe, D., Roters, F., Eisenlohr, P., Lebensohn, R.A., 2010. Comparison of finite element and fast Fourier transform crystal plasticity solvers for texture prediction. Modelling and Simulation in Materials Science and Engineering 18, 085005.

Liu, C., Shanthraj, P., Diehl, M., Roters, F., Dong, S., Dong, J., Ding, W., Raabe, D., 2018. An integrated crystal plasticity–phase field model for spatially resolved twin nucleation, propagation, and growth in hexagonal materials. International Journal of Plasticity 106, 203-227.

Llorca, J., 1995. An analysis of the influence of reinforcement fracture on the strength of discontinuously-reinforced metal-matrix composites. Acta Metallurgica et Materialia 43, 181-192.

Lloyd, D.J., 1991. Aspects of fracture in particulate reinforced metal matrix composites. Acta Metallurgica Et Materialia 39, 59-71.

Lloyd, D.J., 1994. Particle reinforced aluminium and magnesium matrix composites. International Materials Reviews 39, 1-23.

Lu, Y.C., Sass, S.L., 1995. Deformation processes in the vicinity of metal—ceramic interfaces. Acta Metallurgica et Materialia 43, 3283-3293.

Münstermann, S., Feng, Y., Bleck, W., 2014. Influencing parameters on elastic modulus

of steels. Canadian Metallurgical Quarterly 53, 264-273.

Ma, A., Roters, F., 2004. A constitutive model for fcc single crystals based on dislocation densities and its application to uniaxial compression of aluminium single crystals. Acta Materialia 52, 3603-3612.

Ma, A., Roters, F., Raabe, D., 2006. A dislocation density based constitutive model for crystal plasticity FEM including geometrically necessary dislocations. Acta Materialia 54, 2169-2179.

Madec, R., Devincre, B., Kubin, L., Hoc, T., Rodney, D., 2003. The Role of Collinear Interaction in Dislocation-Induced Hardening. Science 301, 1879-1882.

Mahesh, S., 2006. Deformation banding and shear banding in single crystals. Acta Materialia 54, 4565-4574.

Michel, J.C., Moulinec, H., Suquet, P., 2000. A computational method based on augmented Lagrangians and fast Fourier Transforms for composites with high contrast. Cmes-Computer Modeling in Engineering & Sciences 1, 79-88.

Miehe, C., Aldakheel, F., Raina, A., 2016. Phase field modeling of ductile fracture at finite strains: A variational gradient-extended plasticity-damage theory. International Journal of Plasticity 84, 1-32.

Miehe, C., Lambrecht, M., Gürses, E., 2004. Analysis of material instabilities in inelastic solids by incremental energy minimization and relaxation methods: evolving deformation microstructures in finite plasticity. Journal of the Mechanics and Physics of Solids 52, 2725-2769.

Mika, D.P., Dawson, P.R., 1998. Effects of grain interaction on deformation in polycrystals. Materials Science and Engineering: A 257, 62-76.

Milman, V., Warren, M.C., 2001. Elastic properties of TiB2 and MgB2. Journal of Physics: Condensed Matter 13, 5585.

Miracle, D.B., 2005. Metal matrix composites – From science to technological significance. Composites Science and Technology 65, 2526-2540.

Monchiet, V., Bonnet, G., 2011. A polarization-based FFT iterative scheme for computing the effective properties of elastic composites with arbitrary contrast. International Journal for Numerical Methods in Engineering 89, 1419-1436.

Morii, K., Mecking, H., Nakayama, Y., 1985. Development of shear bands in fcc single-crystals. Acta Metallurgica 33, 379-386.

Moulinec, H., Suquet, P., 1994. A fast numerical-method for computing the linear and nonlinear mechanical-properties of composites. Comptes Rendus De L Academie Des Sciences Serie Ii 318, 1417-1423.

Moulinec, H., Suquet, P., 1998. A numerical method for computing the overall response of nonlinear composites with complex microstructure. Computer Methods in Applied Mechanics and Engineering 157, 69-94.

Munro, R.G., 2000. Material properties of titanium diboride. Journal of Research of the National Institute of Standards and Technology 105, 709-720.

Myles, J.P., Flenley, E.C., Fieller, N.R.J., Atkinson, H.V., Jones, H., 1995. Statistical tests for clustering of second phases in composite materials. Philosophical Magazine A 72, 515-528.

Naidich, J.V., 1981. The Wettability of Solids by Liquid Metals, in: Cadenhead, D.A., Danielli, J.F. (Eds.), Progress in Surface and Membrane Science. Elsevier, pp. 353-484.

Nakanishi, H., Kakihara, K., Nakayama, A., Murayama, T., 2002. Development of aluminum metal matrix composites (Al-MMC) brake rotor and pad. JSAE Review 23, 365-370.

Nakayama, Y., Morii, K., 1987. Microstructure and shear band formation in rolled single-crystals of Al-Mg alloy. Acta Metallurgica 35, 1747-1755.

Nardone, V.C., Prewo, K.M., 1986. On the strength of discontinuous silicon carbide reinforced aluminum composites. Scripta Metallurgica 20, 43-48.

Neuhaus, R., Schwink, C., 1992. On the flow stress of [100]- and [111]-oriented Cu-Mn single crystals: A transmission electron microscopy study. Philosophical Magazine A 65, 1463-1484.

Novotny, G.M., Ardell, A.J., 2001. Precipitation of Al3Sc in binary Al–Sc alloys. Materials Science and Engineering: A 318, 144-154.

Ortiz, M., Repetto, E.a., 1999. Nonconvex energy minimization and dislocation structures in ductile single crystals. Journal of the Mechanics and Physics of Solids

47, 397-462.

Ortiz, M., Repetto, E.A., Stainier, L., 2000. A theory of subgrain dislocation structures. Journal of the Mechanics and Physics of Solids 48, 2077-2114.

Pagounis, E., Lindroos, V.K., 1998. Processing and properties of particulate reinforced steel matrix composites. Materials Science and Engineering: A 246, 221-234.

Paul, H., Driver, J.H., Jasieński, Z., 2002. Shear banding and recrystallization nucleation in a Cu–2%Al alloy single crystal. Acta Materialia 50, 815-830.

Paul, H., Morawiec, A., Driver, J.H., Bouzy, E., 2009. On twinning and shear banding in a Cu-8 at.% Al alloy plane strain compressed at 77 K. International Journal of Plasticity 25, 1588-1608.

Peirce, D., Asaro, R.J., Needleman, A., 1982. An analysis of nonuniform and localized deformation in ductile single crystals. Acta Metallurgica 30, 1087-1119.

Peirce, D., Asaro, R.J., Needleman, A., 1983. Material rate dependence and localized deformation in crystalline solids. Acta Metallurgica 31, 1951-1976.

Petryk, H., Kursa, M., 2013. The energy criterion for deformation banding in ductile single crystals. Journal of the Mechanics and Physics of Solids 61, 1854-1875.

Piercy, G.R., Cahn, R.W., Cottrell, A.H., 1955. A study of primary and conjugate slip in crystals of alpha-brass. Acta Metallurgica 3, 331-338.

Prakash, A., Lebensohn, R.A., 2009. Simulation of micromechanical behavior of polycrystals: finite elements versus fast Fourier transforms. Modelling and Simulation in Materials Science and Engineering 17, 064010.

Pramanik, S., Suwas, S., Ray, R.K., 2014. Influence of crystallographic texture and microstructure on elastic modulus of steels. Canadian Metallurgical Quarterly 53, 274-281.

Raabe, D., Roters, F., 2004. Using texture components in crystal plasticity finite element simulations. International Journal of Plasticity 20, 339-361.

Raabe, D., Sachtleber, M., Weiland, H., Scheele, G., Zhao, Z., 2003. Grain-scale micromechanics of polycrystal surfaces during plastic straining. Acta Materialia 51, 1539-1560.

Raabe, D., Sachtleber, M., Zhao, Z., Roters, F., Zaefferer, S., 2001. Micromechanical

and macromechanical effects in grain scale polycrystal plasticity experimentation and simulation. Acta Materialia 49, 3433-3441.

Raabe, D., Zhao, Z., Roters, F., 2004. Study on the orientational stability of cube-oriented FCC crystals under plane strain by use of a texture component crystal plasticity finite element method. Scripta Materialia 50, 1085-1090.

Rana, R., 2014. High Modulus Steels. Canadian Metallurgical Quarterly 53, 241-242.

Rana, R., Lahaye, C., Ray, R.K., 2014. Overview of Lightweight Ferrous Materials: Strategies and Promises. JOM 66, 1734-1746.

Reina, C., Conti, S., 2014. Kinematic description of crystal plasticity in the finite kinematic framework: A micromechanical understanding of F=FeFp. Journal of the Mechanics and Physics of Solids 67, 40-61.

Reuber, C., Eisenlohr, P., Roters, F., Raabe, D., 2014. Dislocation density distribution around an indent in single-crystalline nickel: Comparing nonlocal crystal plasticity finite-element predictions with experiments. Acta Materialia 71, 333-348.

Rice, J.R., 1971. Inelastic constitutive relations for solids: An internal-variable theory and its application to metal plasticity. Journal of the Mechanics and Physics of Solids 19, 433-455.

Rintoul, M.D., Torquato, S., 1997. Reconstruction of the Structure of Dispersions. Journal of Colloid and Interface Science 186, 467-476.

Rohatgi, P.K., Asthana, R., Das, S., 1986. Solidification, structures, and properties of cast metal-ceramic particle composites. International Metals Reviews 31, 115-139.

Roters, F., 2011. Advanced material models for the crystal plasticity finite element method : development of a general CPFEM framework. Publikationsserver der RWTH Aachen University, Germany.

Roters, F., Diehl, M., Shanthraj, P., Eisenlohr, P., Reuber, C., Wong, S.L., Maiti, T., Ebrahimi, A., Hochrainer, T., Fabritius, H.-O., Nikolov, S., Friák, M., Fujita, N., Grilli, N., Janssens, K.G.F., Jia, N., Kok, P.J.J., Ma, D., Meier, F., Werner, E., Stricker, M., Weygand, D., Raabe, D., 2018. DAMASK - The Düsseldorf Advanced Material Simulation Kit for Modeling Multi-Physics Crystal Plasticity, Thermal, and Damage Phenomena from the Single Crystal up to the Component Scale. Computational

Materials Science, accepted for publication.

Roters, F., Eisenlohr, P., Hantcherli, L., Tjahjanto, D.D., Bieler, T.R., Raabe, D., 2010. Overview of constitutive laws, kinematics, homogenization and multiscale methods in crystal plasticity finite-element modeling: Theory, experiments, applications. Acta Materialia 58, 1152-1211.

Roters, F., Eisenlohr, P., Kords, C., Tjahjanto, D.D., Diehl, M., Raabe, D., 2012. DAMASK: the Düsseldorf Advanced MAterial Simulation Kit for studying crystal plasticity using an FE based or a spectral numerical solver. Procedia IUTAM 3, 3-10.

Saada, G., 1960. On hardening due to the recombination of dislocations. Acta Metallurgica 8, 841-847.

Sachs, G., 1928. On the derivation of a condition of flowing. Zeitschrift Des Vereines Deutscher Ingenieure 72, 734-736.

Sachtleber, M., Zhao, Z., Raabe, D., 2002. Experimental investigation of plastic grain interaction. Materials Science and Engineering: A 336, 81-87.

Saimoto, S., Hosford, W.F., Backofen, W.A., 1965. Ductile fracture in copper single crystals. The Philosophical Magazine: A Journal of Theoretical Experimental and Applied Physics 12, 319-333.

Sandström, R., Korzhavyi, P., 2014. Use of elastic constants based on ab initio computation in materials optimisation of austenitic stainless steels. Canadian Metallurgical Quarterly 53, 282-291.

Schmid, E., Boas, W., 1968. Plasticity of crystals: with special reference to metals. Chapman & Hall.

Schoeck, G., Frydman, R., 1972. The Contribution of the Dislocation Forest to the Flow Stress. physica status solidi (b) 53, 661-673.

Segurado, J., González, C., Llorca, J., 2003. A numerical investigation of the effect of particle clustering on the mechanical properties of composites. Acta Materialia 51, 2355-2369.

Segurado, J., Llorca, J., 2006. Computational micromechanics of composites: The effect of particle spatial distribution. Mechanics of Materials 38, 873-883.

Shanthraj, P., Diehl, M., Eisenlohr, P., Roters, F., 2017a. Spectral solvers for crystal

plasticity and multi-physics simulations. Mechanics of Materials, Micromechanics, edited by Chun-Hway Hsueh, Siegfried Schmauder and Yutaka Kagawa.

Shanthraj, P., Eisenlohr, P., Diehl, M., Roters, F., 2015. Numerically robust spectral methods for crystal plasticity simulations of heterogeneous materials. International Journal of Plasticity 66, 31-45.

Shanthraj, P., Sharma, L., Svendsen, B., Roters, F., Raabe, D., 2016. A phase field model for damage in elasto-viscoplastic materials. Computer Methods in Applied Mechanics and Engineering 312, 167-185.

Shanthraj, P., Svendsen, B., Sharma, L., Roters, F., Raabe, D., 2017b. Elasto-viscoplastic phase field modelling of anisotropic cleavage fracture. Journal of the Mechanics and Physics of Solids 99, 19-34.

Shanthraj, P., Zikry, M.A., 2012. Optimal microstructures for martensitic steels. Journal of Materials Research 27, 1598-1611.

Shurin, A.K., Panarin, V.E., 1974. Phase Equilibria and Structure of Alloys of Iron with TiB2, ZrB2 and HfB2. Izv. Akad. Nauk SSSR, Met. 5, 235-239.

Shurin, A.K., Panarin, V.E., 1984. Phase diagrams for iron with interstitial phases as a basis for developing wear-resistant and eutectic steels. Metal Science and Heat Treatment 26, 166-169.

Sigl, L.S., Schwetz, K.A., 1991. TIB2-BASED CEMENTED BORIDES - A NEW GENERATION OF HARDMETALS. Powder Metallurgy International 23, 221-224.

Sokolova, O.A., Kühn, M., Palkowski, H., 2012. Deep drawing properties of lightweight steel/polymer/steel sandwich composites. Archives of Civil and Mechanical Engineering 12, 105-112.

Song, S.G., Shi, N., Gray, G.T., Roberts, J.A., 1996. Reinforcement shape effects on the fracture behavior and ductility of particulate-reinforced 6061-Al matrix composites. Metallurgical and Materials Transactions A 27, 3739-3746.

Speich, G.R., Schwoeble, A.J., Leslie, W.C., 1972. Elastic constants of binary iron-base alloys. Metallurgical Transactions 3, 2031-2037.

Springer, H., Aparicio Fernandez, R., Duarte, M.J., Kostka, A., Raabe, D., 2015. Microstructure refinement for high modulus in-situ metal matrix composite steels via

controlled solidification of the system Fe–TiB2. Acta Materialia 96, 47-56.

Springer, H., Baron, C., Szczepaniak, A., Uhlenwinkel, V., Raabe, D., 2017. Stiff, light, strong and ductile: nano-structured High Modulus Steel. Scientific Reports 7, 2757.

Sun, C., Song, M., Wang, Z., He, Y., 2011. Effect of Particle Size on the Microstructures and Mechanical Properties of SiC-Reinforced Pure Aluminum Composites. Journal of Materials Engineering and Performance 20, 1606-1612.

Suzuki, K., Kikuchi, N., 1991. A homogenization method for shape and topology optimization. Computer Methods in Applied Mechanics and Engineering 93, 291-318.

Szczepaniak, A., Springer, H., Aparicio-Fernández, R., Baron, C., Raabe, D., 2017. Strengthening Fe – TiB2 based high modulus steels by precipitations. Materials & Design 124, 183-193.

Tanaka, K., 2000. Ultra High Modulus Steel Reinforced with Titanium Boride Particles. R&D Review of Toyota CRDL 35.

Tanaka, K., Saito, T., 1999. Phase equilibria in TiB2-reinforced high modulus steel. Journal of Phase Equilibria 20, 207.

Tasan, C.C., Diehl, M., Yan, D., Zambaldi, C., Shanthraj, P., Roters, F., Raabe, D., 2014a. Integrated experimental–simulation analysis of stress and strain partitioning in multiphase alloys. Acta Materialia 81, 386-400.

Tasan, C.C., Hoefnagels, J.P.M., Diehl, M., Yan, D., Roters, F., Raabe, D., 2014b. Strain localization and damage in dual phase steels investigated by coupled in-situ deformation experiments and crystal plasticity simulations. International Journal of Plasticity 63, 198-210.

Taylor, G.I., 1934. The Mechanism of Plastic Deformation of Crystals. Part I. Theoretical. Proceedings of the Royal Society of London A: Mathematical, Physical and Engineering Sciences 145, 362-387.

Taylor, G.I., 1938. Plastic strain in metals. Journal of the Institute of Metals 62, 307-324.

Telle, R., Petzow, G., 1988. Strengthening and toughening of boride and carbide hard material composites. Materials Science and Engineering: A 105–106, Part 1, 97-104.

Tjong, S.C., Ma, Z.Y., 2000. Microstructural and mechanical characteristics of in situ metal matrix composites. Materials Science and Engineering: R: Reports 29, 49-113.

Wang, D., Diehl, M., Roters, F., Raabe, D., 2018a. On the role of the collinear dislocation interaction in deformation patterning and laminate formation in single crystal plasticity. Mechanics of Materials 125, 70-79.

Wang, D., Shanthraj, P., Springer, H., Raabe, D., 2018b. Particle-induced damage in Fe-TiB2 high stiffness metal matrix composites steels. Materials & Design 160, 557-571.

Wang, Y., Zhang, Z.Q., Wang, H.Y., Ma, B.X., Jiang, Q.C., 2006. Effect of Fe content in Fe–Ti–B system on fabricating TiB2 particulate locally reinforced steel matrix composites. Materials Science and Engineering: A 422, 339-345.

Weiland, H., Nardiello, J., Zaefferer, S., Cheong, S., Papazian, J., Raabe, D., 2009. Microstructural aspects of crack nucleation during cyclic loading of AA7075-T651. Engineering Fracture Mechanics 76, 709-714.

Werner, E., Wesenjak, R., Fillafer, A., Meier, F., Krempaszky, C., 2016. Microstructure-based modelling of multiphase materials and complex structures. Continuum Mechanics and Thermodynamics 28, 1325-1346.

Wert, J.A., Huang, X., Inoko, F., 2003. Deformation bands in a [110] aluminium single crystal strained in tension. Proceedings of the Royal Society of London. Series A: Mathematical, Physical and Engineering Sciences 459, 85.

Williams, J.J., Flom, Z., Amell, A.A., Chawla, N., Xiao, X., De Carlo, F., 2010. Damage evolution in SiC particle reinforced Al alloy matrix composites by X-ray synchrotron tomography. Acta Materialia 58, 6194-6205.

Xue, Z., Hutchinson, J.W., 2007. Neck retardation and enhanced energy absorption in metal–elastomer bilayers. Mechanics of Materials 39, 473-487.

Yang, J., Pickard, S.M., Cady, C., Evans, A.G., Mehrabian, R., 1991. The stress/strain behavior of aluminum matrix composites with discontinuous reinforcements. Acta Metallurgica et Materialia 39, 1863-1869.

Yang, N., Boselli, J., Sinclair, I., 2001. Simulation and quantitative assessment of homogeneous and inhomogeneous particle distributions in particulate metal matrix

composites. Journal of Microscopy-Oxford 201, 189-200.

Zeman, J., Vondřejc, J., Novák, J., Marek, I., 2010. Accelerating a FFT-based solver for numerical homogenization of periodic media by conjugate gradients. Journal of Computational Physics 229, 8065-8071.

Zhang, H., Springer, H., Aparicio-Fernández, R., Raabe, D., 2016. Improving the mechanical properties of Fe – TiB2 high modulus steels through controlled solidification processes. Acta Materialia 118, 187-195.

Zhao, Z., Ramesh, M., Raabe, D., Cuitiño, A.M., Radovitzky, R., 2008. Investigation of three-dimensional aspects of grain-scale plastic surface deformation of an aluminum oligocrystal. International Journal of Plasticity 24, 2278-2297.

List of Figures

List of Tables

Abstract

Structural heterogeneities arise in most metallic materials on the microscopic scale prior or after deformation. On the one hand such heterogeneities have great potential to achieve specific properties for high strength and lightweight applications, but on the other hand the ductility and toughness of materials could be critically reduced by damage initiation which is promoted by such heterogeneities. In this thesis, the effect of individual microstructure features and underlying dislocation interactions on mechanical and/or damage responses of materials were investigated by systematic simulation studies. Crystal plasticity Fast Fourier transformation simulations were conducted to gain deep insights into the complex interactions between individual microstructural and micromechanical mechanisms in heterogeneous structures. Two subjects were studied in this thesis: the first is the particle-induced damage in Fe – TiB_2 metal matrix composites steels and the second is the formation of laminate deformation patterning in nickel single crystal.

Fe – TiB_2 metal matrix composites, termed high modulus steels due to their high specific stiffness, have great potential for lightweight design applications. However, the toughness of these steels is critically reduced by the presence of the brittle TiB_2 particles. Due to the multitude of parameters affecting microstructural damage, experimental studies are complex and inefficient to identify the impact of particle microstructure on fracture toughness. In this thesis, a computational simulation approach to derive guidelines for optimizing the mechanical properties of high modulus steels was conducted. Key microstructural parameters such as particle clustering degree, size and volume fraction were investigated. Model geometries were statistically and systematically generated with varied particle configurations from random to clustered

distributions. Simulations were then performed using a crystal plasticity Fast Fourier Transformation simulation method coupled with a novel phase field damage model. The effect of individual particle parameters on particle damage revealed that microstructures with homogeneous particle distributions of 7~15% volume fraction TiB_2 devoid of large primary TiB_2 particles (the primary precipitates for hypo-eutectic composition), are most favorable for obtaining high modulus steels with increased toughness.

Deformation patterning in the form of deformation bands is observed in single crystals under suitable loading conditions. In this thesis, the reasons for this severe deformation patterning were investigated through crystal plasticity simulations. An f.c.c nickel single crystal with initial near-Copper orientation was deformed in plane strain compression boundary conditions. It was found the resulting strain partitioning in the form of alternating parallel bands initiates at a very early loading stage and sharpens with ongoing deformation. It revealed that the microstructure lamination is the result of a complex interplay between available deformation systems, strain hardening, kinematics, and deformation energetics: (i) the dislocation collinear interaction plays an essential role in the formation of the deformation bands under the imposed boundary conditions; (ii) the laminate patterning case minimizes the energy contribution due to strong collinear interaction strength by selecting a locally prevalent slip system. This behaviour is explained by the lower global deformation energy in comparison to a homogeneous double slip behaviour. It also demonstrated that only interaction strength values in the range predicted by discrete dislocation dynamic simulations result in deformation bands.

Altogether, the effectiveness and possibilities of systematic crystal plasticity simulations were presented and discussed in this thesis. The complex interactions between individual microstructural and micromechanical mechanisms in structure heterogeneities were identified. Based on the effect of individual microstructural factors, the optimized microstructure or damage tolerant microstructures can be derived, and deeper insights can be gained for the underlying deformation and damage mechanisms.

Zusammenfassung

Strukturelle Heterogenitäten entstehen in den meisten metallischen Materialien auf den mikroskopischen Skalen vor oder nach der Verformung. Einerseits bieten solche Heterogenitäten ein großes Potenzial, um spezifische Eigenschaften für hochfeste und leichte Anwendungen zu erreichen, andererseits können aber die Duktilität und Zähigkeit von Materialien durch Schadensinitiierung, die durch solche Heterogenitäten begünstigt wird, entscheidend reduziert werden. In dieser Arbeit wurde der Einfluss einzelner Mikrostrukturmerkmale und zugrundeliegender Versetzungswechselwirkungen auf mechanische und/oder Schadensreaktionen von Materialien durch systematische Simulationsstudien untersucht. Kristallplastizität Fast-Fourier-Transformation Simulationen wurden durchgeführt, um tiefe Einblicke in die komplexen Wechselwirkungen zwischen einzelnen mikrostrukturellen und mikromechanischen Mechanismen in heterogenen Strukturen zu gewinnen. In dieser Arbeit wurden zwei Materialsysteme und die damit verbundenen Eigenschaften untersucht: Die erste ist die partikelinduzierte Schädigung in Fe-TiB_2-Metallmatrix-Verbundstählen und die zweite ist die Bildung einer Laminatverformungsstrukturierung in einem Nickeleinkristall.

Fe- TiB_2-Metallmatrix-Verbundwerkstoffe, die aufgrund ihrer hohen spezifischen Steifigkeit als Stähle mit hohem Elastizitätsmodul bezeichnet werden, haben ein großes Potenzial für Leichtbauanwendungen. Die Zähigkeit dieser Stähle wird jedoch durch die Anwesenheit der spröden TiB_2-Partikel entscheidend verringert. Aufgrund der Vielzahl von Parametern, die die Schädigung von Mikrostrukturen beeinflussen, sind experimentelle Studien komplex und ineffizient, um den Einfluss der Mikrostruktur von Partikeln auf die Bruchzähigkeit zu identifizieren. In dieser Arbeit wurde ein

Berechnungssimulationsansatz zur Ableitung von Richtlinien zur Optimierung der mechanischen Eigenschaften von Stählen mit hohem Modul durchgeführt. Wichtige mikrostrukturelle Parameter wie Partikelclustergrad, Größe und Volumenanteil wurden untersucht. Modellgeometrien wurden statistisch und systematisch mit unterschiedlichen Partikelkonfigurationen von zufälligen zu gruppierten Verteilungen erzeugt. Simulationen wurden dann unter Verwendung eines Kristallplastizitäts-Fast-Fourier-Transformations-Simulationsverfahrens in Verbindung mit einem neuartigen Phasenfeldschadensmodell durchgeführt. Die Wirkung einzelner Partikelparameter auf die Partikelschädigung zeigte, dass Mikrostrukturen mit homogenen Partikelverteilungen von 7 bis 15 Vol .-% TiB_2 ohne große primäre TiB_2-Partikel (die primären Niederschläge für die hypoeutektische Zusammensetzung) am günstigsten sind, um Stähle mit hohem Elastizitätsmodul mit erhöhter Zähigkeit zu erhalten.

Deformationsmuster in Form von Deformationsbändern werden in Einkristallen unter geeigneten Belastungsbedingungen beobachtet. In dieser Arbeit wurden die Gründe für diese starke Deformationsstrukturierung durch Kristallplastizitätssimulationen untersucht. Ein fc-c-Nickel-Einkristall mit einer anfänglichen Nähe-Kupfer-Orientierung wurde in ebenen Spannungs-Kompressions-Randbedingungen deformiert. Es wurde festgestellt, dass die sich ergebende Dehnungsaufteilung in Form alternierender paralleler Bänder in einem sehr frühen Belastungsstadium initiiert wird und bei fortschreitender Verformung scharf wird. Es zeigte sich, dass die Mikrostrukturkaschierung das Ergebnis eines komplexen Zusammenspiels von verfügbaren Deformationssystemen, Kaltverfestigung, Kinematik und Deformationsenergien ist: (i) Die dislozierende kollineare Wechselwirkung spielt eine wesentliche Rolle bei der Bildung der Deformationsbanden unter den auferlegten Randbedingungen ; (ii) der Laminatmusterfall minimiert den Energiebeitrag aufgrund der starken kollinearen Wechselwirkungsstärke durch Auswählen eines lokal vorherrschenden Gleitsystems. Dieses Verhalten erklärt sich durch die geringere globale Verformungsenergie im Vergleich zu einem homogenen Doppelschlupfverhalten. Es zeigte auch, dass nur die Werte der Wechselwirkungsstärke

in dem Bereich, der durch dynamische Simulationen mit diskreter Versetzung vorhergesagt wird, zu Verformungsbändern führen.

Insgesamt wurden in dieser Arbeit die Effektivität und Möglichkeiten systematischer Kristallplastizitätssimulationen vorgestellt und diskutiert. Die komplexen Wechselwirkungen zwischen einzelnen mikrostrukturellen und mikromechanischen Mechanismen in Strukturheterogenitäten wurden identifiziert. Basierend auf der Wirkung einzelner mikrostruktureller Merkmale können die optimierte Mikrostruktur oder die schadenstoleranten Mikrostrukturen abgeleitet werden und mehr Erkenntnisse für die zugrunde liegenden Deformations- und Schädigungsmechanismen gewonnen werden.